1984

Microstructural characteristics during the controlled solidification of a binary system

Khanchai Somboonsuk
Iowa State University

Somboonsuk, Khanchai

MICROSTRUCTURAL CHARACTERISTICS DURING THE CONTROLLED SOLIDIFICATION OF A BINARY SYSTEM

Iowa State University PH.D. 1984

PLEASE NOTE:

In all cases this material has been filmed in the best possible way from the available copy. Problems encountered with this document have been identified here with a check mark ✓.

1. Glossy photographs or pages _____
2. Colored illustrations, paper or print _____
3. Photographs with dark background ✓
4. Illustrations are poor copy _____
5. Pages with black marks, not original copy _____
6. Print shows through as there is text on both sides of page _____
7. Indistinct, broken or small print on several pages _____
8. Print exceeds margin requirements _____
9. Tightly bound copy with print lost in spine _____
10. Computer printout pages with indistinct print _____
11. Page(s) _____ lacking when material received, and not available from school or author.
12. Page(s) _____ seem to be missing in numbering only as text follows.
13. Two pages numbered _____. Text follows.
14. Curling and wrinkled pages _____
15. Other _____

Microstructural characteristics during the controlled solidification of a binary system

by

Khanchai Somboonsuk

A Dissertation Submitted to the

Graduate Faculty in Partial Fulfillment of the

Requirements for the Degree of

DOCTOR OF PHILOSOPHY

Department: Materials Science and Engineering
Major: Metallurgy

Approved:

Signature was redacted for privacy.

In Charge of Major Work

Signature was redacted for privacy.

For the Major Department

Signature was redacted for privacy.

For the Graduate College

Iowa State University
Ames, Iowa

1984

TABLE OF CONTENTS

I. INTRODUCTION

During the directional solidification of alloys, the structure of the solid-liquid interface can be planar, cellular, or dendritic depending on the alloy or impurity composition, the growth velocity and the temperature gradient at the interface. If the temperature gradient and alloy composition are fixed, then at low velocities a planar interface is observed. As growth velocity is increased, the interface becomes unstable and complex interface patterns develop which ultimately stabilize to form cellular or dendritic structures. These dendritic and cellular structures are quite important from the practical viewpoint since these structures commonly occur during the solidification of alloys in casting or welding processes. One of the important consequences of such structures is the occurrence of microsegregation between the cells or dendrites. These microsegregation patterns, which greatly influence the mechanical properties of solidified alloys, can be controlled during the solidification process since the periodic concentration variation coincides with the periodicity of the dendrite arm spacings. Consequently, many experimental and theoretical studies have been carried out over the past thirty years to study the solid-liquid interface morphologies under controlled growth conditions. For metal systems, two major difficulties have been encountered during these experimental studies.

1) The interface structure produced during the solidification process cannot be observed <u>in situ</u>, so that the time evolution and the mechanism by which a planar interface breaks up and restabilizes into a

more complex cellular or dendritic pattern cannot be studied precisely.

2) The measurements of cell and dendrite characteristics can be carried out after complete solidification or after interrupting the steady-state growth by a rapid quench. However, not all of the steady-state characteristics, i.e. primary spacing, λ_1, secondary spacing, λ_2, and tip radius, ρ, can be measured accurately. The measurement of λ_1 is unambiguous since primary spacings do not coarsen with time and they can be accurately measured from the microstructure of a cross-section taken perpendicular to the growth direction. On the other hand, the measurements of ρ and of λ_2 are not always reliable since the interface profile may be altered during the quenching process. Consequently, it is desirable to select a system in which λ_1, λ_2 and ρ can all be measured unambiguously.

For this reason, directional solidification experiments have been carried out in this research work by using a transparent organic system. These materials, first used by Jackson and Hunt [1], should have the entropy of fusion in the same range as that of metals, i.e. $\Delta S/R < 2$, where R is the gas constant. Therefore, these compounds would solidify with a nonfaceted interface and would give interface patterns which are analogous to those for metals. In these transparent materials, the interface morphology, spacings and tip radii could be observed and measured directly during the solidification process. The succinonitrile-acetone system was selected in this study since it has a low entropy of fusion and its solidification characteristics are analogous to those of metal systems. Furthermore, the values of all

required physical properties are known quite accurately through the study by Glicksman [2].

One of the advantages of a transparent system is that the actual time dependent changes leading to a steady-state pattern can be studied quantitatively. The formation of this steady-state pattern is nonequilibrium phenomenon and the precise understanding of the time evolution of this pattern and the study of its stability require nonlinear analysis. Although a number of theoretical models [3-7] have now been proposed to understand pattern formation during the solidification of alloys, no experimental results are available to describe this complex pattern formation.

Thus, the objective of this study is to carry out critical experimental studies to understand microstructural characteristics of the solid-liquid interface during the directional solidification of the binary system of succinonitrile and acetone. The experimental results and discussion will be presented in four parts.

In the first part, the experimental work will be carried out under steady-state growth conditions to determine the characteristics of cellular and dendritic structures as a function of solidification conditions. Specifically, the steady-state characteristics, which include primary spacings, λ_1, secondary dendrite spacing, λ_2, tip radius, ρ, and the location of first sidebranch perturbation are measured as a function of growth rate V, temperature gradient G and alloy compositions C_∞. These results will be discussed and used to examine critically the theoretical models that are available currently. These detailed experimental

studies will enable us to determine precisely the optimization principle or the stability criterion which uniquely characterizes various stability steady-state lengths under given experimental conditions.

In the second part, a series of experiments will be carried out to study the transient effects of interface shape as the growth rates are suddenly altered. Initially, the solidification runs are performed at constant velocity until a steady-state interface shape is obtained. Next, the externally imposed velocity is suddenly changed to a higher value. The time dependent changes of the interface's pattern will be studied as the interface restabilizes into the new steady-state configuration. The following questions will be investigated: How fast does the interface velocity, dendrite tip radius, primary spacing and initial secondary arm spacings adjust to the new value? What is the mechanism of creation (or destruction) of primary dendrites during the adjustment of the primary spacing? How does the tip radius approach the stable value? Experimental studies will also be carried out to study the restabilization of the interface as the growth rate is suddenly reduced. Mechanisms which operate during the restabilization of the interface will also be examined for these two cases.

In the third part of these studies, experiments will be carried out to determine the initial breakup of the planar interface as a function of V, when $V > V_{cr}$, where V_{cr} is the marginal stability point for a planar interface. At $V > V_{cr}$, the planar interface is unstable with respect to a range of wavelengths. The objective is to determine if the system chooses any specific wavelength during the initial breakup

of a planar interface when $V > V_{cr}$. In addition, experiments will also be carried out to illustrate the transient interface patterns which emerge as the interface changes from a planar shape to a cellular or dendritic shape. Our aim is not only to characterize the pattern evolution, but also to understand the principle which governs the stabilization of the pattern which occurs after some time.

In the fourth part, experimental work will be extended to examine the dynamics of dendritic structures. The coarsening of secondary dendrite arm spacing as a function of solidification time will be studied. Also, the development of tertiary branches during the adjustment of primary arm spacing will be characterized.

II. LITERATURE REVIEW

A. Stability of a Planar Interface

The original study of interface breakup was carried out by Tiller et al. [8]. They used a simple argument that a planar interface, if it developed a small protuberance, would be unstable and the protrusion would grow faster than the planar elements of the interface if the liquid region ahead of the interface had a greater degree of supercooling than the liquid region at the interface. Thus, a planar interface moving at a constant velocity in an alloy system with a positive temperature gradient in the liquid would be unstable only when

$$V > G_L D/\Delta T_o \tag{1}$$

where G_L is the temperature gradient in liquid at the interface, D is the solute diffusion coefficient in liquid and ΔT_o is the equilibrium freezing range of the alloy. Tiller [9] subsequently pointed out that the stability of the interface should also depend upon the temperature gradient in the solid. He modified Equation (1) to the form

$$V > GD/\Delta T_o \tag{2}$$

where G is the average temperature gradient in liquid whose value was suggested as $G = (K_L G_L + K_S G_S)/(K_L + K_S)$ and K_L and K_S are thermal conductivities of liquid and solid, respectively.

Mullins and Sekerka [10] pointed out that the constitutional supercooling criterion was based only upon thermodynamic consideration of liquid ahead of a planar liquid-solid interface. Such consideration

would not necessarily predict the phase which was dynamically achievable. Mullins and Sekerka, therefore, carried out a first-order linear perturbation analysis which included the thermal fields, as well as the solid-liquid interfacial energy. They analyzed the stability problem by calculating the time dependence of the amplitude introduced into the planar shape. The analysis gave the ratio of the time derivative of amplitude ($\delta^{\cdot}$) to the amplitude (δ) of the initial perturbation as follows:

$$\frac{\delta^{\cdot}}{\delta} = f(w) = S(w)h(w) \tag{3}$$

$$S(w) = \left[-T_m \Gamma w^2 - \tfrac{1}{2}(g'+g) + mG_c \frac{(w^* - V/D)}{(w^* - \frac{V}{D}(1-k))}\right] \tag{4}$$

$$\text{and } h(w) = 2Vw/\left[(g'-g) + \frac{2wmG_c}{(w^* - \frac{V}{D}(1-k))}\right]$$

where $g' = 2G_L K_s/(K_s+K_L)$,

$g = 2G_s K_L/(K_s+K_L)$,

$w^* = \frac{V}{2D} + \left[(\frac{V}{2D})^2 + w^2\right]^{\frac{1}{2}}$,

T_m = melting point of solvent,

Γ = the ratio of interfacial energy (γ) to latent heat of fusion per unit volume,

w = frequency of the interfacial perturbation, and

G_c = gradient of the solute distribution at the solid-liquid interface in the liquid.

Equation (3) can be solved to give the result

$$\delta = \delta_o \exp f(w)t$$

where t is time and δ_o is the amplitude of the initial perturbation. Therefore, the stability of the planar interface which respects to an undulation depends on the sign of f(w), i.e. δ increases with time only if $f(w) > 0$. The value of h(w) is always positive so that the sign of f(w) depends only on the sign of S(w) in Equation (4). The first term on the right-hand side of Equation (4) arises from the capillarity effect and since it is always negative, it favors decay of any perturbation. The second term which arises from thermal gradients is negative and thus, it also favors decay. The third term representing the effect of solute on the equilibrium melting temperature is always positive and therefore, favors growth of perturbation and instability. Instability occurs if there is any frequency for which the magnitude of the third term exceeds that of the sum of the first two terms; otherwise, stability prevails.

The frequency dependence of Equation (4) comes about in two ways. At low frequency (or large wavelength of perturbation), the interface is stabilized by the lack of long-range lateral diffusion, whereas the interface with high frequency (small wavelength of perturbation) is stabilized because of the effect of surface tension. Consequently, δ^*/δ should go through a maximum with w. Mullins and Sekerka predicted that the final wavelength of the perturbed profile should correspond to the wavelength which grew at the fastest rate, i.e. the final spacing

should correspond to λ_{max} or w_{max}, where $\lambda_{max} = 2\pi/w_{max}$. The value of w_{max} is determined from the plot of Equation (3) and w_{max} is the frequency of interfacial wave at maximum in the δ^*/δ curve.

Figure II.1 shows the sketch of f(w) as a function of wave frequency for several growth rate conditions. In case 3, all perturbations will decay with time so that this case corresponds to a stable planar interface. In curve 1, there is a range between w_o and w_{oo} where f(w) is positive. The amplitude of perturbation will increase exponentially with time and this will constitute instability of a planar interface. The frequencies of the perturbed interface will lie between w_o and w_{oo} value. The curve 2 represents the condition of marginal stability of a planar interface, and it characterizes the critical velocity where the planar interface just becomes unstable. The planar interface is unstable if the growth velocity is higher than the growth velocity at marginal stability point, i.e. $V > V_{cr}$.

Many experimental studies have been carried out to test the validity of the stability theory.

Hardy and Coriell [11-14] and Coriell and Hardy [15] have conducted the experiments of ice crystal growth in pure undercooled water. In their experiments, the relative growth rate of perturbation in two different directions was measured. If the solid-liquid surface tension was taken as known, calculated values of the relative growth rate from perturbation analysis agreed very well with experiment to within 10%. In a later paper [16], they measured the relative growth rate of ice and combined with the perturbation theory to calculate the value of

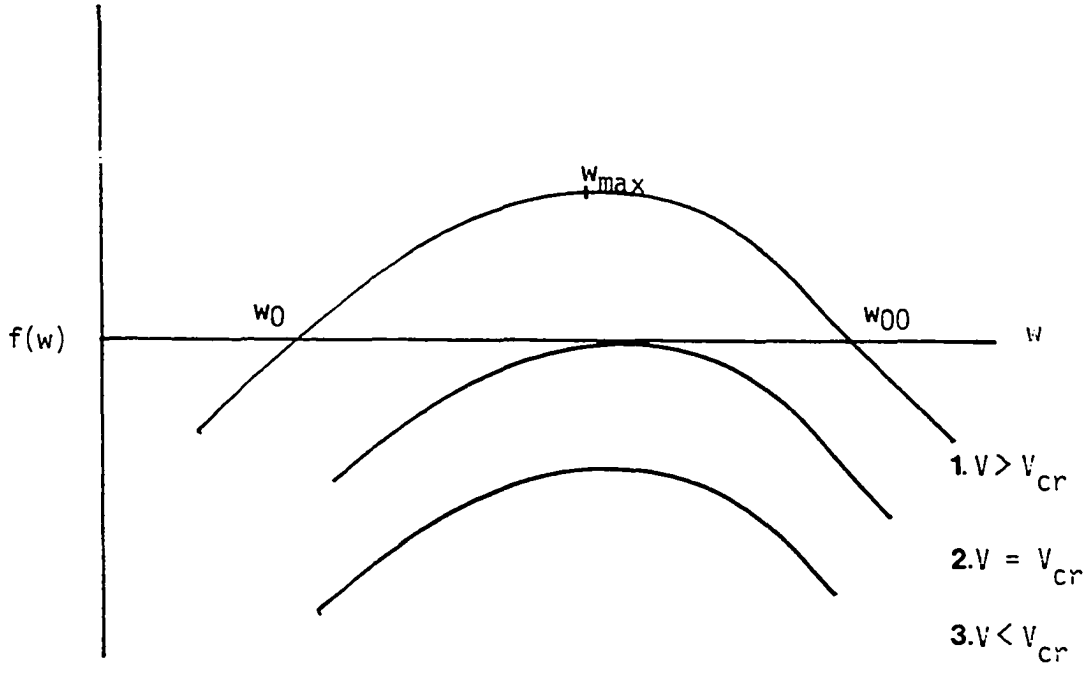

Figure II.1. f(w) vs. w for various growth conditions. Case 1, instability ($V > V_{Cr}$); Case 2, marginal stability ($V = V_{Cr}$); Case 3, stability ($V < V_{Cr}$)

ice-water surface tension. The results were in satisfactory agreement with the value obtained from an independent experiment.

Although experimental studies on the stability of ice growth in undercooled water are in strong support of the perturbation theory, the studies on the stability of a planar interface of alloy crystals grown under the positive temperature gradient have not been sufficient to check the validity of the perturbation analysis. In metallic alloys, the study of the developing perturbation as the planar interface breaks up cannot be observed. Consequently, the wave frequency and the amplitude of perturbation are examined from the observation of the solid-liquid interface after quenching the unidirectionally solidified alloy. Most experimental studies on the stability of a planar interface have been carried out at growth velocity near the critical velocity, $V \simeq V_{cr}$. The initial wave frequencies are measured and the surface energy of the liquid-solid interface is determined.

Sato and Ohira [17] observed the interfacial frequency of planar solid-liquid interface during the directional solidification of Al-Cu alloy at a critical state of stability. Their results showed that the initial perturbations were distributed at random and had a wide range of interfacial wave frequencies. They concluded that the observed perturbation in the quenched specimen was not the perturbation at the critical state, but above the critical state into the unstable region. This deviation from critical state occurred because the experimental conditions were not constant during the solidification process. Thus, it caused a wide range of interfacial wave profiles to grow.

In the next paper, Sato et al. [18] utilized the perturbation theory (Equation 3) to calculate the maximum wave frequency at a little deviated condition from the critical state. The result showed that the range of possible wave frequencies in the unstable condition was wider in the alloys of smaller k than in the alloys of larger k. They also showed that the maximum wave frequency was insensitive to the growth velocity in Al-Ti and Al-Cr alloys and thus, w_{max} at the critical state was approximately equal to w_{max} at unstable condition ($V > V_{cr}$).

Subsequently, Shibata et al. [19] used the results of the perturbation theory to determine the interfacial energies of Al-Ti and Al-Cr alloys. The value of the interfacial energy for the Al-Cr alloy determined by this method was found to be close to that for pure aluminum, although the value for Al-Ti alloy was found to be only one-half of that for pure aluminum.

As can be seen from the above discussion, the interfacial energies (γ) calculated from the interfacial wave frequencies of the quenched alloy after directional solidification are inconsistent. Thus, precise experimental studies of the interface perturbation process in metallic alloy are not possible. By using a transparent material, the development of initial perturbation on the planar interface can be observed in situ, so that the experimental studies can be carried out to study the velocity dependence of the perturbed wave spectrum.

B. Cellular and Dendritic Interface

When the growth rate of the interface is increased above the critical velocity for the planar interface breakdown, a zone of supercooled liquid exists ahead of the planar interface which causes the interface to become unstable and form a cellular shape. Teghtsoonian and Chalmers [20] and Atwater and Chalmers [21], in the original works on cellular structure, found that cells did not form along any specific crystallographic direction, and that their orientation was controlled mainly by the heat flow direction. However, they also observed cells whose growth direction deviated from the heat flow direction. They found that cells in cubic crystals tended to grow along <100> direction and this tendency increased as the deviation from planar interface stability condition was increased, i.e. G/V was reduced. As the ratio, G/V, was decreased further, the cellular structure changed to a dendritic structure and secondary arms began to appear. Tiller and Rutter [22] found that the breakdown from cells to dendrites depended upon the crystallographic orientation of the interface. For given temperature gradient and composition, the cellular-to-dendritic transition occurred at higher velocities for cells with <100> growth direction, compared to cells whose growth direction deviated from <100> direction.

Experimental studies of dendritic structures in pure undercooled melt [23-25] and in directionally solidified binary alloy [26] showed that dendritic structure developed certain steady-state characteristics at the advancing front, whereas at the interface regions further behind

the advancing front, a nonsteady-state evolution of sidebranches occurred. The major morphological features of a dendritic interface are the primary dendrite, λ_1, secondary dendrite spacing, and the dendrite tip radius ρ. Because the secondary dendrite spacing tends to coarsen with time or with distance away from the dendrite tip, one should relate only the initial spacing, λ_2, which forms close to the dendrite tip, with the steady-state conditions of growth. Some experimental and theoretical works on each steady-state characteristic are reviewed as follows.

1. Dendrite tip characteristics

A number of theoretical and experimental studies have been carried out to explain the dendrite tip characteristics as a function of growth conditions. Most of them characterized the dendrite tip by measuring the temperature and composition at the dendrite tip as a function of growth velocity and temperature gradient in liquid.

Kramer et al. [27] measured the temperature of a cellular interface in Sn-Pb alloy. They found that the interface temperature increased and approached liquidus temperature as the growth velocity was increased. Also, Sharp and Hellawell [28] carried out microprobe analysis to measure the solute concentrations at the tips of cell and dendrite in Al-Cu alloy. They found that the solute undercooling decreased (or tip temperature increased) with the increase in the growth rate. In contrast to these results, Backerud and Chalmers [29] and Doherty et al. [30] found that the dendrite tip temperature

decreased with an increase in the growth rate. This apparent inconsistency was resolved by Burden and Hunt [31] who measured the tip temperature over a wide range of growth rates and found the tip temperature to go through a maximum as the velocity was increased.

The first approximate theoretical model, valid at low growth rates only, was proposed by Bower et al. [32] which predicted that the tip temperature would increase with the growth rate. A more detailed study was carried out by Burden and Hunt [33]. They ignored the interactions of neighboring dendrites and assumed a constant temperature gradient in the entire liquid region. Their results for a given temperature gradient, G_L, and growth velocity, V, can be written in terms of dimensionless parameters as

$$\frac{\Delta T}{\Delta T_o} = \left[\frac{\phi k}{1 - \phi(1-k)}\right] \left[1 + \tfrac{1}{2}\psi Ng(p) + \frac{2\mathcal{A}}{p^2} f(p)\right] \tag{5}$$

where $T = T_m + mC_\infty - T_t$ is the tip undercooling in which T_m is the melting point of pure solvent, m the slope of the liquidus, C_∞ the initial composition and T_t the tip temperature. ϕ is the Ivantsov [34] function equal to exp P $E_1(p)$, p is a peclet number equal to $V\rho/2D$, $E_1(p)$ is the exponential integral function and dimensionless parameter ψ and $\mathcal{A}$ are given by [35]

$$\psi = \frac{2\bar{G}D}{Vk\Delta T_o} \tag{6}$$

$$\mathcal{A} = \frac{\gamma V}{2\Delta S D k \Delta T_o} \tag{7}$$

Here, $\bar{G}$ is the weighted average temperature gradient in the liquid which was assumed to be equal to G_L, the temperature gradient in liquid at the interface, by Burden and Hunt [33], k is the equilibrium partition coefficient, D is the solute diffusion coefficient in liquid, $\Delta T_o = mC_\infty(k-1)/k$ is the equilibrium freezing range of the alloy, γ is the solid-liquid interface energy, and S is the entropy of fusion per unit volume. The function Ng(p) and f(p) are complex functions which were approximately derived by Burden and Hunt [33]. Subsequently, a detailed theoretical model which considered the variation in concentration as well as temperature profile was given by Trivedi [35] who obtained a result similar to that given by Burden and Hunt with the values of functions Ng(p) and f(p) as

$$Ng(p) = (1-\Phi)/(\Phi-P+P\Phi) - (1/\Phi) \tag{8}$$

$$f(p) = \tfrac{1}{2}N_2(p) - P/\Phi \tag{9}$$

where $N_2(p)$ is a gradient function which was numerically evaluated by Trivedi [36]. The function f(p) represents the effect of capillarity on tip temperature.

The basic theoretical result, given by Equation (5), is still not complete since it does not give a unique solution, but predicts ΔT as a function of tip radius for given experimental conditions. This result is shown schematically in Figure II.2 which illustrates that tip temperature can vary between the solidus and liquidus temperature and the tip radius value will depend on the tip temperature assumed by the

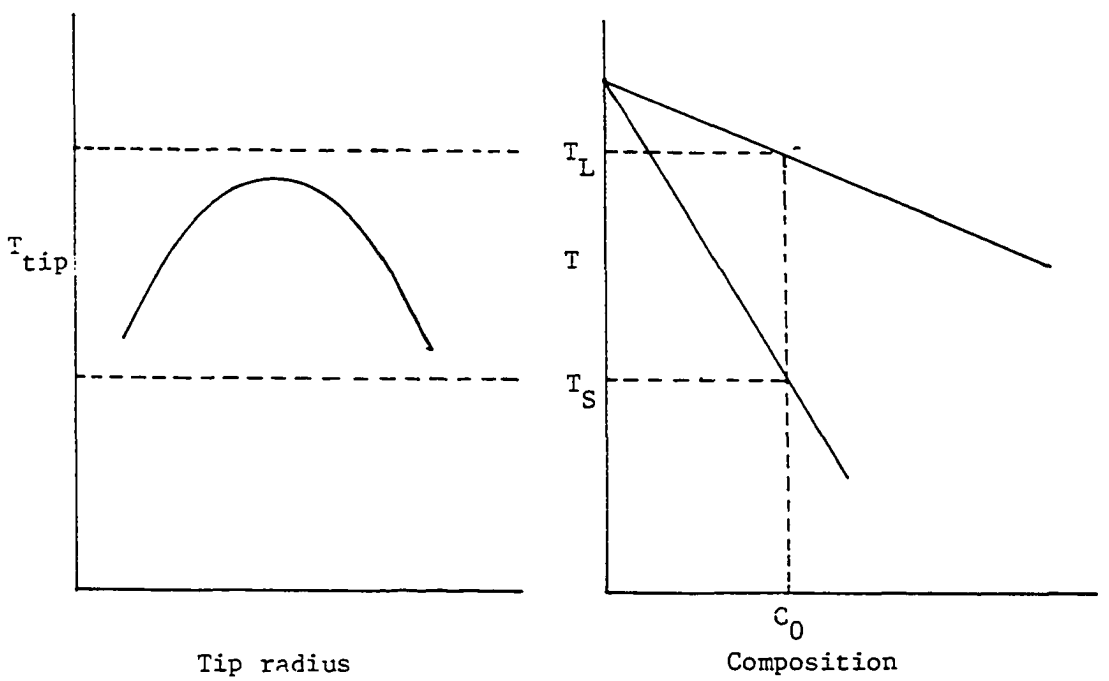

Figure II.2. A schematic illustration of the multitudes of theoretical tip radius which are possible for given growth conditions

dendrite. Since the unique tip characteristics are observed experimentally for given values of ω and $\mathcal{A}$, it is necessary to find a specific tip temperature which the interface chooses under given experimental conditions. Burden and Hunt [33] used the minimum undercooling principle to obtain a unique solution, whereas Jin and Purdy [37] used the principle of the minimum rate of entropy production. Based on the results of undercooled dendrite growth, Trivedi [35] and Kurz and Fisher [38] developed a marginal stability criterion to uniquely determine the dendrite tip radius. This stability criterion is given by the following relationship [35, 39]:

$$(C_t/C_\infty)\xi_c = (1/2)\omega' + \mathcal{A}_L/P^2 \qquad (10)$$

where $L = 1/2\ (\ell+1)(\ell+2)$ for the spherical approximation of dendrite front. For pure succinonitrile in an undercooled melt, Huang and Glicksman [24] found $\ell = 6$ to be operative for cubic crystals. For this condition, $L = 28$. The function ξ_c depends on peclet number [39] and it approaches unity for small peclet numbers. C_t is the tip composition. Equations (5) and (10) are simultaneously solved to obtain the variation of Peclet number and tip radius as a function of V, C_∞ and G as follows:

$$\frac{1}{2}\omega' + \frac{\mathcal{A}_L}{P^2} - 1 = \left[\frac{\phi(1-k)}{1-\phi(1-k)}\right]\left[1 + \frac{1}{2}\omega' Ng(p) + \frac{2\mathcal{A}}{P^2} f(p)\right] \qquad (11)$$

The results of theoretical calculation values of ρ as a function of V are given in Figure II.3. Two distinct growth rate regions are observed.

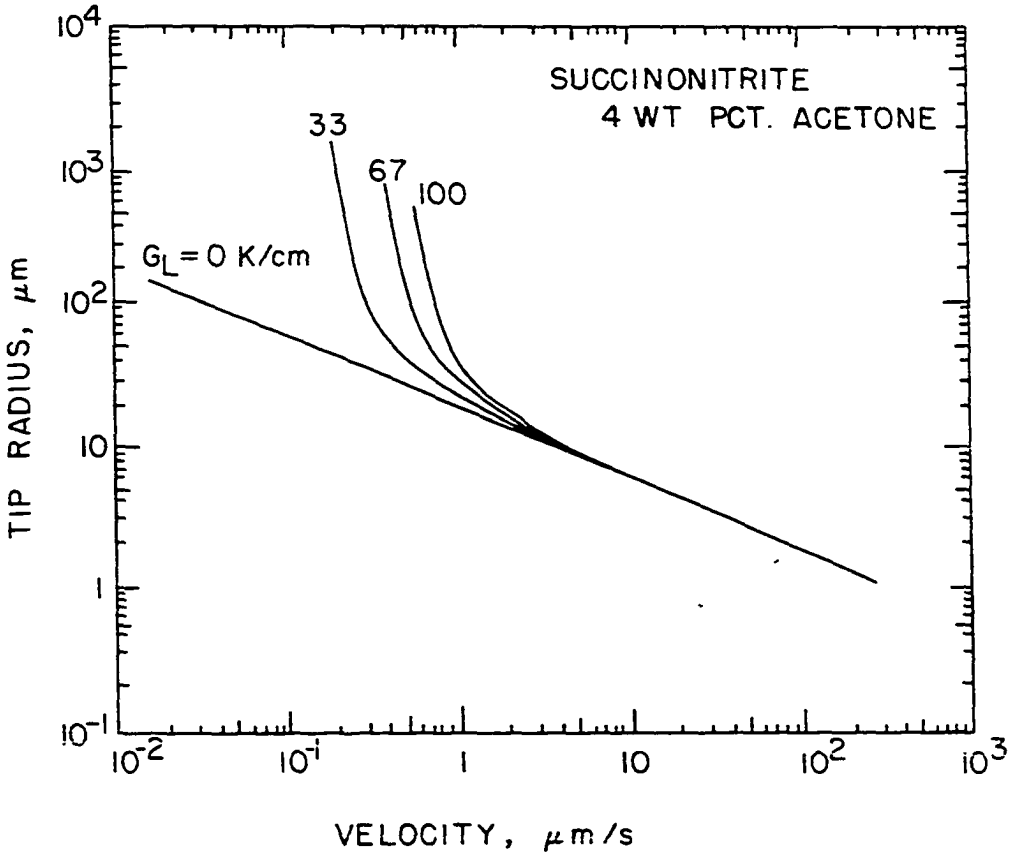

Figure II.3. Theoretical variation of tip radius as a function of velocity for different thermal gradient conditions

For low growth rate values, the tip radius is strongly influenced by the temperature gradient value. However, at higher growth rates, the tip radius becomes independent of temperature gradient. Near the transition velocity, the tip radius increases sharply with the decrease in growth rate. This rapid increase in the tip radius was associated by Kurz and Fisher [38] with the dendrite-to-cell transition. They also predicted that the transition would occur at $V = GD/k\Delta T_o$.

2. Initial secondary spacing

As discussed earlier, the steady-state secondary arm spacing is represented by the initial spacing, λ_2, at the dendrite tip. However, most experimental studies on secondary arm spacing [40-44] characterized the secondary spacing by measuring the average spacing of λ_2 with some distance behind the dendrite tip. These spacings change with time. Thus, the secondary spacings obtained from these experimental studies do not represent the steady-state characteristics of dendrite morphology. The only experimental work on initial spacing λ_2 was carried out by Okamoto and Kishitake [45] in the directional solidification of cyclohexanol-water system. The initial spacing in this system was clearly observed, and they found that λ_2 was proportional to V^{-a} and G^{-b}. The exponents a and b were equal to 0.49 and 0.4, respectively. No correlation was made with the dendrite tip radius.

Although the experimental study of λ_2 for dendrites grown under positive temperature gradient is limited, extensive studies have been carried out on the initial secondary spacing for dendrites grown in

undercooled liquids. The recent theoretical work by Langer and Müller-Krumbhaar [46] related the initial secondary spacing to the tip radius of the isothermal dendrite growth. Their model predicted $\lambda_2/\rho = 2.1 \pm 0.03$. A detailed experimental study of the initial secondary spacing was carried out by Huang and Glicksman [25] in pure undercooled succinonitrile and they found that a definite scaling law existed between λ_2 and ρ with the relationship $\lambda_2/\rho = 3.0$. Similarly, Honjo and Sawada [47] reported $\lambda_2/\rho = 4.68$ for the growth of ice dendrites in an undercooled water and NH_4Br solution. Besides this scaling law, Huang and Glicksman [25] also found that the position of the first distinguishable sidebranch appeared to vary with the supercooling. They found that the first sidebranch perturbation occurred somewhat further behind the dendrite tip at smaller supercooling (or the distance from the tip for the first sidebranch, λ_p, increased as the growth velocity was decreased). This relationship between λ_p and growth conditions seems to occur in dendritic structure and the λ_p may be one of the steady-state characteristics of dendrite morphology.

The results that are discussed above show that the observation of dendritic structure in transparent materials gives us some valuable results which cannot be obtained in metallic systems. Thus, it is desirable to use a transparent system to characterize these steady-state characteristics (λ_2 and λ_p) as a function of growth rate, temperature gradient and alloy composition in an alloy which is directionally solidified.

3. Primary arm spacing

During the past thirty years, several directional solidification studies [48-56] have been carried out to characterize primary dendrite spacing as a function of growth conditions.

One of the first experimental works on primary dendrite spacing was carried out by Bell and Winegard [48]. They measured primary dendrite spacing in tin lead alloy solidified vertically under steady-state condition as a function of V and G. The functional dependence of these variables was given by equations of the form

$$\lambda_1 = (A-B\ell nG)(R)^n \qquad n < 1$$

where A, B and n increased with composition. The results showed that the dendrite spacing decreased as V and G increased, and increased as the lead constant increased.

Coulthard and Elliot [49] measured the cell spacings in Pb-Sn and Pb-In alloys directionally solidified at the steady-state condition and found that λ_1 was proportional to $V^{-0.5}$ and $G^{-0.25}$. The result of λ_1 versus V was larger than the result on the Cd-Zn alloy system of Jesse and Giller [50], who found that the slopes of log λ_1 versus log V were about 0.41 and 0.44 for Cd in Zn and Zn in Cd, respectively.

Subsequently, Sharp and Hellawell [26, 28, 51] measured the primary spacing and cell tip radius in Al-Cu alloys. They found that the cells did not change their spacing, λ_1, with growth rate V and alloy concentration, C, but decreased with the imposed temperature gradient, G,

possibly as G^{-2}. At the same time, the radius of curvature of the tip of a cell, ρ, decreased with V, C and G roughly according to G^{-1} and $(VC)^{-\frac{1}{2}}$. They concluded that cells were stable until conditions (G, V, C) were such that $\rho \leq 1/2\ \lambda$, i.e. until the cell tips were approximately hemispherical in longitudinal section. Thereafter, as ρ decreased further, there was a sudden transition to a branched shape and this was a transition which was as sharp as that from planar to nonplanar front. After this transition, λ_1 was no longer insensitive to growth rate and concentration, but increased sharply with V as soon as branches appeared. Subsequently, λ_1 decreased with V - possibly with $V^{-\frac{1}{2}}$.

Following the experiments that have been discussed above, further experiments to correlate primary dendrite spacing with G, V and C have been carried out [52-56]. Most of the recent directional solidification studies that isolated the effect of G, V and C have shown that the primary spacing can be correlated with G, V and C as

$$\lambda_1 = K\ V^{-a}\ G^{-b} \tag{12}$$

where a and b are constants and the value of K includes the composition dependence. Three detailed theoretical models have been proposed in the literature [38, 57, 58] to characterize primary spacing as a function of growth rate, temperature gradient and alloy composition. The first significant treatment was presented by Hunt [57]. His model was based on the assumptions that: 1) a dendrite or cell tip may be approximated by a smooth steady-state shape even when secondary arms have been formed, and 2) temperature and composition in liquid are

constant along the direction perpendicular to the dendritic growth direction. Under these assumptions, Hunt derived the shape of cell by using material balance within a volume element. The results gave the shape of a cell accurately far from the tip. However, the interface shape was not valid near the tip region since the assumption (2) was not valid in this region. Hunt resolved this problem by fitting part of a sphere to derive the shape at the dendrite tip. From these results, he obtained a relationship between λ_1 and ρ as follows:

$$G\lambda_1^2/\rho = -4\sqrt{2}\left[mC_t(1-k) + \frac{GD}{V}\right] \quad . \tag{13}$$

Hunt then substituted the tip radius value from this equation into a simplified Burden and Hunt [33] equation for dendrite tip undercooling and obtained a result which related primary dendrite spacing and tip undercooling. By assuming that dendrites grow at the minimum undercooling for a given velocity, the relationship between V and λ_1 was obtained as follows:

$$VG^2\lambda_1^4 = -(64\gamma D/\Delta S)\left[m(1-k)\ C_\infty + kGD/V\right] \quad . \tag{14}$$

Equation (14) showed that for $V >> kGD$, λ_1 is proportional to $V^{-1/4}$ and $G^{-1/2}$, which agree very well with the relationship in Equation (12). He suggested that this equation should apply for both primary dendrite and cell spacings. However, recent experimental work on lead dendrite growth in Pb-Sn system by Klaren et al. [54] and Mason et al. [55] found that the relationship in Equation (12) was indeed not valid in general.

The primary dendrite spacing did not continually increase with decreasing velocity or temperature gradient, but it went through maximum. Only at high velocity did they find the relation $\lambda_1 = KG^{-a}V^{-b}$ to hold true.

Recent theoretical work by Kurz and Fisher [38] also supported Klaren and Mason works. They derived the equation for cell and primary dendrite spacings by using stability criterion proposed by Langer and Müller-Krumbhaar [46] in place of the criterion of maximum velocity and minimum undercooling. Their results give equation of λ_1 at two velocity regions:

at low V,

$$\lambda_1 = \frac{6\Delta T'}{G(1-k)} \left(\frac{D}{V} - \frac{\Delta T_o k}{G}\right)^{\frac{1}{2}} \quad , \text{and} \tag{15}$$

at high V,

$$\lambda_1 = 4.3\ \Delta T^{\frac{1}{2}} [\gamma D/\Delta S k \Delta T_o] V^{-\frac{1}{4}} G^{-\frac{1}{2}} \quad . \tag{16}$$

Equation (16) is very similar to Equation (14) obtained by Hunt. Thus, in the high velocity regime, the results predicted by these two theories differ only by a constant. However, in the low velocity regime, these two theories give significantly different results. In Kurz and Fisher model, λ_1 increases sharply with decrease in velocity at $V = V_{cr}/k$. The effect of this at low velocity is for the interface morphology to change from cell to dendrite structure.

Another theoretical model was presented by Trivedi [58], who modified Hunt's treatment to predict the primary spacing as a function of G, V and C_∞. Instead of using the minimum undercooling criterion, Trivedi used a marginal stability criterion from Equation (10) and

substituted it into Equation (13) and found the following relationship:

$$\frac{\lambda_1^2 G}{\rho k_o \Delta T_o} = 4\sqrt{2}\,A_{L/P}^2 \quad . \tag{17}$$

The value of radius of curvature was calculated from Equation (11) and used to completely define the primary dendrite spacing. A comparison between these three theoretical models and experimental data of primary dendrite spacing will thus enable us to understand the relationship between the primary spacing and the growth conditions.

C. Secondary Arm Coarsening

In the ingot solidification, it has been observed that the final secondary dendrite arm spacing in a fully-solidified casting is usually coarser than the one that forms initially. This coarsening process influences dendritic structures in other ways than simply by altering the final secondary arm spacing. One effect is to decrease the amount of microsegregation which greatly improves the mechanical properties of metals. Consequently, many experimental studies on both metallic and nonmetallic alloys have been carried out to explain the mechanism of secondary arm coarsening.

From experimental studies on casting, Flemings et al. [59] and Bower et al. [32] have related the secondary spacing with the local solidification time $t_f = \Delta T_s/GV$, in which ΔT_s is the nonequilibrium temperature range of solidification. They proposed an empirical relationship $\lambda_2(t)\ \alpha t_f^n$, where the exponent n is in the range of 0.3 to

0.5. Following these works, many directional solidification studies [26, 43, 44, 53, 60] have been carried out to characterize the secondary arm spacing as a function of solidification time. Although all of the results of these experiments support the above relationship between λ_2 and t_f, the discrepancy between the effect of growth conditions and the rate of coarsening is still observed.

Sharp and Hellawell [26], in the directional solidification study of Al-Cu alloy, found that the rate of coarsening (or the exponent n) increased as the growth rate was increased. On the other hand, Young and Kirkwood [53] found that the rate of coarsening decreased with growth rate. They also found that the effect of increasing solute contents was to reduce the rate of coarsening. This result does not agree with the results obtained from the experimental studies of Taha et al. [60] and Jacobi and Schwerdtfeger [44] on the directional solidification of carbon steel. They found that the increase in carbon content increased the rate of coarsening.

Despite the experimental results discussed above, the theory of secondary arm coarsening in the directional solidification alloy has not been fully developed. However, theoretical studies have been done on the closely similar, but much simpler, problem of isothermal coarsening and at least three models are available in the literature [61-63]. The first two models [61, 62] described dendrite branch coarsening by the remelting of some of the secondary branches and the third [63] by the detachment of some branches. The recent theoretical model was proposed by Kurz and Fisher [64], who carried out the theory

of secondary arm coarsening for isothermal dendrite growth and found the relationship between λ_2 and t_f as

$$\lambda_2 = 4.4\ (Mt_f)^{1/3} \tag{18}$$

where $M = -2\Gamma D\ \ell n\ (C_E/C_\infty)/m(1-k)(C_E-C_\infty)$, where C_E is eutectic composition, C_∞ is the initial alloy composition.

A detailed experimental work by Huang and Glicksman [25] in pure succinonitrile showed that the mechanism of isothermal coarsening consisted of 1) the competitive growth mechanism, 2) the coarsening of inactive sidebranches by the surface energy reduction which leads to either formation of branch plates or remelting of small branches. Their experimental work showed very clear pictures which gave us some understanding of isothermal coarsening mechanisms, but the exponent n of the equation $\lambda_2 \alpha t_f^n$ was equal to 1.3, which was much higher than the one from other experiments. The discrepancy of these results is due to the different criterion used in the measurements of secondary arms spacing. Huang and Glicksman measured only the active sidebranches (the sidebranches which are larger than the neighboring sidebranches), whereas the other experiments on metallic alloy measured all the secondary branches behind the dendrite tip. Consequently, the slope of the proportionality is higher in the results of Huang and Glicksman, compared to that in the other investigations.

III. EXPERIMENTAL TECHNIQUE

A. Material Preparation

The as-received succinonitrile was impure and had a melting range of 3 K. This was purified by zone refining as described by Glicksman et al. [23]. Initially, succinonitrile was melted and partially recrystallized with the impure liquid decanted off. The crystals were then remelted into a 6 mm ID, 50 cm long pyrex tube under vacuum and sealed under an inert atmosphere. This material was further refined by making approximately 70 passes through a multistage vertical zone melter. The purified position of the material was stored in an inert atmosphere and used as needed. The melting point of the purified succinonitrile was 331.05 $\pm$ 0.03 K.

The acetone as-received was 99.9 mol % pure. This was further purified, as suggested by Werner [65], by first adding $AgNO_3$ and NaOH solution and then shaking the mixture for ten minutes. A layer of reduced silver was formed on the walls of the sample vessel. The water was removed by treating with anhydrous $CaSO_4$. The acetone was then distilled with the first and the last fractions being discarded.

The physical properties of the materials used in this study are given in Appendix A.

B. Controlled Solidification Equipment

A succinonitrile-acetone mixture of known composition was directionally solidified in a transparent glass cell. These cells were

made from two pieces of 19 mm square by 0.5 mm thick type 1059 pyrex glass slides which were first separated by a predetermined gap size, and then fused together on three sides with a micro-torch. In the case of low velocity run, i.e. $V < 2$ μm/s, and in the studies of transient effects, long sample cells of 25 x 38 mm were used to ensure that the steady-state condition was achieved. The cells were filled by capillary action on dipping a part of the open end into a molten solution of the desired composition.

The directional solidification apparatus, shown in Figure III.1, is similar to that described by Hunt et al. [66]. A temperature gradient is established by using a hot chamber and a cold chamber. The hot chamber consists of two transite plates grooved to accommodate a resistance heating wire. Copper plates, insulated by mica sheets, are placed next to the heating coils and formed the top and bottom walls of the heating chamber, thus providing uniform heat distribution. The top and bottom heaters are separated by 4 mm high side insulator bars. The cold chamber is made from the two stacked cold plates of 15 mm thick hollow brass with input and discharge tubes for cooling water. The heating and cooling chambers are 45 and 100 mm long, respectively. Both are 50 mm wide.

The heater and cooler are supported on tracks cut into the sides of the two support walls of 150 x 77 x 13 mm teflon. This allows both the heater and cooler to be moved so that the space between them is adjustable. The sample cell is placed in a bakelite holder which is connected through a screw and nut assembly to a variable speed DC motor

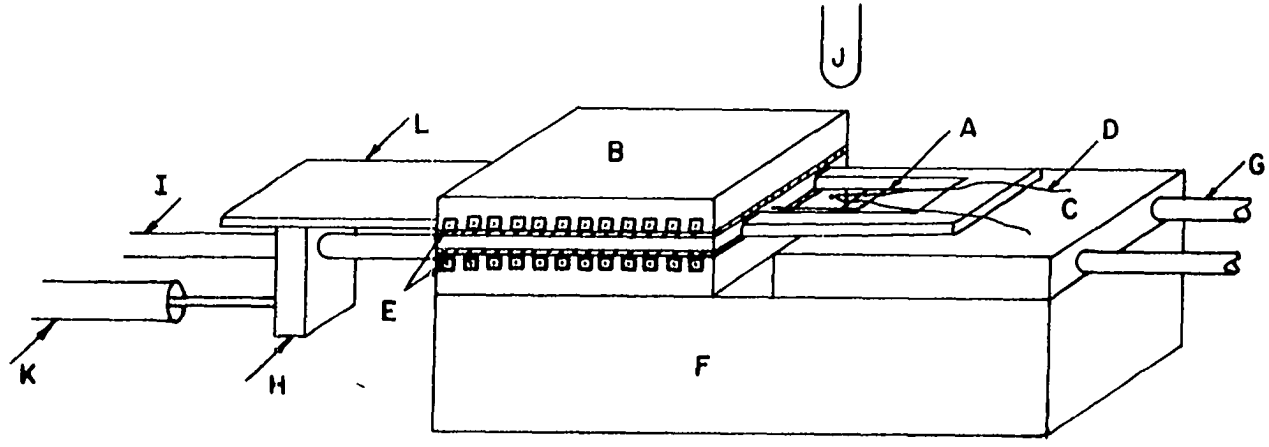

A) Sample cell
B) Hot chamber
C) Bottom cold plate. The top half of the cold chamber is not shown for clarity.
D) Thermocouple
E) Resistance heating wire
F) Teflon support track. The track sides extend to the top of the hot chamber and cold plate, but are not shown for clarity.
G) Water inlet and outlet
H) Driving nut
I) Drive screw connected to the motor
J) Microscope
K) Linear variable differential transformer
L) Bakelite cell holder

Figure III.1. A schematic diagram of the directional solidification apparatus

that provides constant linear rates between 0.066 and 300 μm/s.

A metallurgical microscope placed above the cell is used to observe the solid-liquid interface. Magnifications in the range of 25 to 100X were found to be adequate for this work. The microscope is equipped with a closed circuit television camera and monitor to observe the interface characteristics. Furthermore, quantitative measurements were made from pictures taken with either a still or movie camera. The camera is equipped with automatic exposure and timer to measure the light and time accurately during the photography process.

C. Velocity and Temperature Measurements

Approximate velocities of the drive train assembly were initially determined for different dial settings of the DC motor controller and for various increments of the speed reducer. Subsequently, the velocity of each run was determined by measuring the actual displacement of the cell with a linear variable differential transformer as a function of time. Velocities determined from recorder traces of the transducer output over distances of several mm and times of several hours were reproducible to 0.5 percent or better.

Temperatures were measured with 0.025 mm diameter chromel-alumel thermocouples. For precise measurement of the tip temperature, the thermocouple of each solidification run was calibrated with a precision mercury thermometer which was precisely calibrated by the National Bureau of Standards. The accuracy of temperature measured from calibrated thermocouple is within $\pm$ 0.05°C. The junction of

thermocouple was placed in the middle of the cell by positioning it on one glass slide prior to fusing the second slide during the construction of the cell. The cell and thermocouple were then dipped into the molten solution, and the cell filled by capillary action. Preliminary studies on the effect of the thermocouple placement in the cell showed that there was no difference in the measured temperature when the leads were brought out through either the solid or the liquid portion of the sample.

D. Experimental Procedure

Two solidification passes were made for each run. The first pass was made with a cell containing a thermocouple and a sample. The entire cell was first held in the hot chamber for a minimum of 2 hours to ensure thermal and solutal equilibria. The cell was then driven at high velocity about 200 μm/s across the gap and onto the cold plate until approximately 3 mm of sample was solidified. The system was then allowed to remain stationary for the time necessary to develop a planar interface with no sign of dendrite growth from the initial freezing. The drive was then turned on at the desired rate. The temperature at the thermocouple junction was recorded until the moving interface passed the thermocouple junction. The interface was observed through the microscope to ensure that steady-state conditions were established before the thermocouple approached the interface. As the interface position approached the thermocouple junction, a series of pictures was taken and the thermocouple outputs at the time that the

pictures were taken were marked on the recorder. The tip temperatures were then determined by correlating the thermocouple output on a chart recorder with the relative position of thermocouple and the interface obtained from the micrograph. The temperature gradient was also determined from the recorder trace at the point where the interface met the thermocouple. All gradients reported here were measured in the liquid at the dendrite or cell tips. In the case of transient effect studies, each solidification run contained two different velocities. Thus, it is necessary to determine the effect of growth velocity on temperature gradient at the same heater setting. With the fixed heater setting, temperature gradients were determined for steady-state growth at four different growth velocities. The results are shown in Table III.1. The temperature gradient was found not to vary significantly with growth rate. Consequently, the variation in temperature gradient at the interface can be assumed to be negligible during the change in velocities studied.

Table III.1. Variation of G with V

V, μm/s	G, K/cm
1.17	67.0
1.50	68.0
5.80	70.0
10.70	67.5

A second pass was made with an identical cell and sample, but without the thermocouple. Also, exactly the same experimental conditions were maintained as during the first pass. The pictures of the development of a planar interface when the interface just became unstable were taken with an automatic controlled 35 mm camera at a very short interval time. This ensured that the initial wavelength during the initial instability could be measured. When steady-state growth conditions were attained, the growing interface was photographed, as shown in Figure III.2. Both λ_1 and λ_2 were then measured from these photographs. The secondary spacing was found to coarsen with time so that its value increased with the distance from the tip. Consequently, only secondary spacings next to the dendrite tip were measured and these are reported here as λ_2. Furthermore, all measurements on dendritic structures were made only for glass cell sizes that were sufficiently large to permit well-developed sidebranches in all four directions.

The tip radius was measured by comparing the unperturbed tip region to a series of parabolas of known curvatures. The procedure consisted of projecting a greatly enlarged tip image from the photographic negative onto the standard parabolas, and adjusting the magnification until a best fit was obtained. A negative scale was then inserted into the enlarger in place of the photographic negative to obtain the magnification. The λ_2, λ_p and ρ values were measured on the same dendrite, as shown in Figure III.3. In this figure, a dotted parabola is superimposed to show that the unperturbed region of the dendrite tip

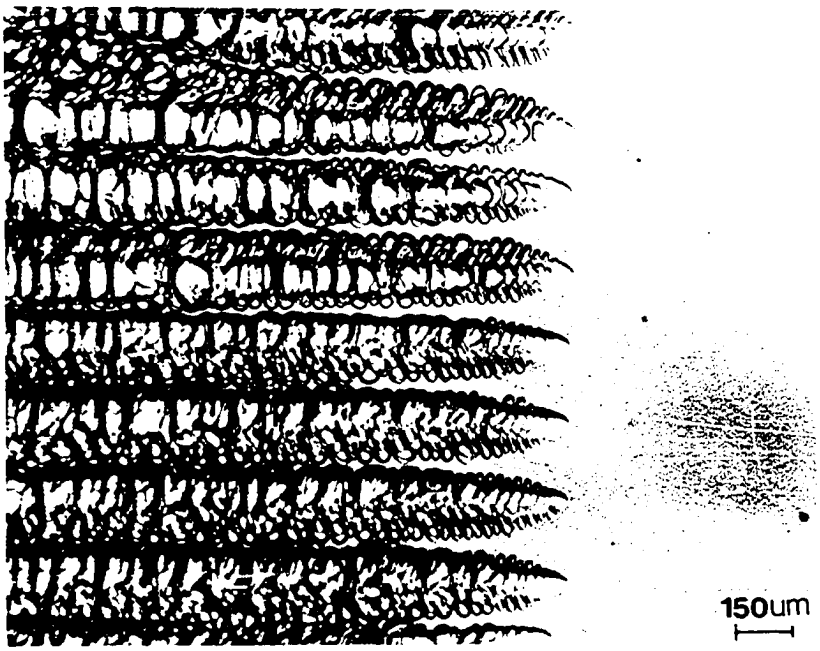

Figure III.2. An array of dendrites formed during the directional solidification of succinonitrite - 4 wt % acetone. V = 10.0 μm/s and G = 67 K/cm

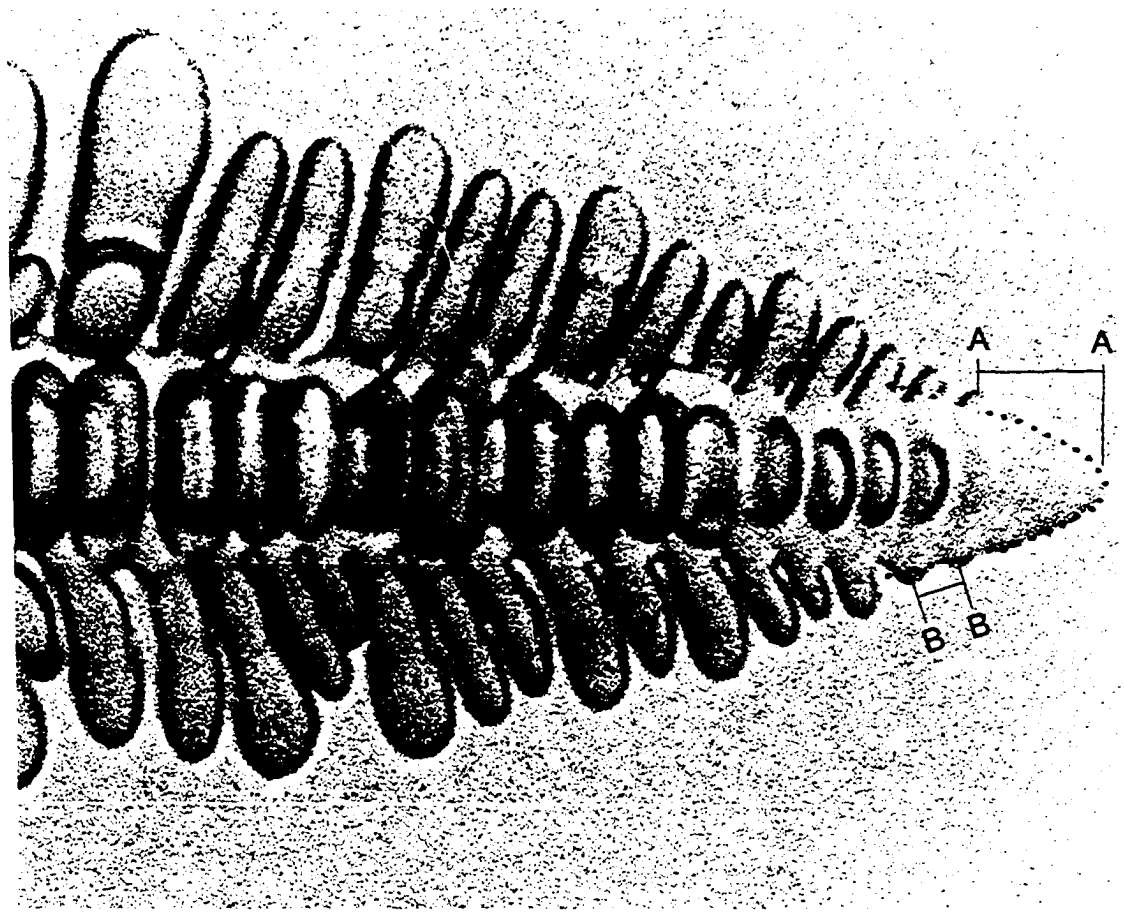

Figure III.3. An enlarged view of the steady-state dendrite tip shape in succinonitrile-acetone system. The dotted line is a standard parabola with the same radius of curvature as that at the dendrite tip. The distances AA = λ_p and BB = λ_2

matches with the parabola. All values of ρ were measured from micrographs taken from a <100> direction.

Although convection effects in these thin samples were not expected, experiments were carried out to determine if any convection was present in the liquid under low growth rate conditions. Inert silica spheres of 20 to 100 μm diameter were placed in the cell. There was no observed motion of these spheres during the entire solidification run. In another experiment, very fine inert gas bubbles were introduced into the liquid and again, no motion was observed during solidification. These results indicate that no observable convection effects were present in this study.

IV. STEADY-STATE GROWTH

A. Experimental Results

The experiments on the variation of λ_1, λ_2, λ_p and ρ at steady-state growth are presented to isolate the effects of (1) thickness of the sample, (2) growth velocity, (3) temperature gradient in the liquid at the interface and (4) alloy composition. All experimental results on steady-state growth are summarized in Appendix B.

1. Sample thickness

In order to eliminate the effect of sample thickness, a series of experiments was carried out with sample thicknesses of 50, 100, 150 and 500 μm. For each thickness, controlled solidification runs were carried out at velocities ranging from 1 to 100 μm/s. These results for G = 67 K/cm are shown in Figure IV.1. As the sample thickness was decreased, the dendrite tip radius and initial secondary arm spacing were decreased, whereas the primary dendrite arm spacing was increased. These variations were significant when the growth rate was less than 25 μm/s. At higher growth rates, the variations in λ_1, λ_2 and ρ were quite small. It was found that, for the range of velocities and temperature gradients studied, λ_1, λ_2 and ρ did not change when the sample thickness was 150 μm or more as shown in Figures IV.2(a) and (b). Consequently, all subsequent experiments were carried out with a thickness of 150 μm or more.

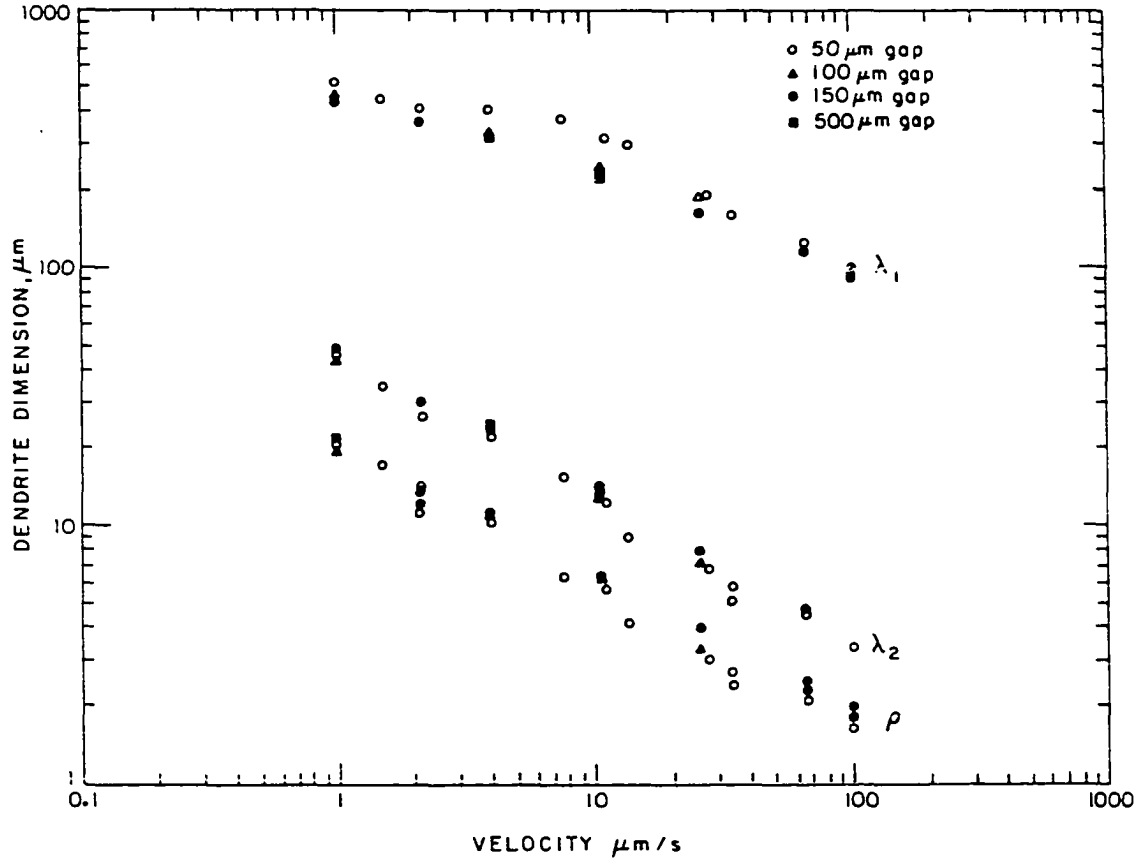

Figure IV.1. Variation of λ_1, λ_2 and ρ as a function of velocity at a constant temperature gradient of 67 K/cm. The effect of cell thickness on these parameters is also shown for cell thicknesses varying from 50 - 500 μm

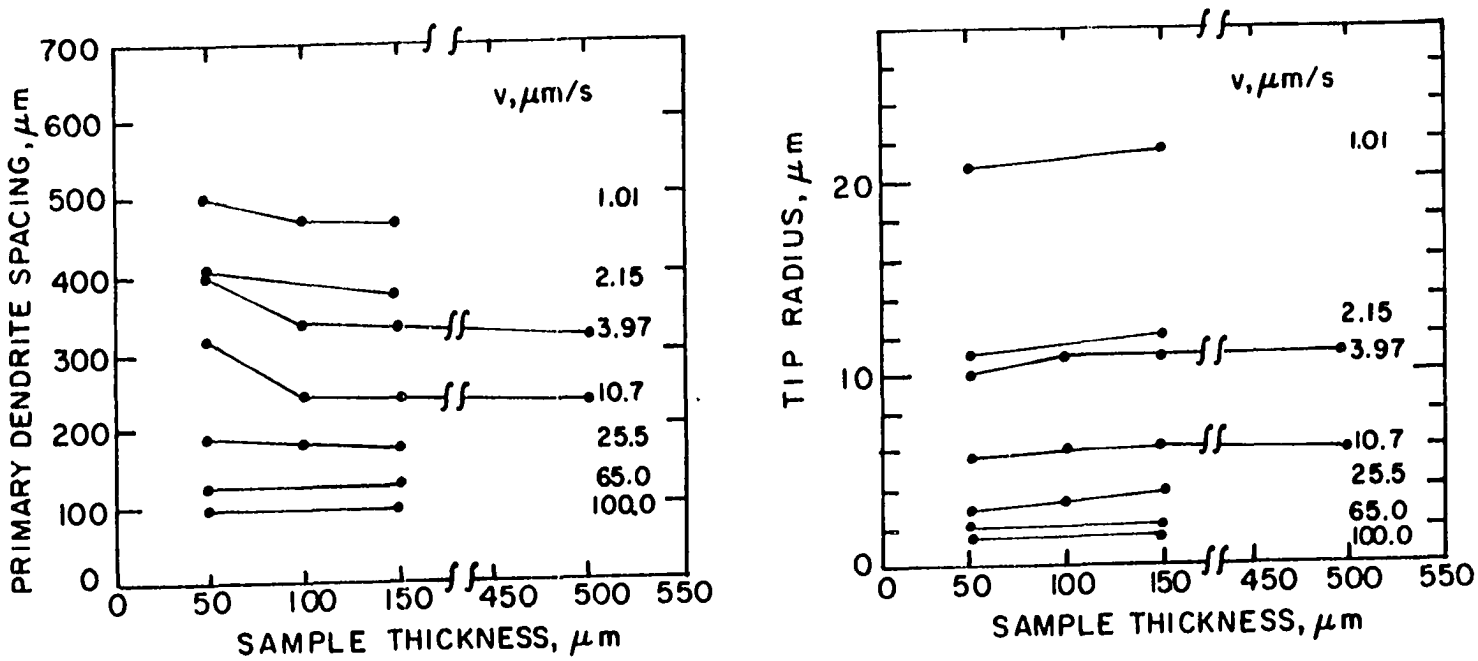

Figure IV.2. The effect of cell thickness on (a) primary dendrite spacing and (b) dendrite tip radius. G = 67 K/cm

2. Growth velocity effect

The experimental studies on the effect of growth velocity on steady-state characteristics were carried out at constant G = 67 K/cm and C_∞ = 4.0 wt % acetone. The growth velocity was varied from 0.4 to 100 μm/s. The variation in the interface structure as a function of V is shown in Figures IV.3 and IV.4. Figure IV.3(a) shows a cellular structure at low velocity. At V = 0.4 and 0.5 μm/s, many small cells with large tip radii developed at the solid-liquid interface. The tip region was found to deviate from a standard parabola for cellular structures. As V was increased to 0.68 μm/s, the length and spacing of cells increased, but tip radius decreased. As V was increased further, sidebranches developed and the interface changed to a dendritic structure, as shown in Figure IV.4. The tip radii of dendrites were measured very precisely with standard parabola curves which were drawn by a computer. As growth velocity was increased further, dendrites became finer in size and the spacings between the dendrites became smaller, as shown in Figure IV.4.

The variation in λ_1, λ_2, λ_p and ρ with controlled growth rates at constant G and C_∞ is shown in Figure IV.5. The variation in λ_1 on the log λ_1 versus log V plot is essentially linear for V between 4 and 100 μm/s. A least square linear regression gives the proportionality equation $\lambda_1 \alpha V^{-0.37 \pm 0.01}$. For $1 < V < 4$ μm/s, a small deviation from linearity is observed and λ_1 goes through maximum as the growth rate is decreased. Below V = 1 μm/s, λ_1 decreases sharply with the decrease in V and the interface changes from a dendritic to cellular structure.

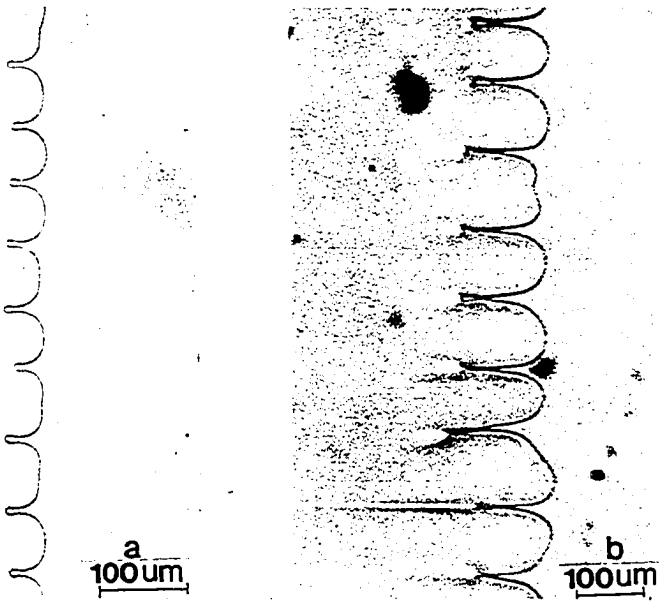

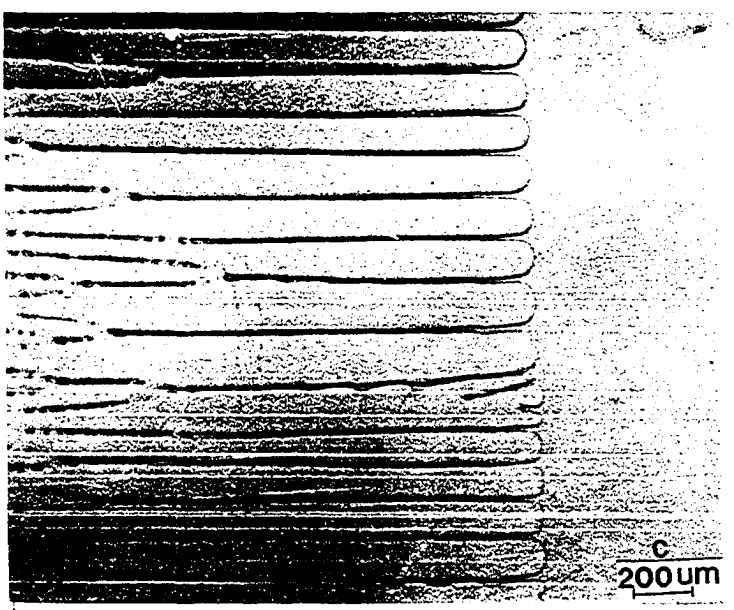

Figure IV.3. Cellular structures as a function of growth rate in succinonitrile - 4 wt % acetone. G = 67 K/cm. (a) V = 0.4 μm/s, (b) V = 0.5 μm/s, (c) V = 0.68 μm/s

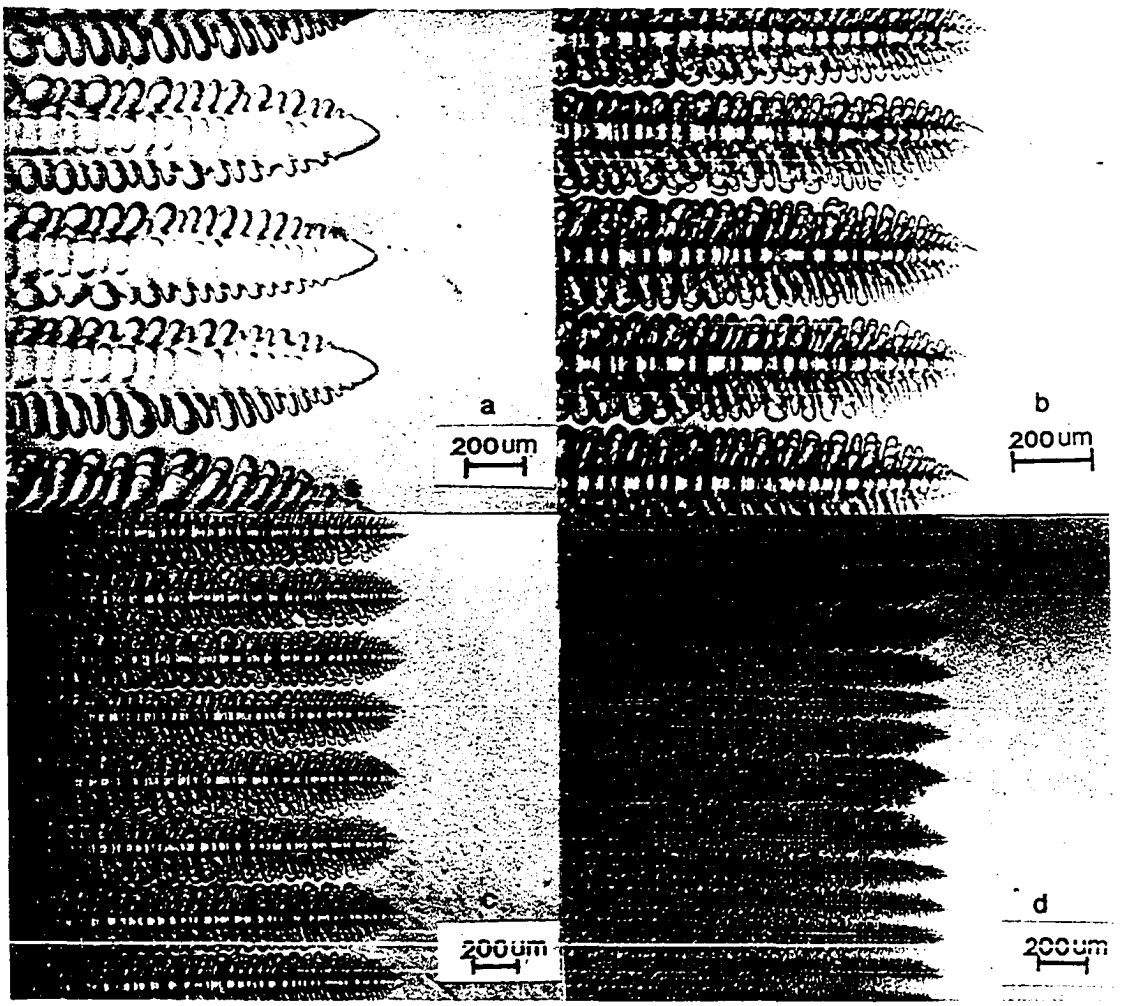

Figure IV.4. Dendritic structures as a function of growth rate in succinonitrile - 4 wt % acetone. G = 67 K/cm. (a) V = 1.17 μm/s, (b) V = 5.8 μm/s, (c) V = 10.7 μm/s, (d) V = 65.0 μm/s

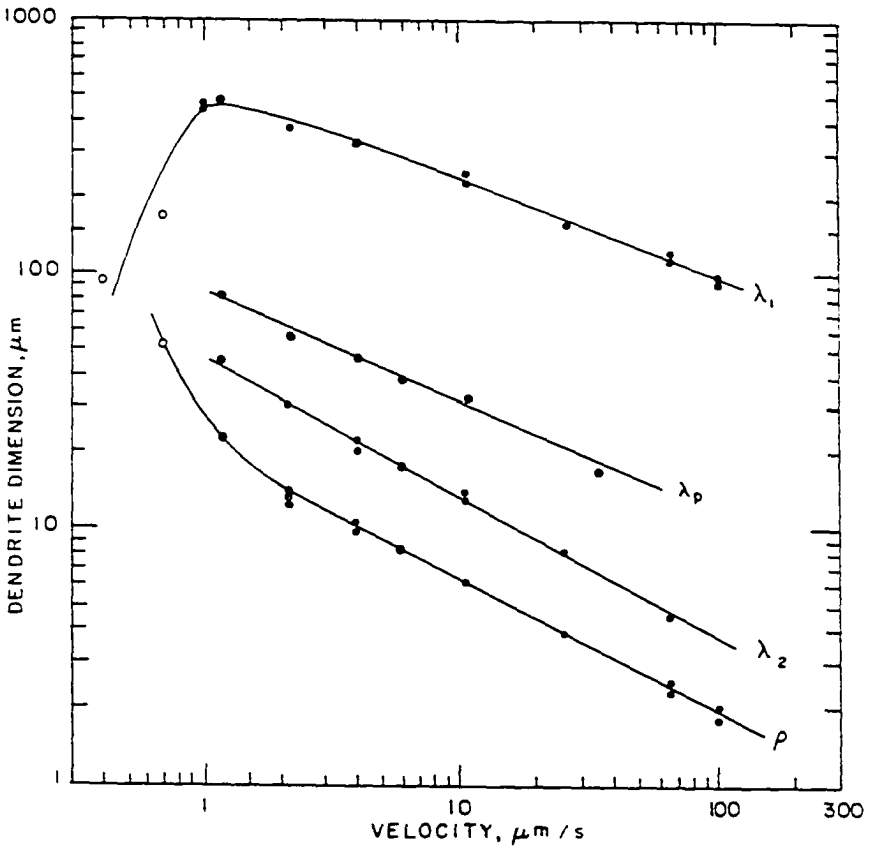

Figure IV.5. Variation of λ_1, λ_2, λ_p and ρ with growth rate, V, at G = 67 K/cm. Sample thickness = 150 μm

The λ_p, λ_2 and ρ were all found to decrease with V (Figure IV.5). The log-log plot of λ_p and V yields a straight line with the slope of -0.39 ± 0.03. The variation in λ_2 for $V \geq 1$ μm/s was found to be proportional to V^{-n} where $n = 0.56 \pm 0.02$. The variation in ρ for $V > 2$ μm/s was also found to be proportional to V^{-m} with $m = 0.53 \pm 0.02$. The measurements of λ_2 and ρ were made on the same dendrite for each experimental run. A least square regression of the experimental data gives the following relationship for $V > 2$ μm/s:

$$V\rho^2 = 441 \pm 30 \ \mu m^3/s \ . \qquad (19)$$

When V is less than 1 μm/s, ρ increases sharply with decreasing V and the tip shape begins to deviate from a parabola. The sharp increase in ρ corresponds with a sharp decrease in λ_1, as well as with the onset of the dendrite-to-cell transition.

The variation in dendrite or cell tip temperature as a function of velocity is shown in Figure IV.6 for succinonitrile - 4.0 wt % acetone solution, and the experimental results are summarized in Table IV.1. The dendrite tip temperature, like primary spacing, is found to go through a maximum. However, the velocity at which a maximum in tip temperature is observed is significantly different from the velocity at which a maximum in λ_1 is observed.

3. Temperature gradient effect

The effect of temperature gradient in the liquid on λ_1, λ_p, λ_2 and ρ was investigated under conditions of constant $C_\infty = 4.0$ wt % acetone,

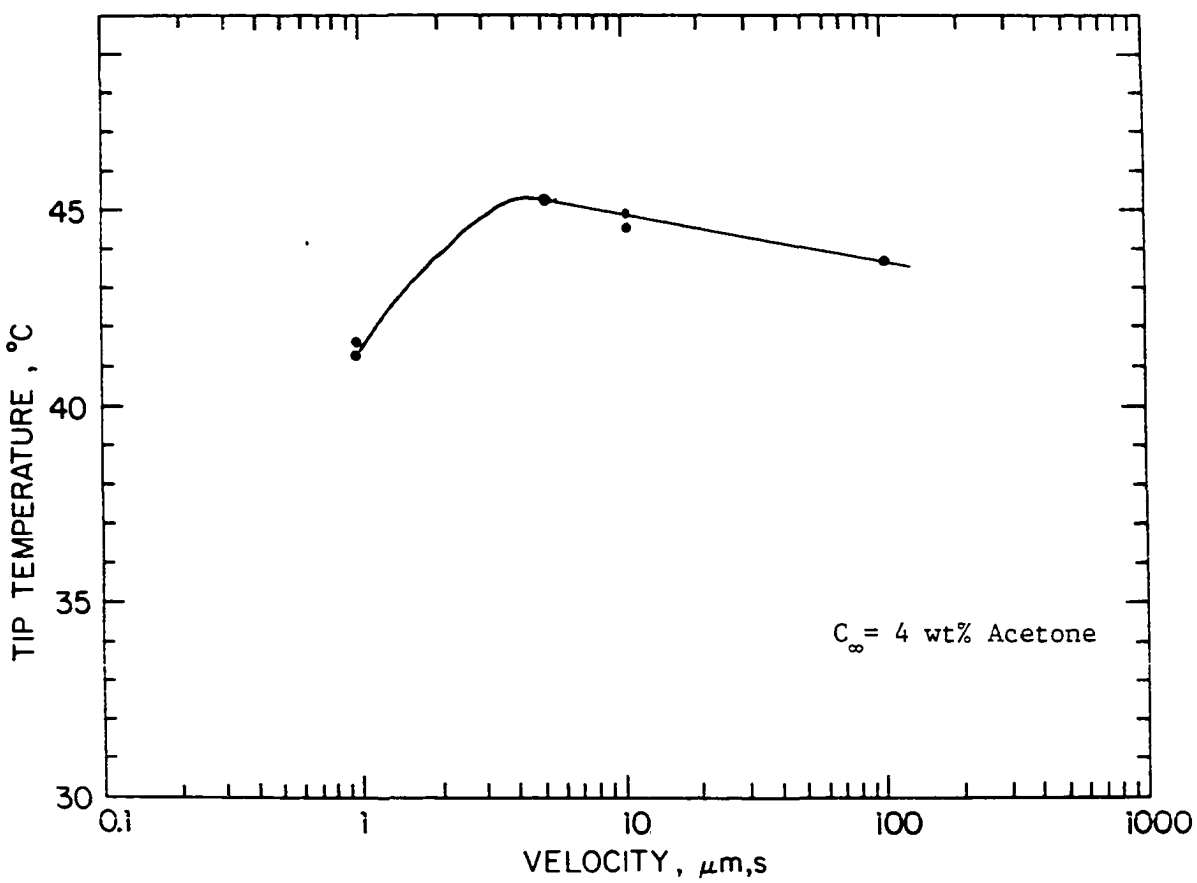

Figure IV.6. Variation of T_{tip} as a function of V

Table IV.1. Variation of T_{tip} with V and G for succinonitrile - 4 wt % acetone

V (μm/s)	G (K/cm)	T_{tip} (°C)
10	72.0	44.53
0.97	77.0	41.3
5.0	67.0	45.2
100.0	67.0	43.6

V = 10.7 μm/s and 65.0 μm/s. Because of the limitations in the experimental setup to control the temperature gradient, the temperature gradient at the interface could be varied from 35 to 116 K/cm. At this range of temperature gradient, only dendritic interface could be observed. Figure IV.7 shows the change in microstructure as the temperature gradient is increased. The results of λ_1, λ_2, λ_p and ρ, as a function of G, are plotted in Figures IV.8, IV.9 and IV.10.

The primary dendrite spacing decreases as G increases according to $\lambda_1 \propto G^{-a}$. The value of the exponent a depends on the velocity and is equal to 0.53 ± 0.02 at 10 μm/s and 0.43 ± 0.02 at 65 μm/s.

The variations of λ_p with G at V = 10.7 and 65.0 μm/s are shown in Figure IV.10. It was found that λ_p increased as the temperature gradient was decreased. A least square linear analysis gives the equations of $\lambda_p = G^{-a}$, where a are equal to 0.26 ± 0.10 and 0.20 ± 0.10 for V = 10.7 and 65.0 μm/s, respectively.

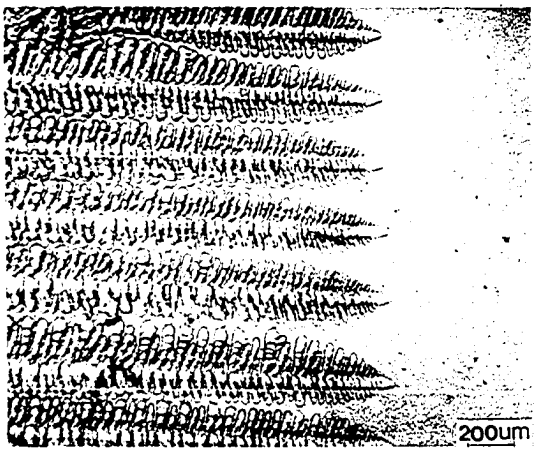

a

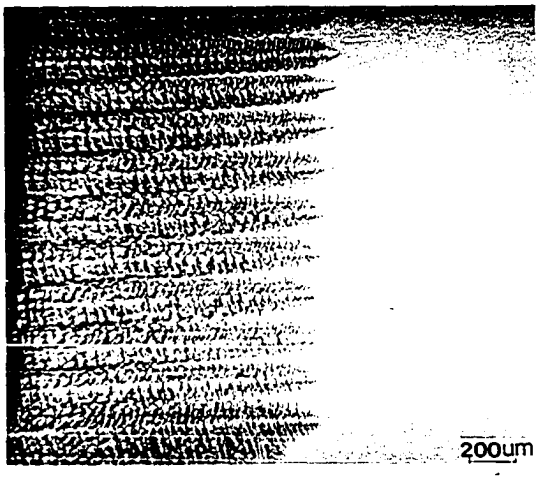

b

Figure IV.7. Dendritic structures as a function of temperature gradient in succinonitrile - 4 wt % acetone at V = 10.7 μm/s. (a) G = 35 K/cm, (b) G = 86 K/cm

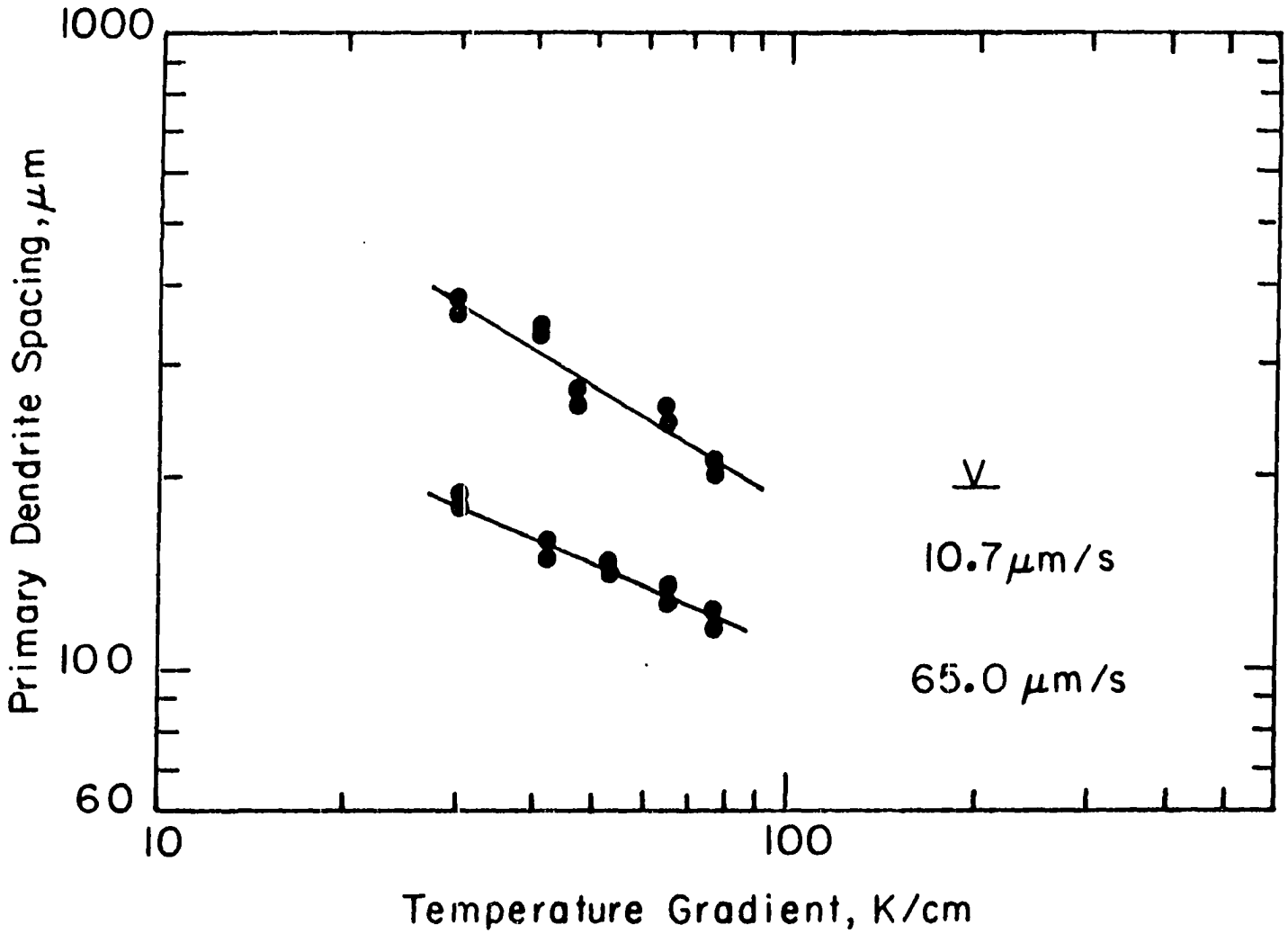

Figure IV.8. λ_1 versus G for succinonitrile - 4 wt % acetone at two constant V values

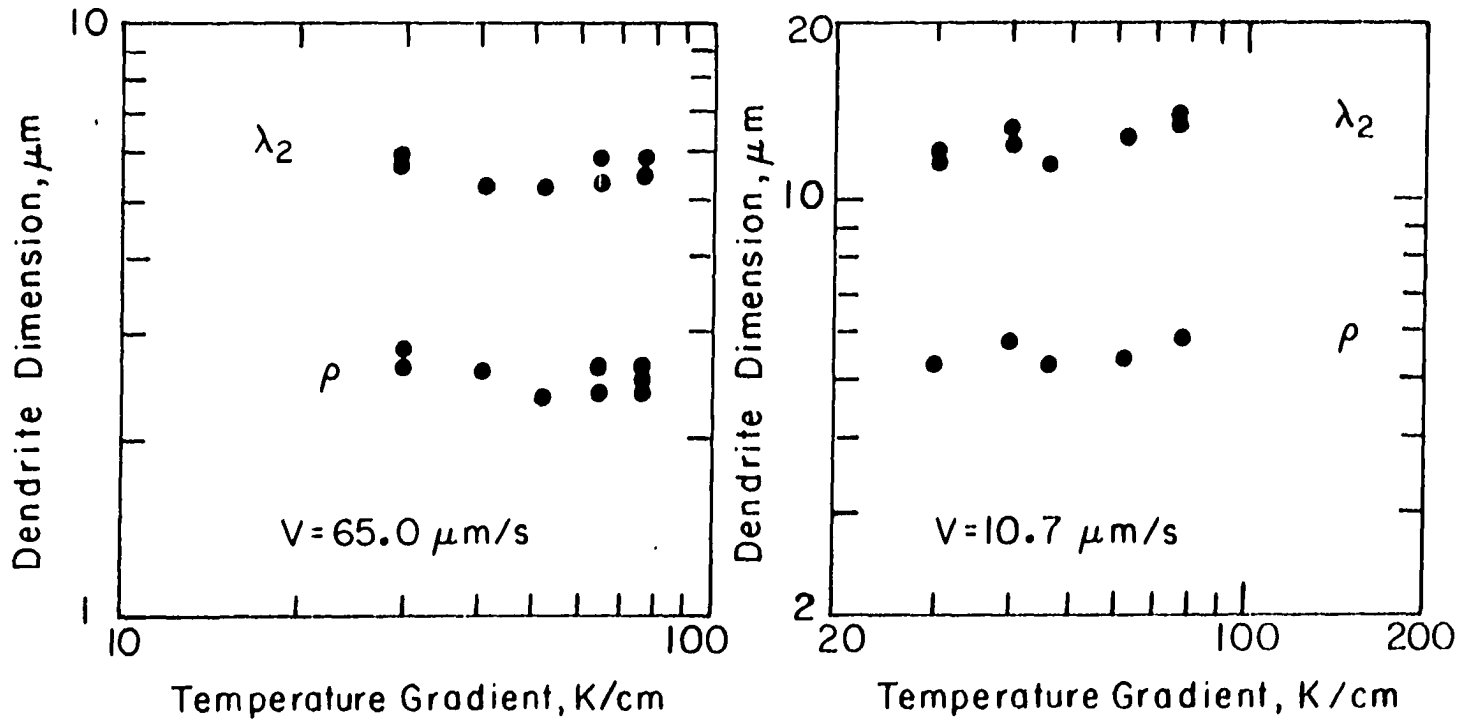

Figure IV.9. The effect of temperature gradient on λ_2 and ρ for constant growth rates of (a) 10.7 μm/s and (b) 65 μm/s

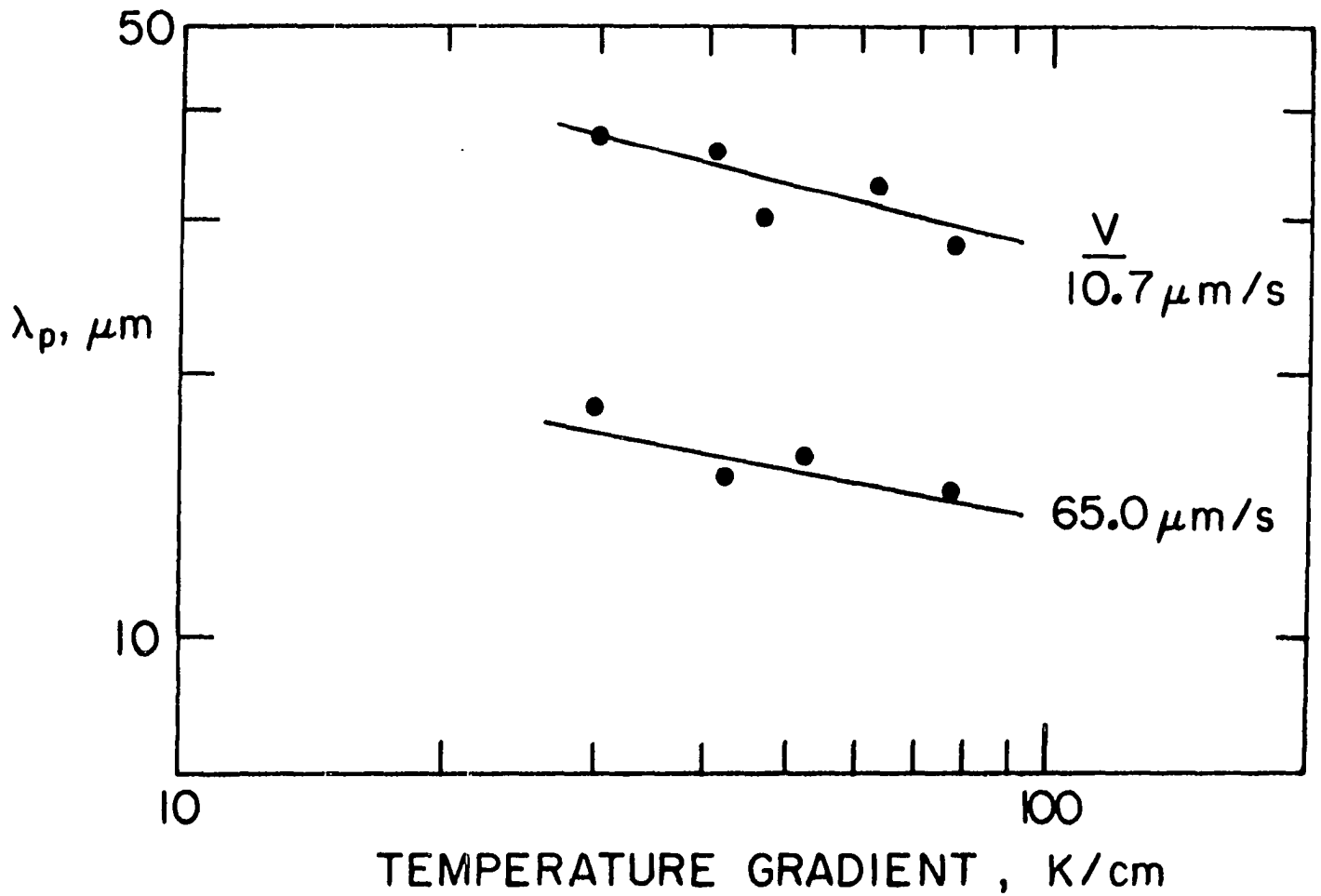

Figure IV.10. The effect of temperature gradient on λ_p at two constant V values for succinonitrile - 4 wt % acetone

4. Alloy composition effect

The experimental studies on the effect of alloy composition on λ_1, λ_p, λ_2 and ρ were carried out at G = 67 K/cm and V = 5.8 μm/s. Figure IV.11 shows the change in microstructure as the alloy composition is increased from 0.23 wt % to 4 wt %. At low composition, the cellular structure was observed, as shown in Figure IV.11(a). As the composition was increased, the interface changed from cellular to dendritic, as shown in Figure IV.11(b) and (c). The cell-dendrite transition occurred at C_∞ = 0.50 wt %.

Figure IV.12 presents the effect of composition variation upon λ_1, λ_p, λ_2 and ρ. The primary spacing, λ_1, increases as the alloy composition is increased. The increase in λ_1 is more rapid in the cellular region than in the dendritic region. The λ_2, λ_p and ρ were found to decrease with alloy composition. A least square linear analysis gives the equations $\lambda_2 \propto C^{-a}$ and $\lambda_p \propto C^{-b}$, where a and b are equal to 0.43 ± 0.04 and 0.36 ± 0.06, respectively. The tip radius was found to be proportional to $C^{-\bar{m}}$ for the range of alloy composition from 0.55 wt % to 4 wt % with $m = 0.48 \pm 0.05$. For $C_\infty < 0.55$ wt %, interface started to change from dendritic to cellular structure. In this region, the tip radius increased rapidly and the cell tip shape was found to deviate from parabolic shape.

B. Discussion

In this section, the experimental results on steady-state dendrite characteristics are discussed and compared with the existing theoretical

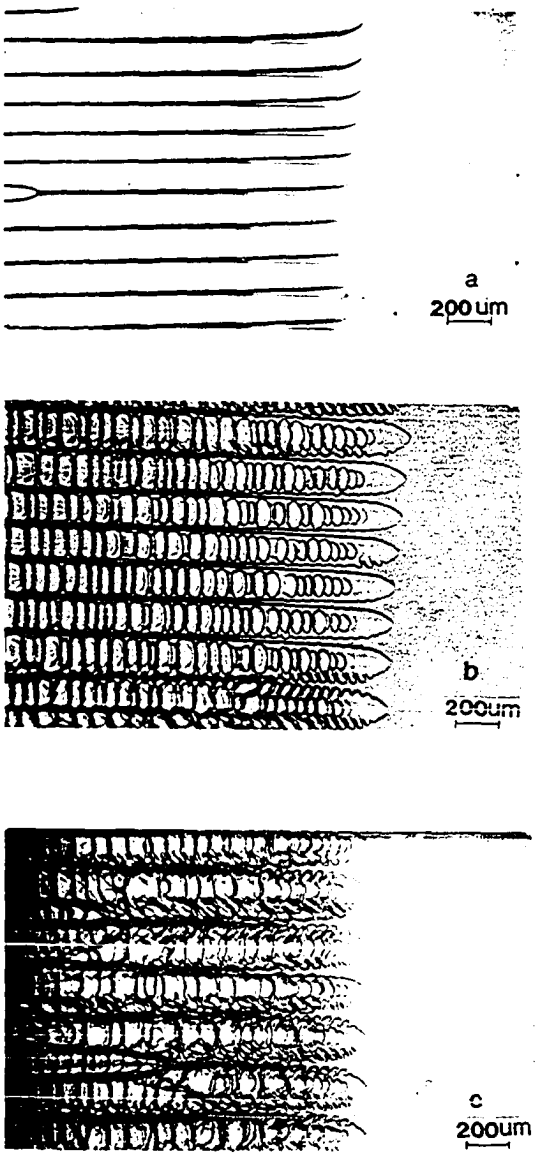

Figure IV.11. Interface structures change as a function of alloy composition at V = 5.8 μm/s and G = 67.0 K/cm. (a) C_∞ = 0.23 wt %, (b) C_∞ = 0.55 wt %, (c) C_∞ = 1.0 wt %

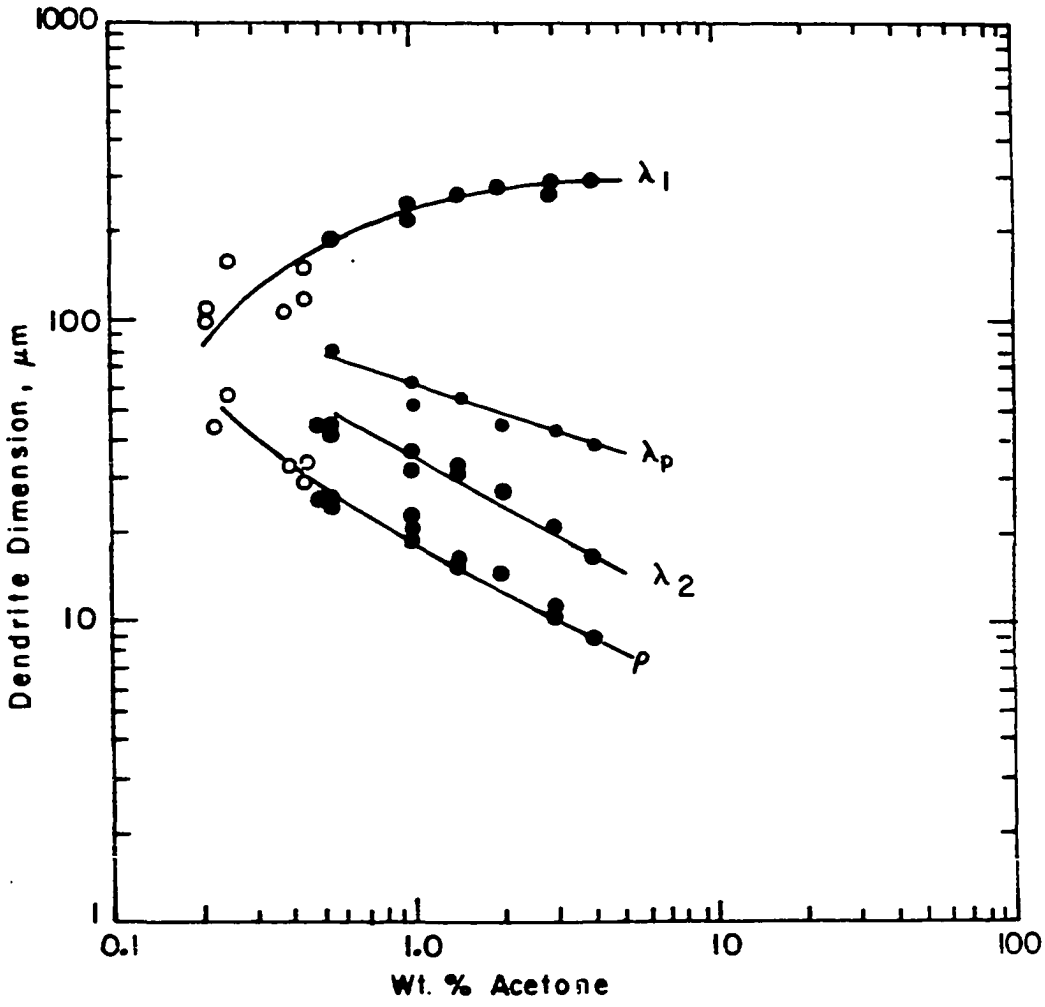

Figure IV.12. Variation of λ_1, λ_2, λ_p and ρ with wt % acetone at a thermal gradient of 67 K/cm and growth rate of 5.8 μm/s (o cell, • dendrite)

models. These dendrite characteristics are first separately presented as 1) dendrite tip characteristics, 2) secondary arm spacings and 3) primary arm spacing. Finally, the interrelationship between these characteristic spacings will be discussed, and the various correlations among the spacings, tip temperature and morphological features will be summarized.

1. Dendrite tip characteristics

1.1. Dendrite tip radius In Figure IV.13, the experimental data on ρ as a function of V is compared with the theoretical calculation Equation (11). Excellent agreement is obtained in both high and low growth rate regions. Also at the high growth rate region, the tip radius is independent of the imposed temperature gradient. The prediction of dendrite to cell transition velocity of Kurz and Fisher, $V = GD/k\Delta T_o = 0.78$, is in good agreement with the experimental result shown in Figure IV.13. Figure IV.14 shows the variation in P vs V. Again, a good agreement is found. Note that for a given value of P, two solutions for velocity are obtained. One solution represents the dendritic structure, whereas the other represents the cellular structure. For the experimental conditions described in this study, the minimum in P is associated with the maximum in λ_1 and also with the dendrite to cellular transition.

Figure IV.15 compares the experimental results of dendrite tip radius as a function of C_∞ with the theoretical calculation from Equation (11). The agreement is quite good within the dendritic region.

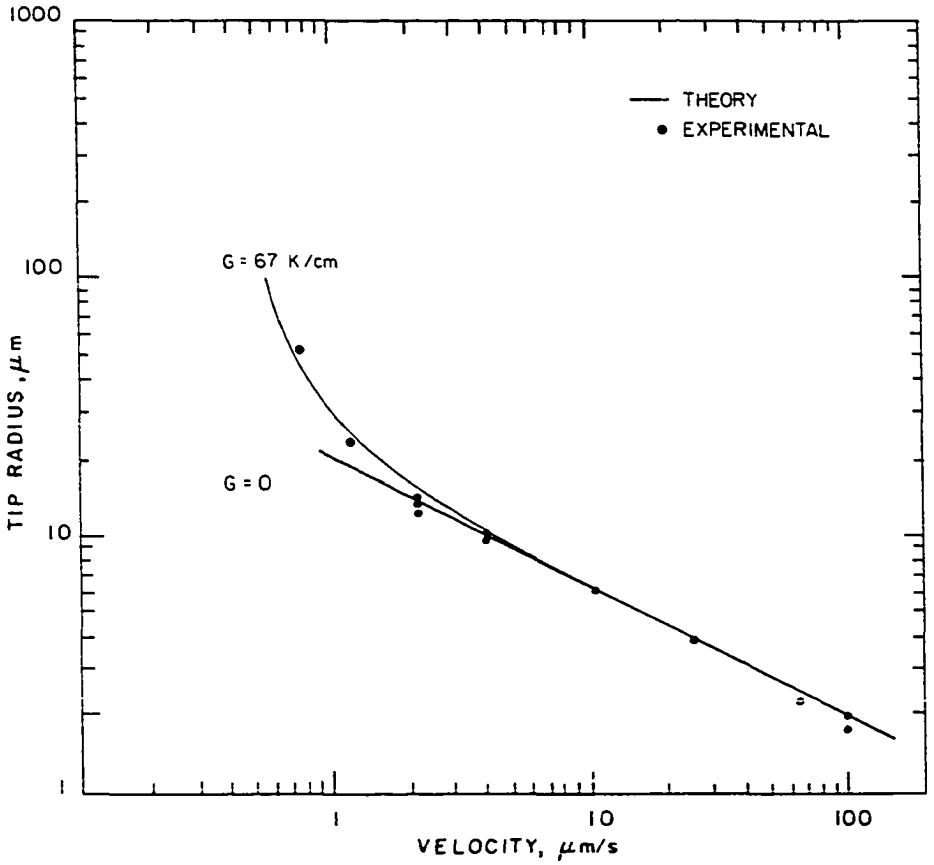

Figure IV.13. Variation of dendrite tip radius with velocity at G = 67 K/cm. Solid lines show theoretical values and the points are experimental results

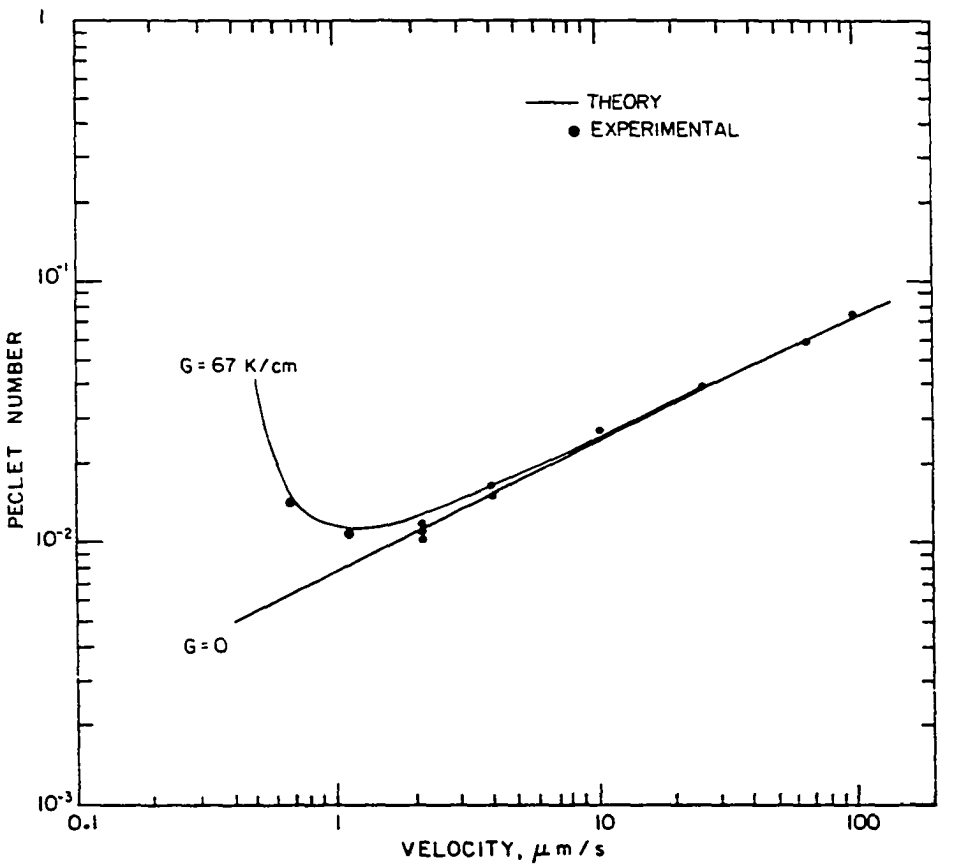

Figure IV.14. The variation of solute peclet number with growth velocity at a constant temperature gradient of 67 K/cm. Solid lines are theoretical results and points are experimental data

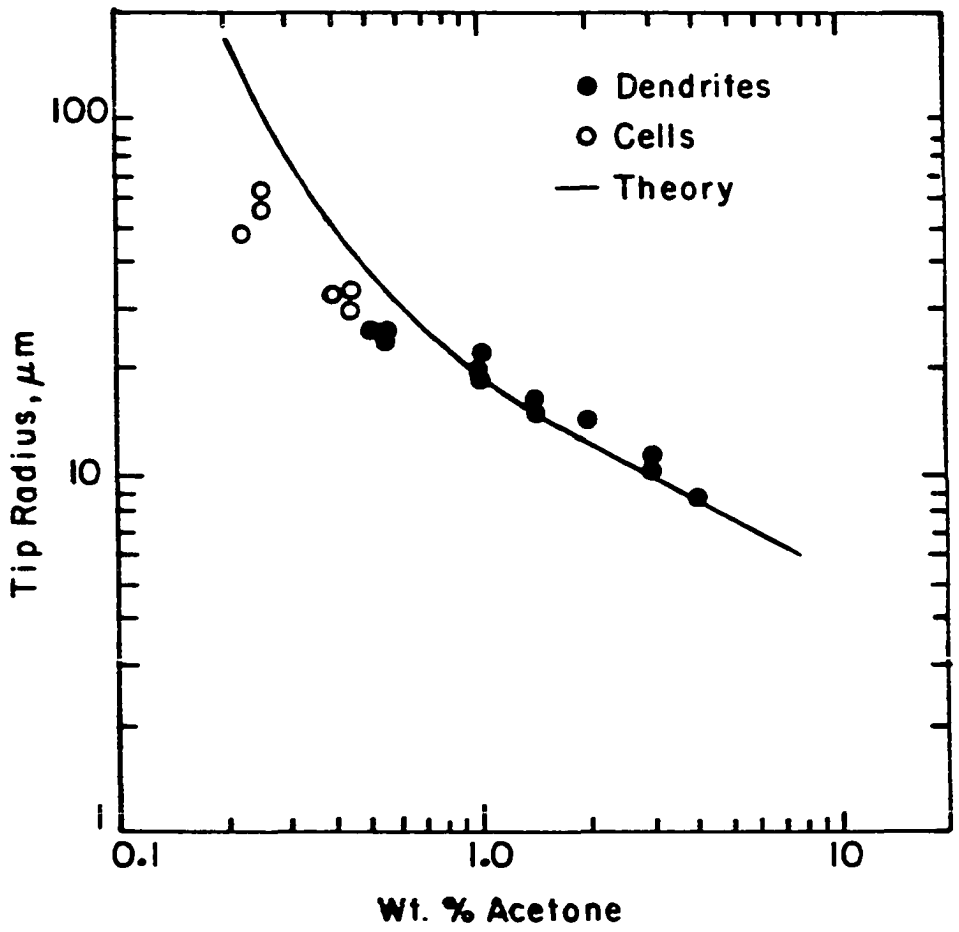

Figure IV.15. Variation of tip radius with composition at G = 67 K/cm and V = 5.8 μm/s

Some deviation is observed in the cellular region which is expected since the theory is based on a parabolic tip shape and the effect of neighboring dendrites or cells is assumed to be small. The cell tip shapes were found to deviate from a parabola, whereas all dendritic structures could be matched quite accurately with standard parabola. The dendrite-to-cell transition is observed around C_∞ = 0.5 wt % acetone, which compares well with the value of C_∞ = 0.54 wt % acetone predicted by Kurz and Fisher [38].

From Equation (11), it is noted that at high velocities, the surface energy term is important, whereas at low velocities, the temperature gradient effect is significant. However, for $2 < V < 100$ μm/s, both of these effects are small so that Equation (11) can be simplified and the results are as follow:

$$V\rho^2 = (2\gamma DL)/(\Delta Sk\Delta T_o) \qquad (20)$$

for $P \ll 1$. Using the properties given in Appendix A, the right-hand side of Equation (20) is equal to 411.1 $\mu m^3/s$. This value is in good agreement with the experimental result given by Equation (19). Equation (20) also shows that for dendritic structure, ρ is proportional to $(VC_\infty)^{-\frac{1}{2}}$. To check the validity of this equation, all of the experimental results on tip radius are plotted in Figure IV.16 as a function of VC_∞. In the dendritic region, all results are found to follow a straight line behavior. As an additional check, dendritic structures obtained under the same VC_∞ value, but with different

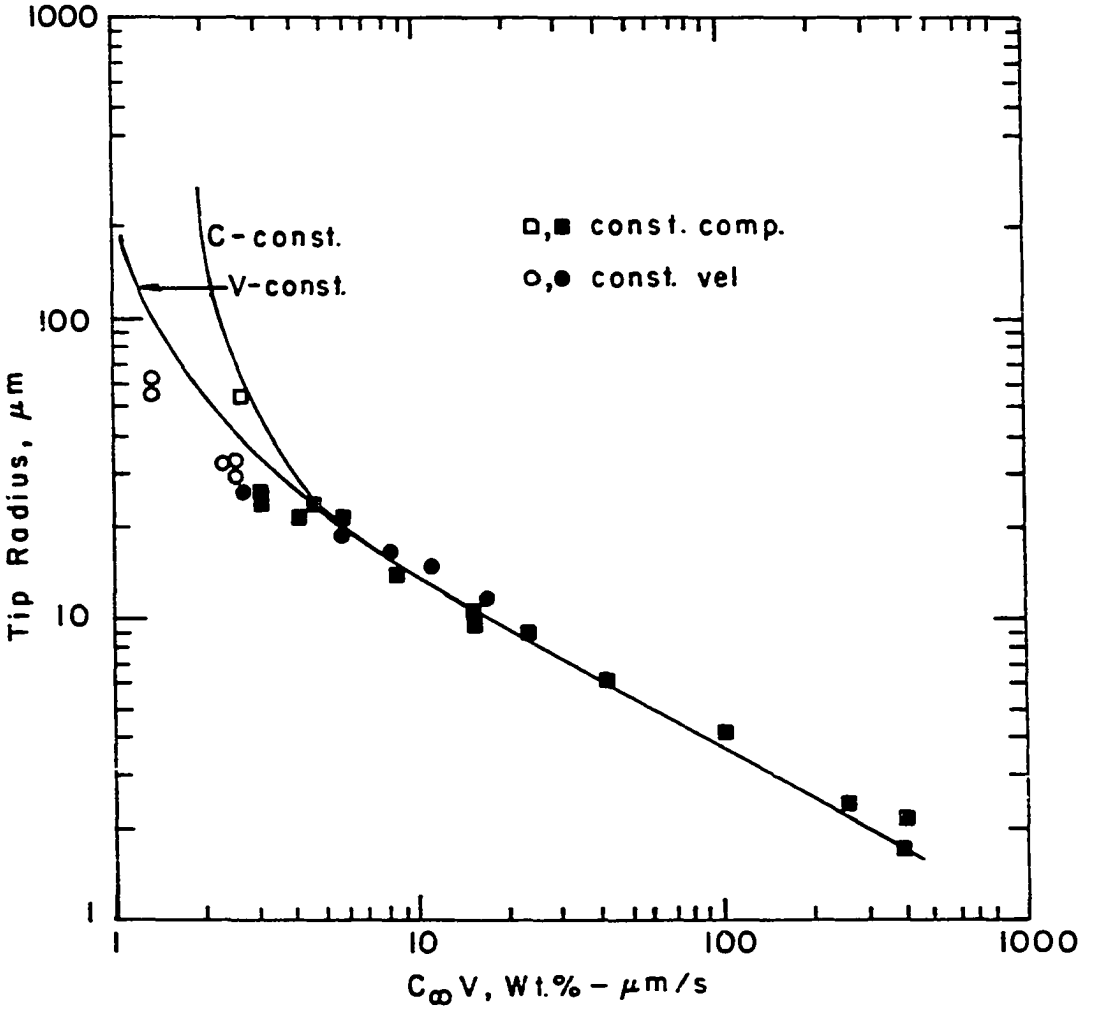

Figure IV.16. Variation of tip radius with VC_∞. Solid lines are theoretical results. Open and filled symbols represent cell and dendrite structures, respectively

combinations of V and C_∞ (V = 5.8 μm/s, C_∞ = 4.0 wt %, and V = 23.2 μm/s, C_∞ = 1.0 wt %), are superimposed in Figure IV.17. An excellent match in the dendrite tip region is found. Also, there does not appear to be a significant difference in the overall envelope of the dendritic microstructure.

The agreements between the experimental results and the theoretical model in the dendrite tip radius that are discussed above show that the dendrite tip radius under steady-state condition chooses a specific tip radius value which is predicted by the marginal stability criterion, Equation (10). Figure IV.18 shows the variation of dendrite tip radius with growth rate at G = 67 K/cm from Figure IV.13, and the theoretical results based on the minimum undercooling criterion. It shows that the tip radius values obtained from the minimum undercooling criterion are far below the experimental values, whereas the tip radius values obtained from the marginal stability criterion precisely coincide with the experimental values.

Although the marginal stability criterion seems to be valid for dendrite tip growth, it is not as yet clear why the radius values slightly smaller than the marginal stability values are not stable. A qualitative agreement has been presented by Langer [3] which shows that the dendrite tip radius will be driven toward the larger radius value due to the sidebranching activities until the radius value is just at the margin of instability. How this sidebranching activity affects the stability of dendrite tip is not yet very clearly understood. It would indeed be desirable to study experimentally how a dendritic

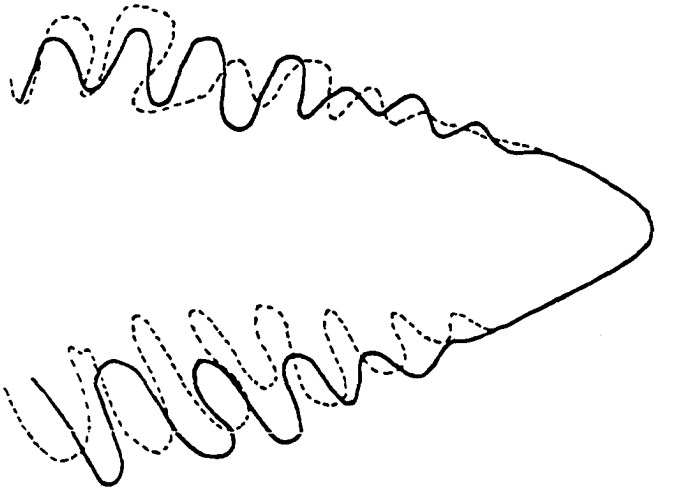

Figure IV.17. A superposition of two dendrite shapes obtained under identical VC_∞ value in succinonitrile - 4 wt % acetone solute. G = 6.7 K/mm. Solid line: V = 5.8 μm/s, C_∞ = 4 wt %; dotted line: V = 23.2 μm/s, C_∞ = 1 wt %

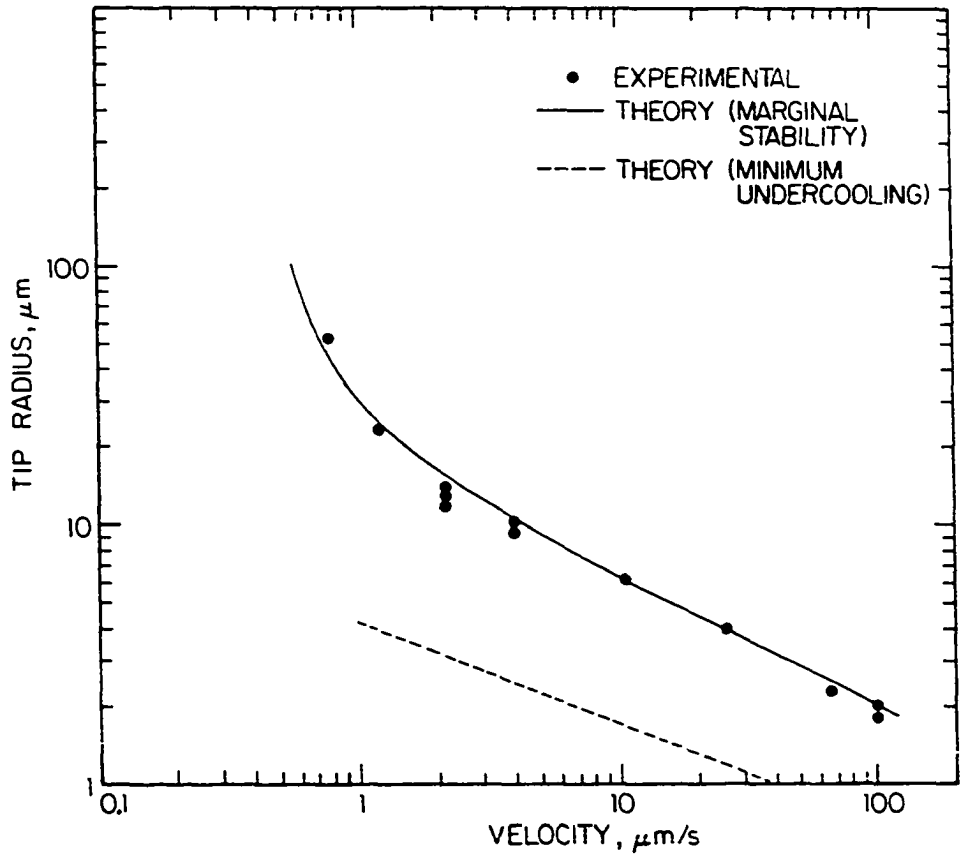

Figure IV.18. The experimental variation of tip radius with velocity is compared with the theoretical results based on the marginal stability criterion and on the minimum undercooling hypothesis

structure with a tip radius slightly larger or smaller than the marginally stable value adjusts under the externally imposed known steady-state growth conditions. These unanswered questions will be studied extensively in Part V.

The experimental observation of parabolic dendrite front and the excellent match between the theoretical and experimental results indicate that the concentration variation along the interface near the tip region is negligible for the values of velocities greater than 1 μm/s. We may estimate the variation of concentration, C_I, along the parabolic front by using the relationship [35]

$$C_I/C_\infty = (C_t/C_\infty) + (a_1\rho)(r^2/\rho^2) \tag{21}$$

where C_t is the solute concentration at the dendrite tip, r is the radial coordinate, and $a = -G/2mC_\infty$. For these experiments, G = 67 K/cm, $a_1 = 0.36$. For the range of velocities V = 1 - 100 μm/s, the value of the tip radius varied from 20 to 2 μm. Thus, $a_1\rho$ will vary from 0.72×10^{-4} to 0.72×10^{-3}. Since C_t/C_∞ is greater than one for $k_o < 1$, the second term in Equation (21) will be less than 0.1 for $r \sim 10 - 30\rho$. Thus, the dendrite tip is essentially an isoconcentrate for the experimental conditions used in this study. This is also confirmed by Equation (5), in which the magnitudes of both the gradient and the capillarity terms are negligible compared to the magnitude of the solute diffusion term. Consequently, Equation (5) reduces to the Ivantsov result [34] for the growth of an isoconcentrate dendritic

front. Furthermore, the dendrite tip stability criterion, given by Equation (10), reduces to the spherical approximation of Langer and Müller-Krumbhaar [46]. Thus, our results confirm the existence of a parabolic dendritic shape when the interface is isoconcentrate. Furthermore, our experimental data clearly shows the validity of the marginal stability criterion for the solute diffusion controlled dendritic growth in alloys.

These conclusions are valid for the range of V studied. When V becomes very large, i.e. when rapid solidification conditions are approached, the surface energy term becomes important so that the interface shape will deviate from a parabola. Also, the variation of k_o with V should be taken into account which may alter some of the conclusions reached in this paper.

1.2. Dendrite tip temperature Once the value of p is calculated from Equation (11), the value of the dendrite tip temperature may be obtained from Equation (5). Figure IV.19 compares the experimental results on dendrite tip temperature from Table IV.1 with results from theoretical calculation as a function of growth velocity. At high velocity where the gradient effect is negligible, the tip temperature increases with decreasing velocity. However, as the gradient effect becomes important, the tip temperature decreases with decreasing velocity. Excellent agreement between experimental results and the theory (Equation 11) is found at high velocity conditions.

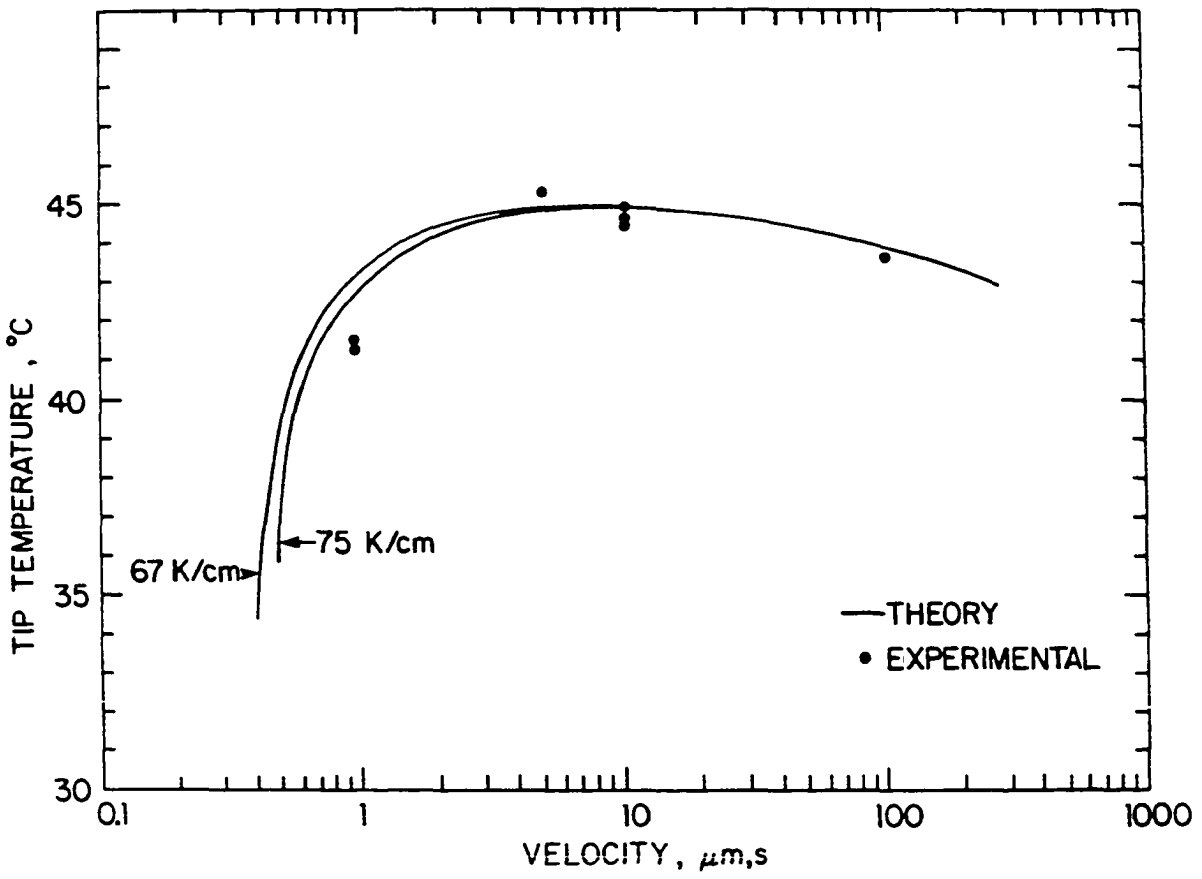

Figure IV.19. Variation of T_{tip} with V. Solid lines are theoretical results

2. Secondary branch characteristics

2.1. Initial spacing The experimental results on the variation of λ_2 and ρ as a function of V show that λ_2 and ρ have very similar dependence on V, which indicates that a simple relationship may exist between λ_2 and ρ. Figure IV.20 shows the variation of λ_2/ρ with velocity and it is found that $\lambda_2/\rho = 2.2 \pm 0.03$ for all velocities studied. This relationship was found to be independent of any changes in the temperature gradient. Even during the preliminary studies on λ_2 and ρ as a function of sample thickness, λ_2/ρ was always found to obey this relationship for all sample thickness studied, even though λ_2 and ρ varied individually for small thickness. Furthermore, the results of λ_2 and ρ, as shown in Figure IV.12, show that λ_2 and ρ have a similar dependence on composition. In Figure IV.21, all results of λ_2/ρ with V and C_∞ are combined together and it is found that a scaling law between λ_2 and ρ is obtained, i.e. $\lambda_2/\rho = 2.0$ over a wide range of variation in V, G and C_∞.

The experimental observations during steady-state growth clearly showed that as the sidebranches formed, they did not alter the macroscopic shape of the dendrite front. Also, the spacing of the nonlinear perturbations that developed initially along the sides was related to ρ. The relationship between λ_2 and ρ obtained in this experiment is found to agree very well with the results predicted by Langer and Müller-Krumbhaar [46], but the value of constant is lower than the ones obtained from Huang and Glicksman [25] and Honjo and Sawada [47]. Nevertheless, such a scaling law between λ_2 and ρ seems

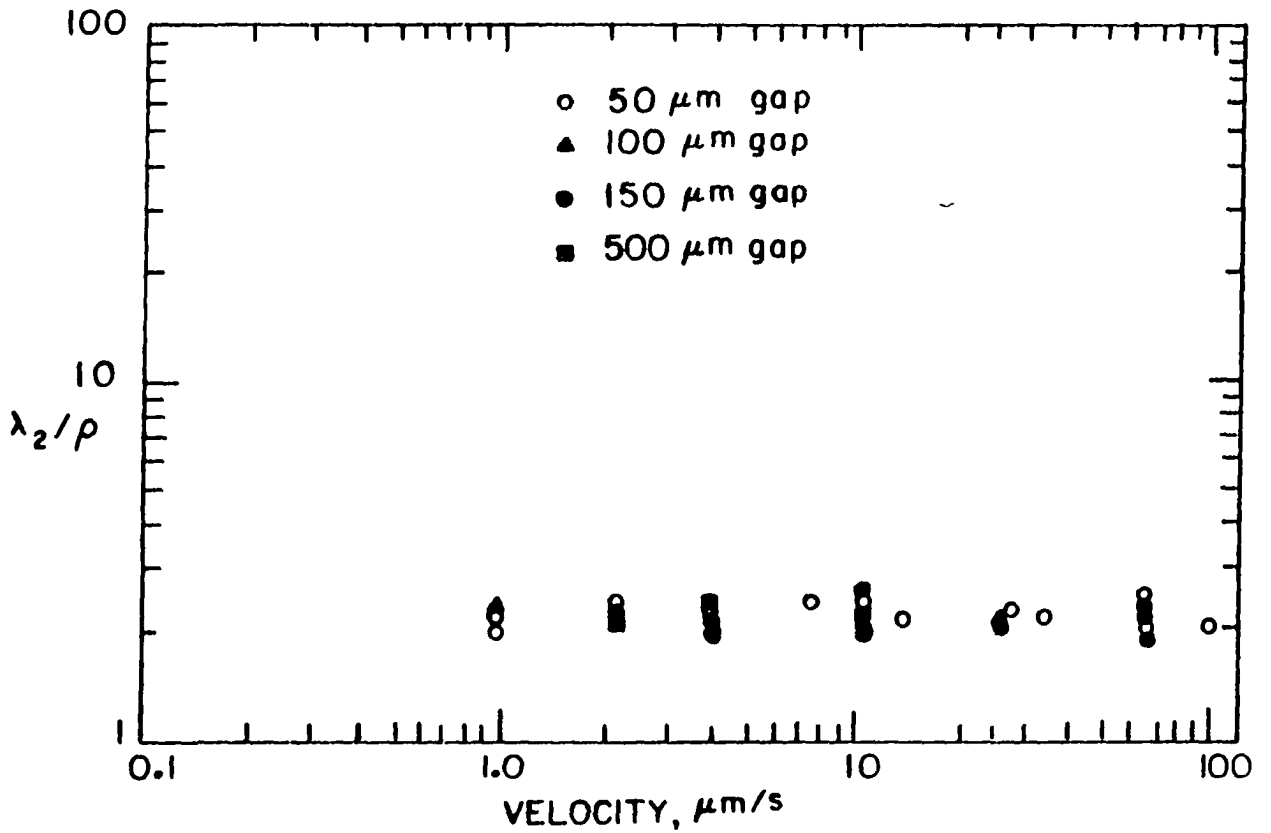

Figure IV.20. The variation of λ_2/ρ as a function of velocity. The results for all velocities, temperature gradients, and cell thicknesses are included

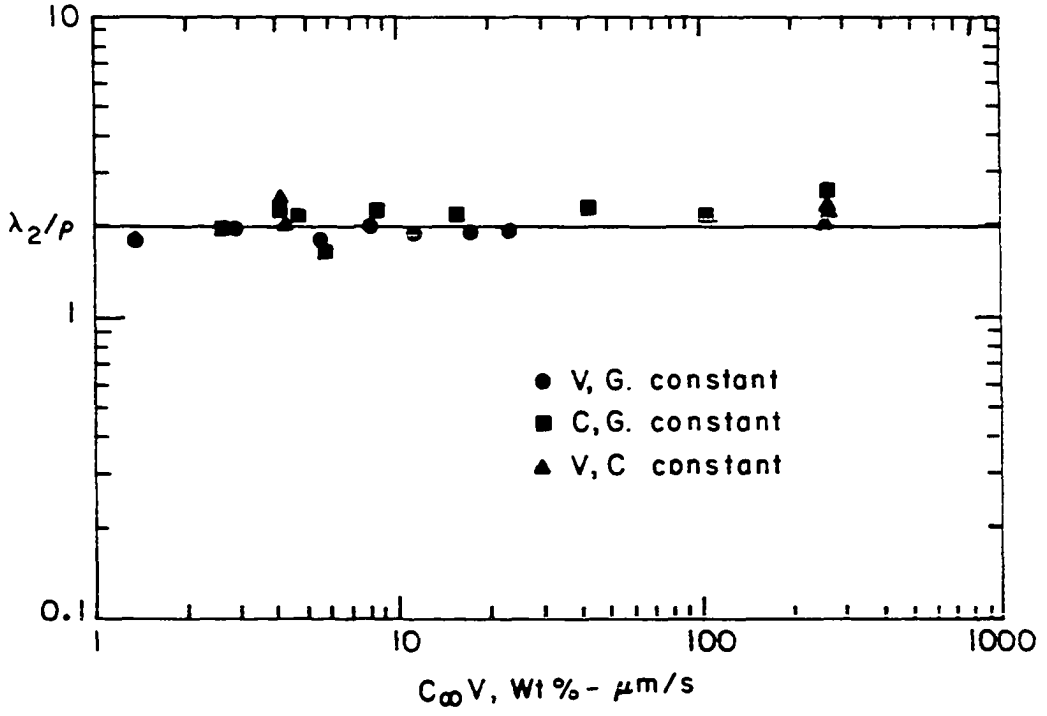

Figure IV.21. Variation of λ_2/ρ with VC_∞. All results for velocities, temperature gradient and composition variation are included

to be a fundamental characteristic of the dendritic structure, although the value of constant appears to depend slightly upon the experimental conditions which give rise to a dendritic structure.

The experimental results on the effect of G have shown that initial secondary dendrite spacing is independent of temperature gradient. Consequently, λ_2 is a function of C_∞ and V only. Using the scaling law $\lambda_2/\rho = 2.0$, the variation of λ_2 for small peclet number conditions can be represented as

$$\lambda_2^2 = 8\gamma DL/V\Delta T_o \Delta S \ . \qquad (22)$$

The results of Equation (22) are compared with the experimental data in Figure IV.22 and good agreement is found.

2.2. Initial perturbation The dendritic growth phenomenon is characterized by a dual phenomena in which the dendrite tip propagates in a steady-state manner, whereas time dependent evolution and propagation of instabilities occur at the side of a dendrite. The steady-state dendrite tip characteristics are now well understood in that the dendrite tip radius is found to be controlled by the marginal stability criterion obtained from a linear stability analysis. The sidebranch formation, however, is a nonlinear phenomenon and it is assumed that the formation of sidebranches does not affect the steady-state dendrite growth process. The coupling between these two processes may be weak, nevertheless, it does exist since it has now been well established that the initial sidebranch wavelength is twice the dendrite tip radius. Consequently, there is a definite coupling between the steady-state

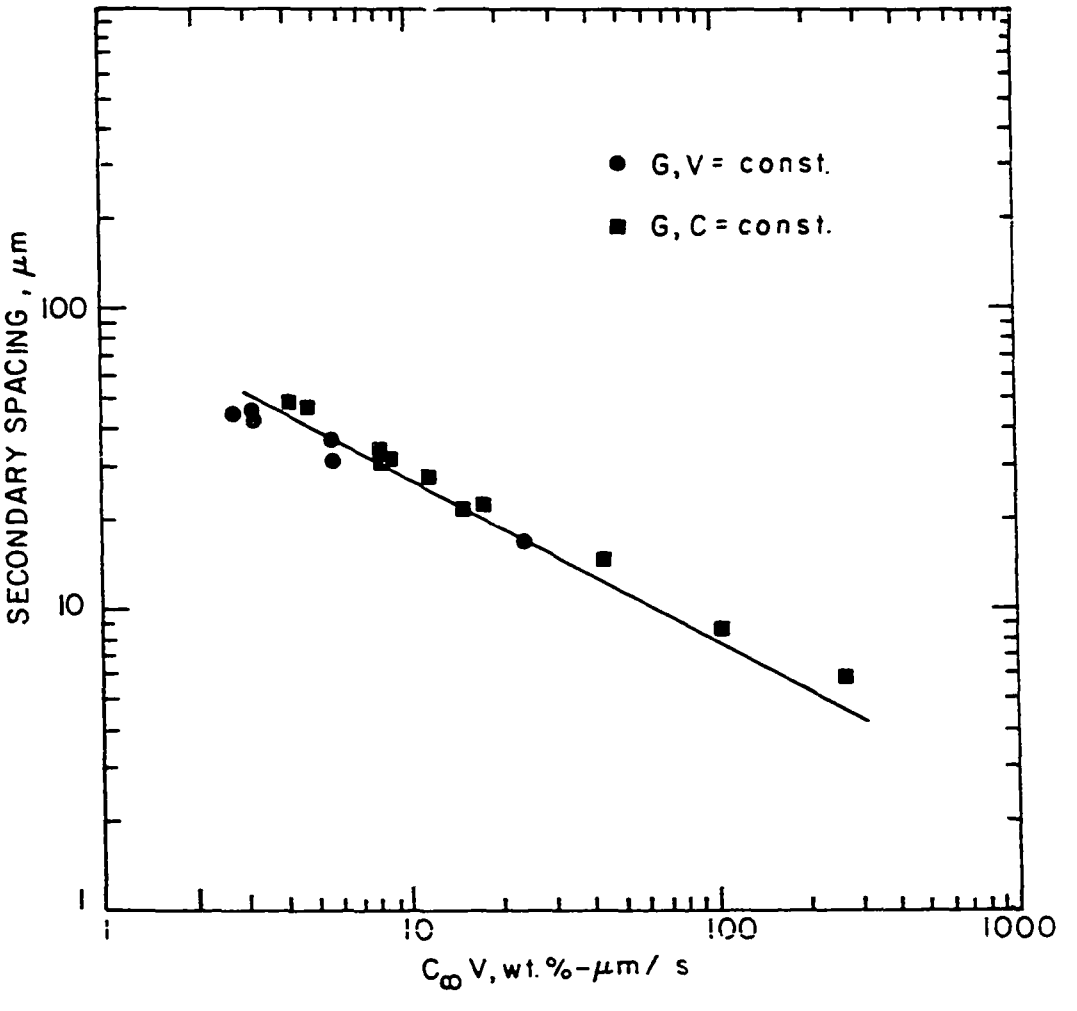

Figure IV.22. Variation of secondary dendrite spacing as a function of VC_∞. The solid line is the theoretical result obtained for $\lambda_2/\rho = 2.0$

dendrite tip growth and the non steady-state sidebranch formation. Another parameter of the sidebranch instability which has a definite value is the location of the first sidebranch perturbation. The value of λ_p has been found to be uniquely established for given growth conditions. It would thus be desirable to investigate if a scaling behavior is established by λ_p with respect to λ_2 or λ_1.

Huang and Glicksman [25], in their studies of free dendrite growth from a pure undercooled melt, found that the value of λ_p/ρ decreased as the undercooling was increased. No detailed quantitative study of λ_p was carried out by these authors. In our directional solidification studies, it is found that λ_p decreases as V, G or C_∞ are increased. The value of λ_p will now be related with other steady-state characteristics.

There are two independent steady-state lengths that are observed during the dendrite growth process, i.e. λ_1 and λ_2. The dendrite tip radius is scaled to λ_2 and has a magnitude of λ_2/ρ. There is no scaling law observed for λ_2 and λ_p. Furthermore, no scaling law is observed between λ_1 and λ_p. However, the experimental results show that $\lambda_p \propto (\lambda_1\lambda_2)^{\frac{1}{2}}$. In order to check this relationship, $\lambda_p/(\lambda_1\lambda_2)^{\frac{1}{2}}$ is plotted in Figure IV.23 as a function of V, G and C_∞. It is clear that all the experimental results show a scaling law of the form

$$\lambda_p \simeq \frac{1}{2} (\lambda_1\lambda_2)^{\frac{1}{2}} .$$

Note that, in Figure IV.23c, the ratio increases as the composition is lowered. This is the region in which dendrite-to-cellular transition takes place. This is seen from the microstructures shown in Figure IV.11.

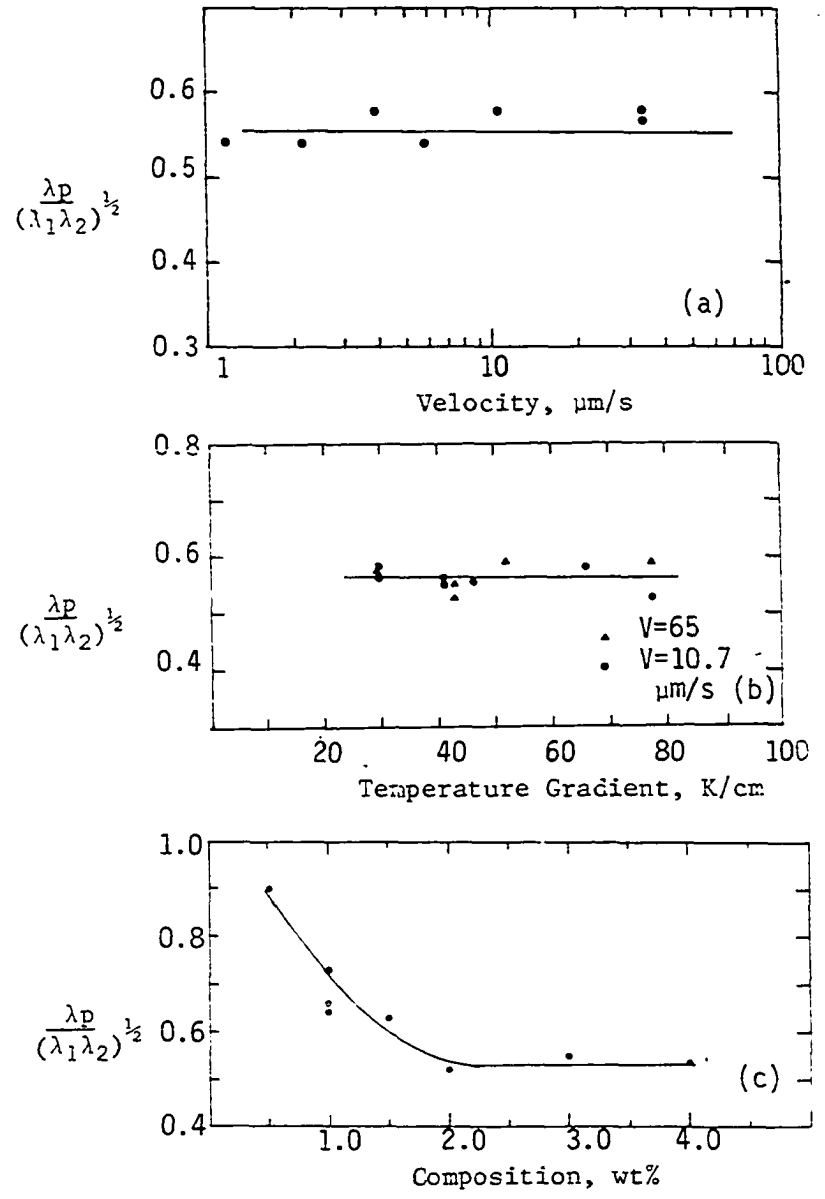

Figure IV.23. Variation of $\lambda_p/(\lambda_1\lambda_2)^{1/2}$

a) with V at G = 67.0 K/cm and C_∞ = 4 wt %,
b) with G at V = 10.7 μm/s and C_∞ = 4 wt %, and
c) with C_∞ at V = 5.8 μm/s and G = 67.0 K/cm

3. Primary arm spacing

Since the successful prediction of the theory on λ_2 as a function of V and C_∞ as shown in Figure IV.22, the relationship of λ_1 and ρ as a function of V is plotted in Figure IV.24. It shows that the ratio of λ_1 to ρ increases with V. For $V > 4$ μm/s, the variation is linear on the log-log plot. At low velocity region where the interface becomes cellular, the ratio λ_1/ρ decreases sharply with decreasing V. Because the primary spacing is a function of V, C_∞ and G, the values of the slope on the log λ_1/ρ versus log V, log G and log C_∞ are different. Consequently, no scaling law is observed between λ_1 and ρ. The ratio λ_1/ρ is more complicated than the ratio λ_2/ρ because it is a function of V, C_∞ and G. In order to predict the theory of λ_1 as a function of the growth conditions, the relationship between λ_1 and ρ has to be known quite accurately. All three theoretical models on primary spacing [38, 57, 58] which have already been discussed in Part II, predicted the λ_1 as a function of G, V and C_∞ by first developing the relationship between λ_1 and ρ. These three models will thus be compared to our experimental results.

Figure IV.25 compares the experimental results with the theory of Hunt [57], given by Equation (14), and with the high growth rate regime result (Equation 16) of Kurz and Fisher [38]. A poor correlation is obtained between the experimental results and both theories. In Hunt's theory, the value of velocity at maximum λ_1 is much smaller than the value from experimental results; also, the λ_1 values are far below the experimental value. The values of λ_1 from Kurz and Fisher are too high

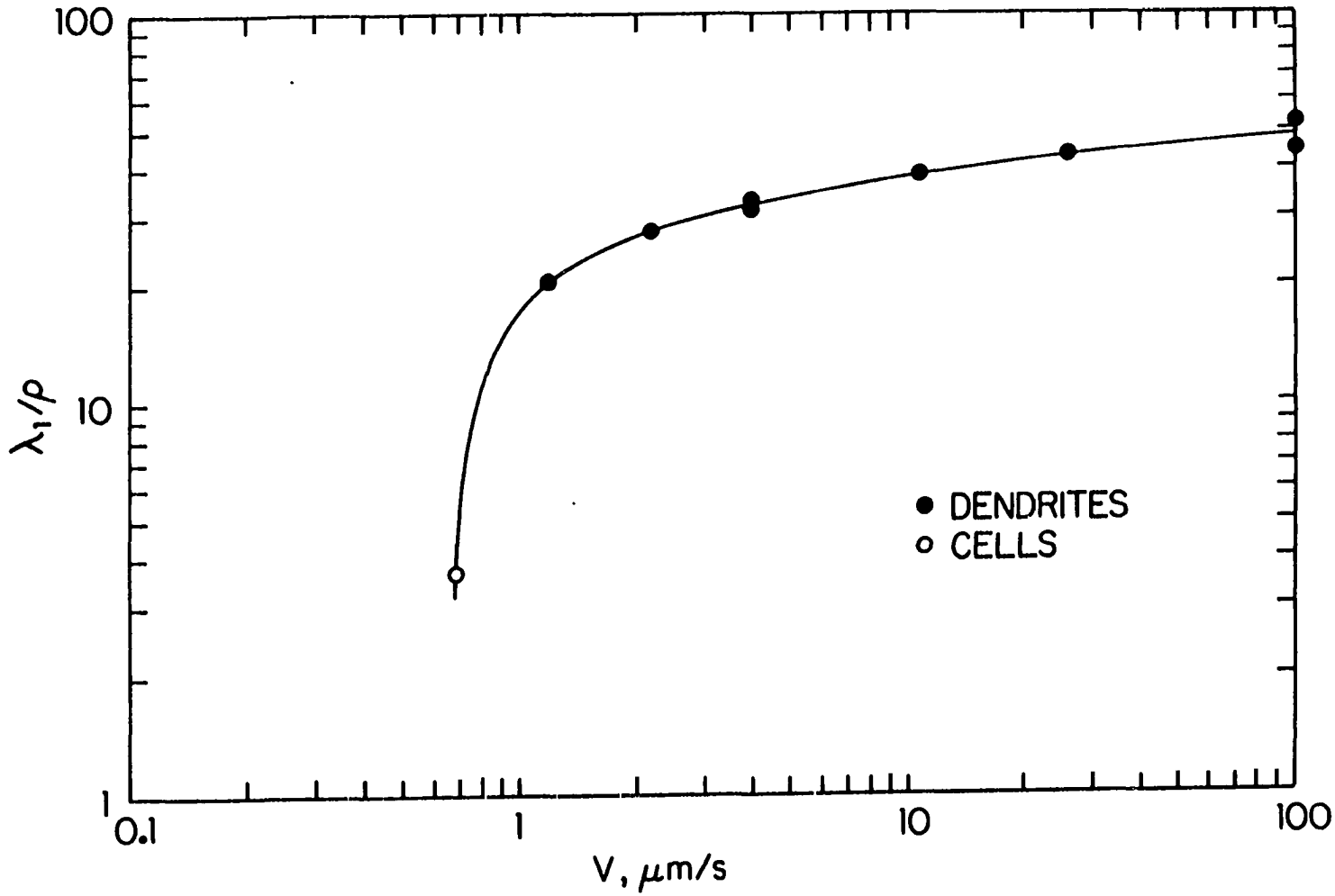

Figure IV.24. Variation of λ_1/ρ with V at G = 67 K/cm

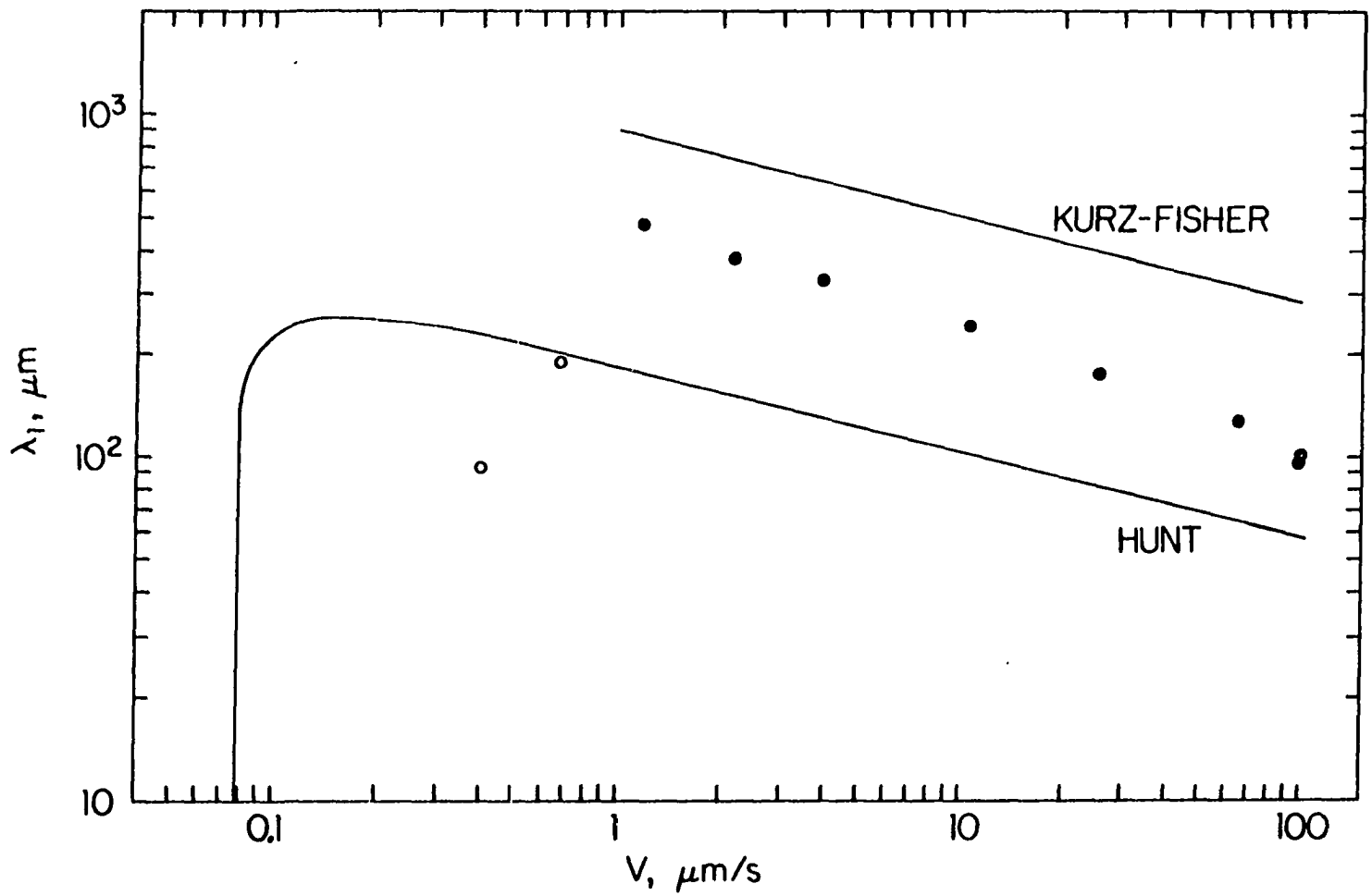

Figure IV.25. Comparison of the existing theories of primary spacing with the experimental data in succinonitrile - 4 wt % acetone system. G = 67 K/cm (o cell, o dendrite)

from experimental results. They predict the transition velocity from high to low regime at $V = V_{cr}/k = 0.783$ μm/s, which agrees well with the experimental results on dendritic-to-cellular transition velocity. However, Kurz and Fisher predict that λ_1 will increase sharply with decreasing V near $V = V_{cr}/k$. Experimental results, in fact, show just the opposite behavior in that λ_1 decreases sharply as V is decreased in the cellular regime.

Figure IV.26 compares the results of experiments and theory of Trivedi [58] as a function of V. The correlation between the theory and the experimental data is found to be quite good. The theory also predicts a maximum in λ_1 as a function of velocity and the velocity at which the maximum in λ_1 agrees quite accurately with the predicted value.

The experimental results on the effect of composition on primary spacing are shown in Figure IV.27. The primary spacing increases more rapidly with composition in the cellular region than in the dendritic region. Theoretical calculations, using Equation (17), are shown for comparison. Good agreement is found for the range of composition studied.

Figure IV.28 compares the experimental results on λ_1 as a function of G with the theory. The agreement between the theory and the experimental data is not quite good. The theoretical values of λ_1 at $V = 10.7$ μm/s agree quite well with the experimental results, but the slope predicted by the theory is a little lower than the one from the experimental results. For $V = 65.0$ μm/s, the theoretical values of λ_1 are far above the experimental values. This difference in λ_1 between

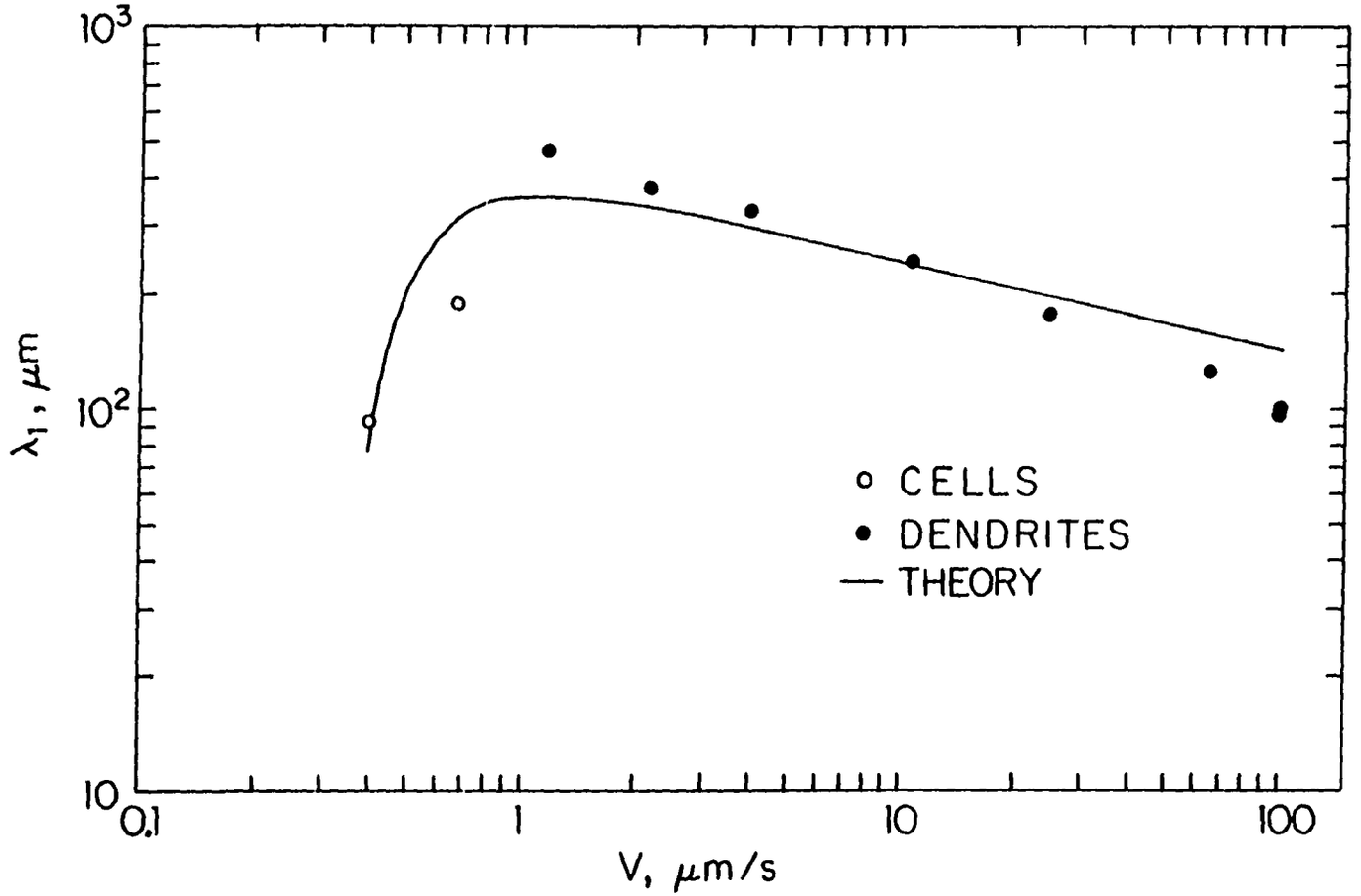

Figure IV.26. Comparison of the theory and experimental data on primary spacing in succinonitrile - 4 wt % acetone. G = 67 K/cm

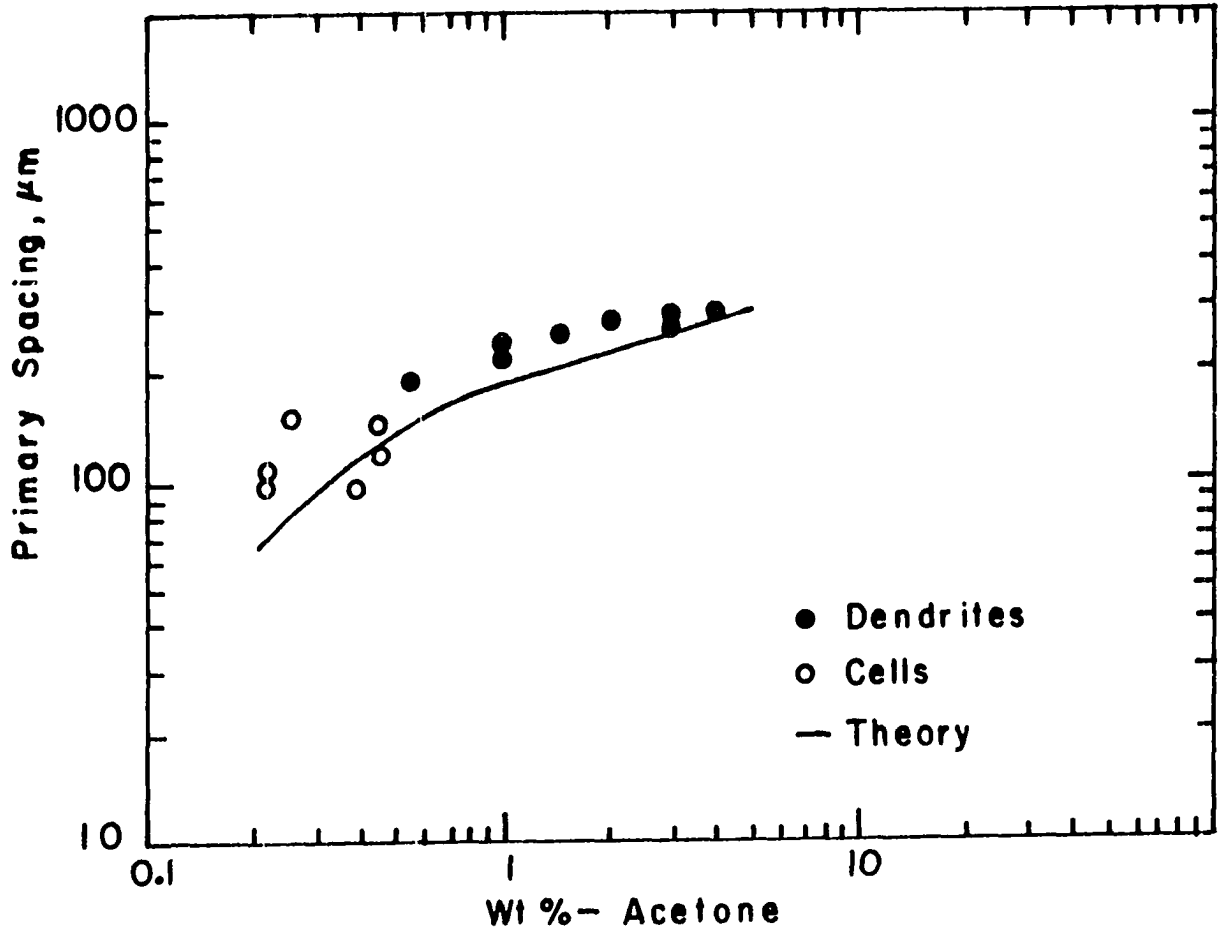

Figure IV.27. Variation in primary spacing with composition

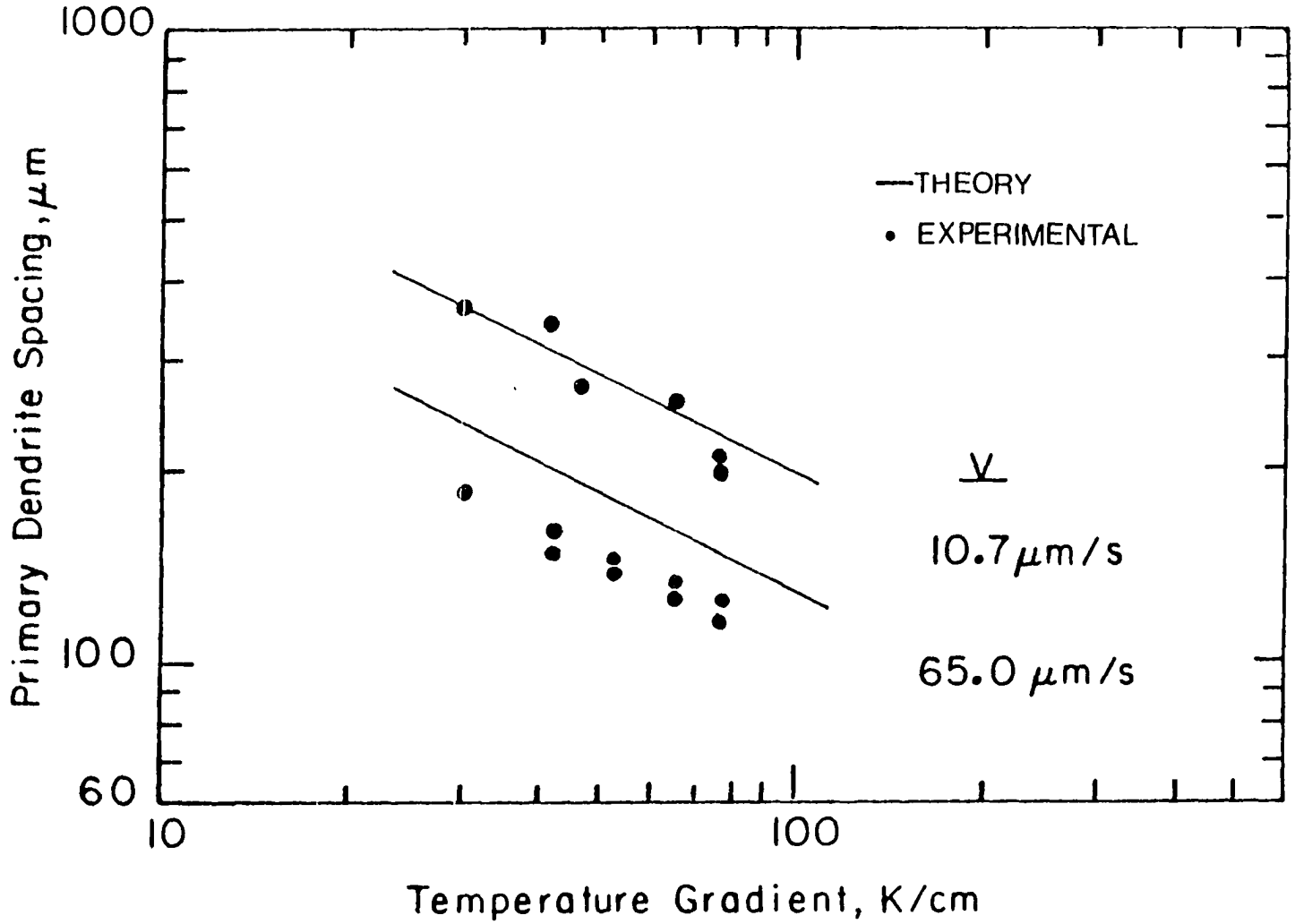

Figure IV.28. Comparison of theory and experimental data on λ_1 as a function of G at V = 10.7 μm/s and 65.0 μm/s

theory and experiment occurred because the agreement between the theory and experimental results at V > 10 μm/s is not good, as shown in Figure IV.26.

The temperature gradient significantly affects λ_1, although it has no effect on dendrite tip radius. In order to understand this observation, the results of dendritic growth at constant C_∞ and V for two values of temperature gradient are compared together. Figure IV.29 shows dendrite morphologies observed at G = 33 and 116 K/cm. These morphologies are superimposed in Figure IV.30 to show that the dendrite tip radii are identical in these two cases. However, the dendrite morphology obtained under the higher temperature gradient tends to be wider as we go further behind the tip. Thus, at any given location, the volume fraction of solid is greater for the higher temperature gradient condition. Consequently, the solute content in liquid at that location will be higher, which will cause λ_1 to decrease.

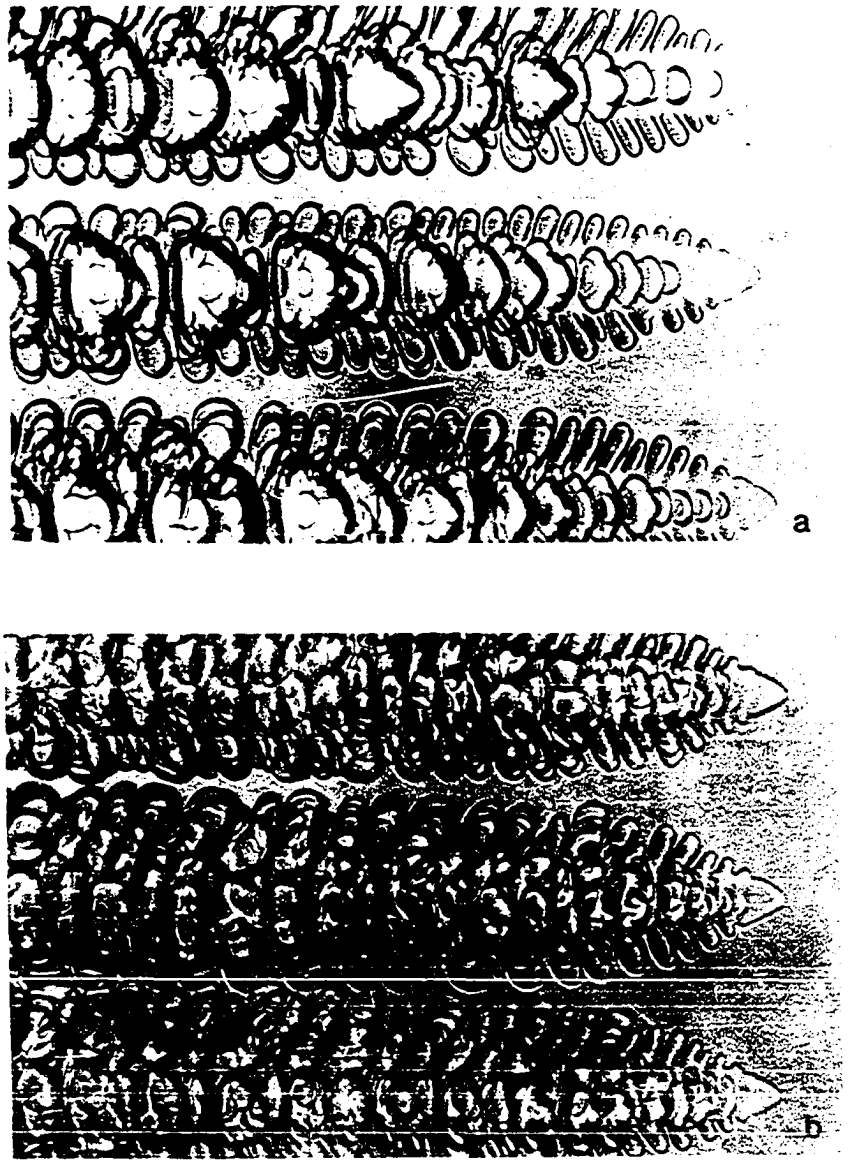

Figure IV.29. A comparison of dendrite morphologies obtained in directionally solidified succinonitrile - 4.0 wt % acetone solution, at V = 10.7 μm/s, under two thermal gradient conditions. (a) G = 3.3 K/mm; (b) G = 11.6 K/mm. Mag. 188X

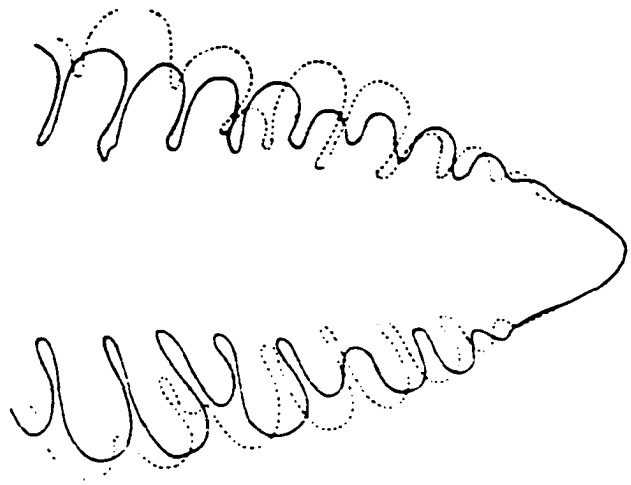

Figure IV.30. A superposition of the traces of dendritic morphologies of Figure IV.28. The solid shape corresponds to G = 33 K/cm, and the dotted shape is for G = 116 K/cm

V. TRANSIENT EFFECT DURING DENDRITIC GROWTH

A. Experimental Results

Directional solidification experiments were carried out in succinonitrile - 4 wt % acetone at G = 67 K/cm. Three sets of experiments were done in which the velocities were changed as follows: a) 1.17→1.5→1.17 μm/s, b) 1.17→5.8→1.17 μm/s and c) 1.17→10.7→1.17 μm/s. In each of these studies, the interface was allowed to come to its steady-state configuration before the change in velocity was imposed. Microscope pictures of the solid-liquid interface were taken during the steady-state and transient conditions, and the changes in dendrite tip radius, primary spacing and initial secondary spacing were measured from these micrographs. Table V.1 lists the steady-state values of λ_1, λ_2 and ρ for experiments used in this study.

Table V.1. Steady-state values of ρ, λ_2 and λ_1 at G = 67 K/cm for succinonitrile - 4 wt % acetone solution

V (μm/s)	ρ (μm)	λ_2 (μm)	λ_1 (μm)
1.17	23.0	47.5	472.0
1.5	19.8	41.5	448.0
5.8	8.6	16.9	286.0
10.7	6.2	14.2	240.5

Figure V.1 illustrates the changes in interface shape that occurred with time as the velocity was changed from 1.17 to 5.8 μm/s. Figure V.1(a) shows the initial steady-state configuration at 1.17 μm/s. The restabilization of the pattern with time is found to occur in two steps:

(1) The tip of each dendrite becomes sharper, Figure V.1(b), and the tip radius approaches the value that is characteristic of the steady-state growth conditions at 5.8 μm/s, as given in Table V.1. While the tip radius has already been reestablished to its new steady-state value, the primary spacing has not altered from its initial value.

(2) Since the primary spacing is smaller at V = 5.8 μm/s, it is necessary to create a dendrite to reduce the primary spacing. One of the tertiary branches (Figure V.1(c)) becomes the nucleus for the additional primary dendrite, and this nucleus subsequently develops into a primary dendrite, thereby reducing the average primary spacing, as shown in Figure V.1(d). This mechanism for primary dendrite creation was described earlier by Jackson *et al.* [67].

A significantly different restabilization mechanism is found to operate when the velocity is reduced from 5.8 to 1.17 μm/s. The time evolution of the steady-state interface profile is shown in Figure V.2. In this case, the tip radius increases initially (Figure V.2(b)) and then approaches infinity as the sidebranches near the tip grow somewhat rapidly toward the tip (Figure V.2(c)). The nearly flat region of the tip now becomes unstable (Figure V.2(d)), and splits into two or three protrusions. This split tip, along with the extended initial

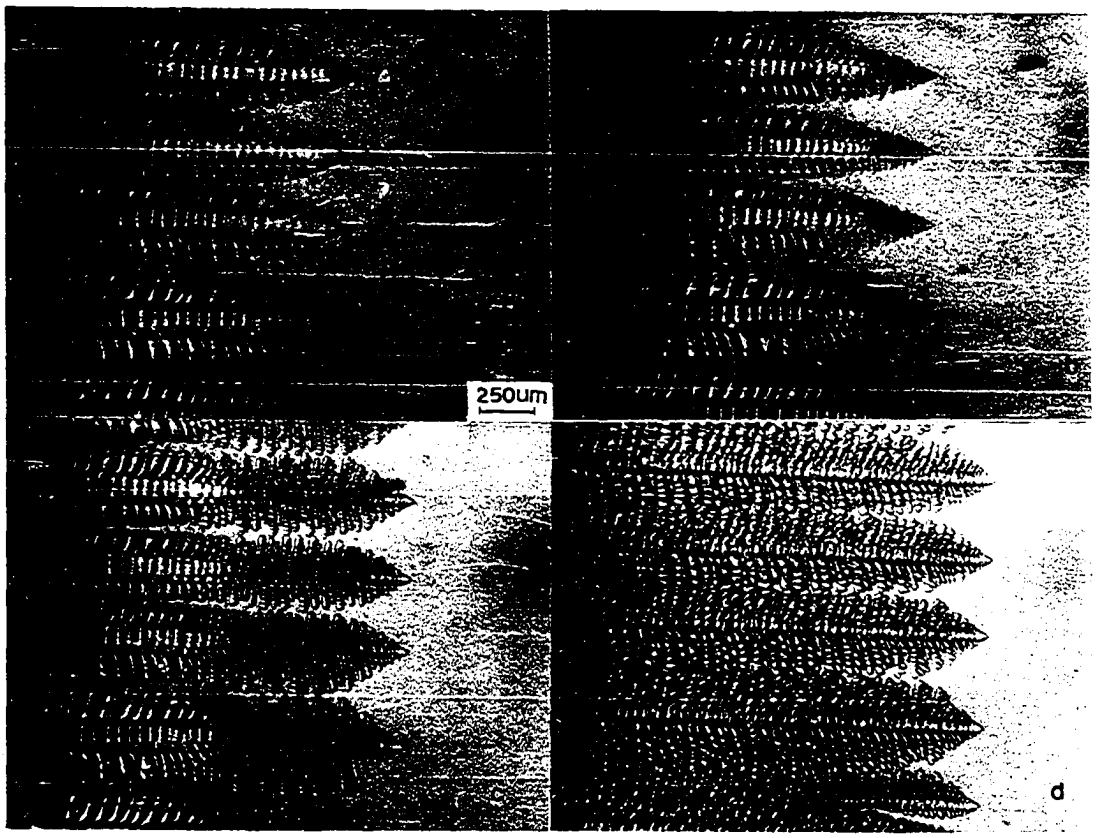

Figure V.1. Interface structures as a function of time when the applied velocity is suddenly changed from 1.17 to 5.8 μm/s during the directional solidification of succinonitrile-5.5 mol% acetone solution at G = 6.7 K/mm. (a) The initial steady-state interface structure at V = 1.17 μm/s, just before the applied velocity was changed to 5.8 μm/s, i.e. t' = 0, (b) t' = 60 s, (c) t' = 74 s, (d) t' = 674 s

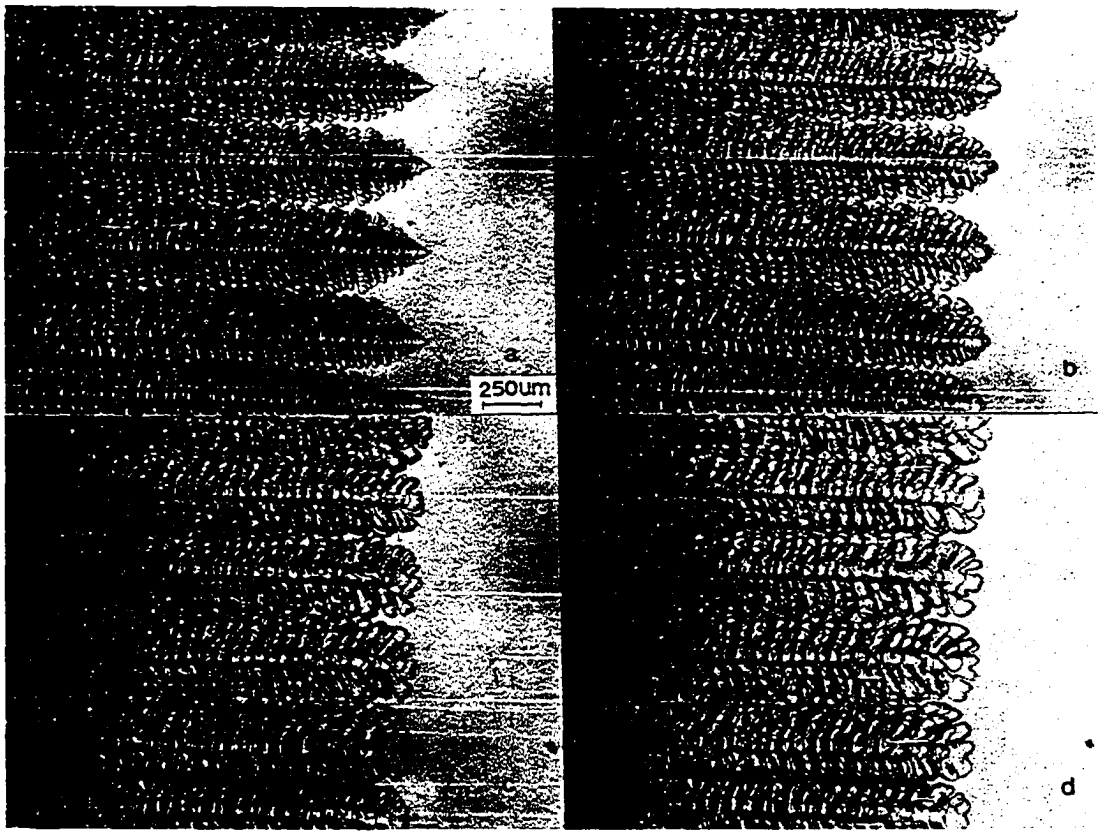

Figure V.2. Interface structures during the restabilization of steady-state conditions from the initial steady-state velocity of 5.8 μm/s to the final velocity of 1.17 μm/s. The times after the applied velocity was changed from 5.8 μm/s to 1.12 μm/s are (a) 0 s, (b) 120 s, (c) 660 s, (d) 840 s, (e) 1020 s, (f) 1200 s, (g) 1920 s, (h) 2820 s

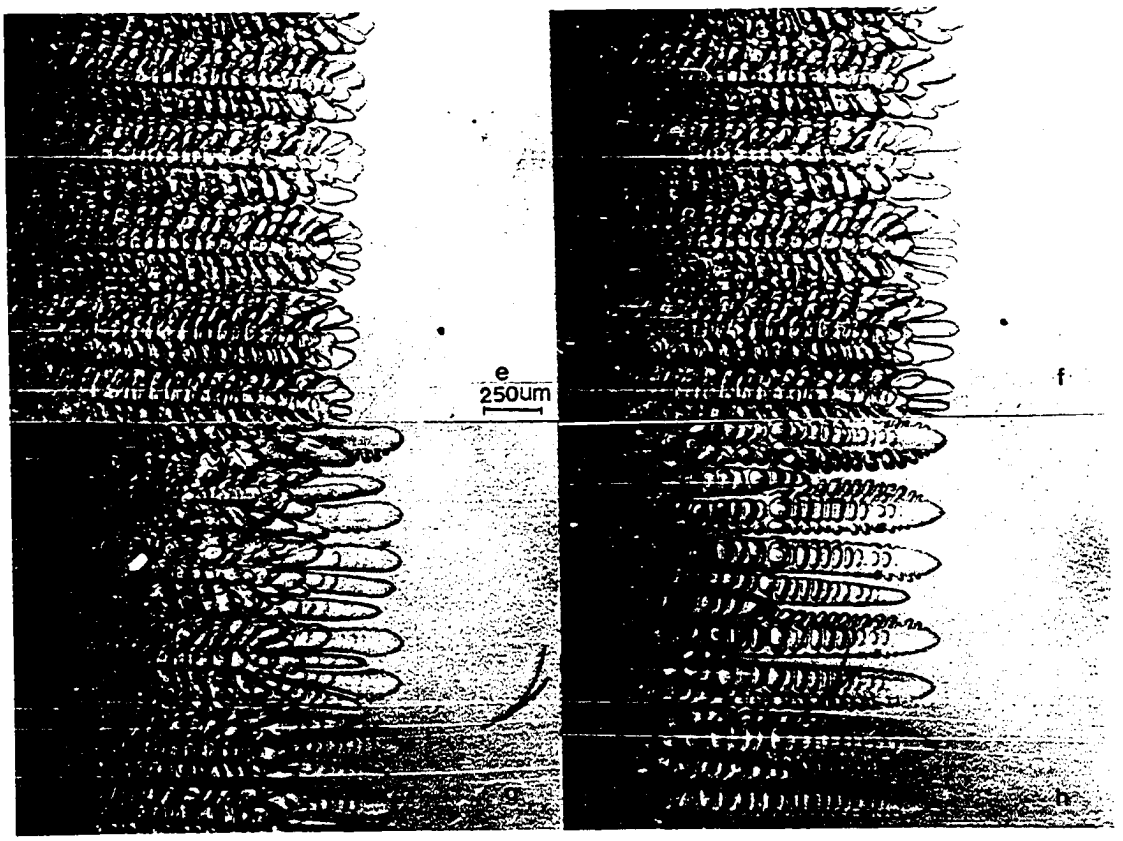

Figure V.2. Continued

sidebranches, forms a complex array of cellular structure, as seen in Figures V.2(e) and V.2(f). Next, a competition in growth among the cells occurs, and the ones which protrude further develop sidebranches (Figure V.2(g)). Finally, the primary spacing is adjusted by the elimination of some dendrites, as seen in Figure V.2(h). This sequence of events which restabilizes the interface is significantly different from that shown in Figure V.1.

Detailed measurements of dendrite tip radius (ρ), primary spacing (λ_1) and initial secondary arm spacing (λ_2) are also carried out to characterize the change in these parameters during the transient period when the interface is undergoing the restabilization process. These results are shown in Figure V.3 for the case in which the velocity was changed from 1.17→5.8→1.17 μm/s. A similar behavior was also exhibited by the other sets of experiments. Note, that instead of primary spacing, the actual locations of dendrite tips are shown in Figure V.3, so that any lateral movement of primary dendrites which may occur during the restabilizing process can be studied.

B. Discussion

1. The restabilization process

A significant difference in the process of restabilization of ρ, λ_1 and λ_2 is observed when the applied velocity is changed from 1.17 to 5.8 μm/s compared to the change from 5.8 to 1.17 μm/s. During the transient period, both ρ and λ_2 show a very similar behavior. In fact, the steady-state relationship reported earlier, $\lambda_2/\rho = 2.0$, appears to

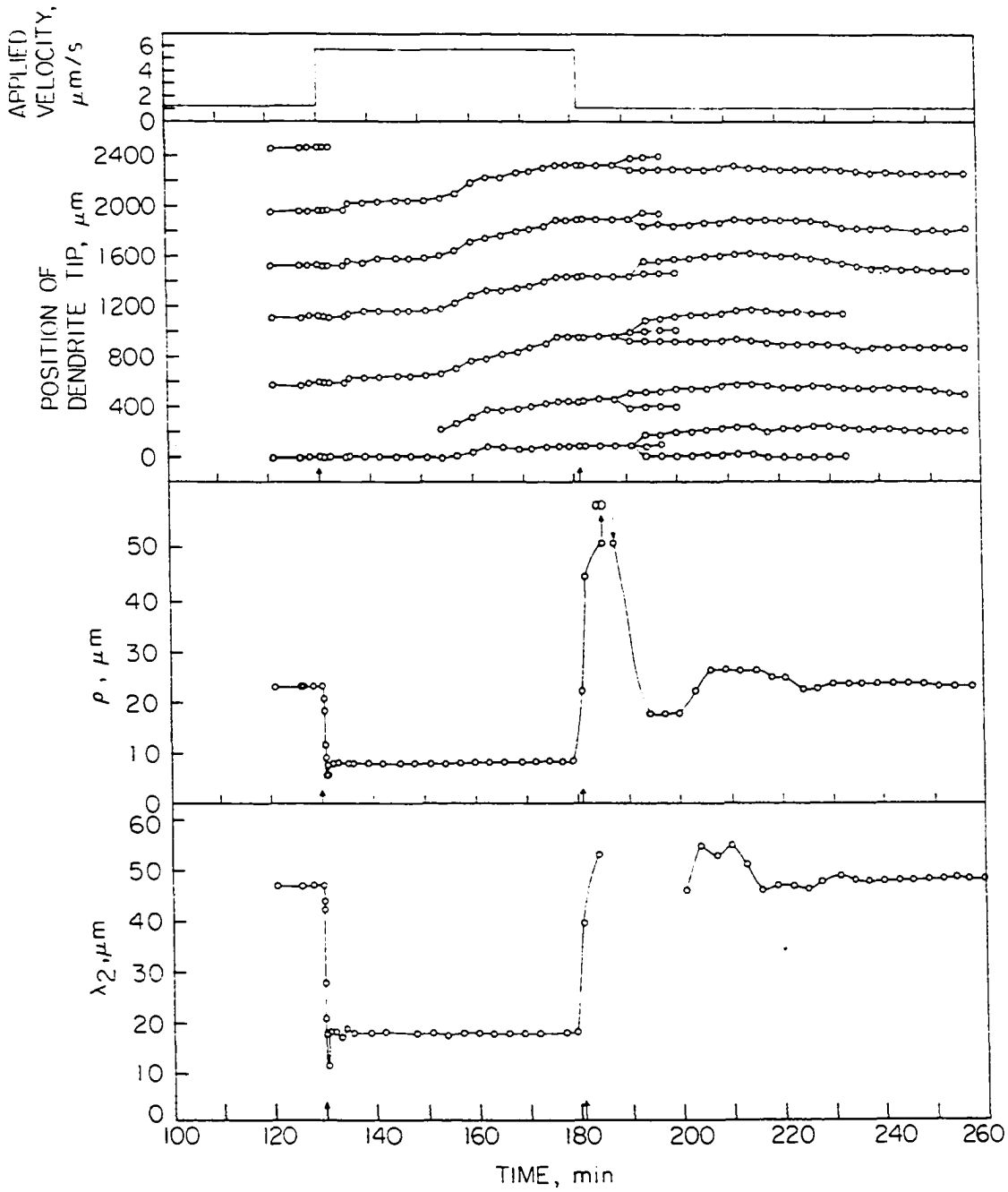

Figure V.3. The changes in dendrite tip positions, dendrite tip radius and initial secondary arm spacing as a function of time as the applied velocity was changed from 1.17 to 5.8 to 1.17 μm/s

hold closely, though not precisely, during the transient period.

Table V.1 shows that the steady-state values of λ_1, λ_2 and ρ should decrease as the velocity is changed from 1.17 to 5.8 μm/s. Figure V.3 shows that the dendrite tip radius begins to decrease as soon as the applied velocity is increased. The tip radius, as well as λ_2, initially overshoots the new steady-state value and then slowly approaches this value. The new steady-state values of ρ and λ_2 are established within about five minutes. However, during this time, there does not appear to be any significant change in the primary spacing. Figure V.3 shows that once ρ and λ_2 are restabilized, there is some lateral movement in the primary dendrite location. The top dendrite in Figure V.3 moves to the left (or upward in the figure) and goes out of the view of the microscope. The next four primary dendrite arms move laterally toward the left so that a slightly larger spacing occurs between the two lower dendrites in the figure. This fluctuation in primary spacing gives rise to longer sidebranches, and a tertiary arm begins to grow in the direction of the primary dendrite growth.

The creation of a primary dendrite from the tertiary branch is seen more clearly in Figure V.4 where the applied velocity was changed from 1.17 to 10.7 μm/s. In order to be effective as a source for primary dendrite, the tertiary branch should be located on a secondary branch which is significantly away from the dendrite tip. In fact, it appears that the tertiary branch becomes a primary dendrite when it is nearly at the center of the two adjacent primary dendrites. Figure V.4(b) shows how the tertiary branches of Figure V.4(a) have grown to become

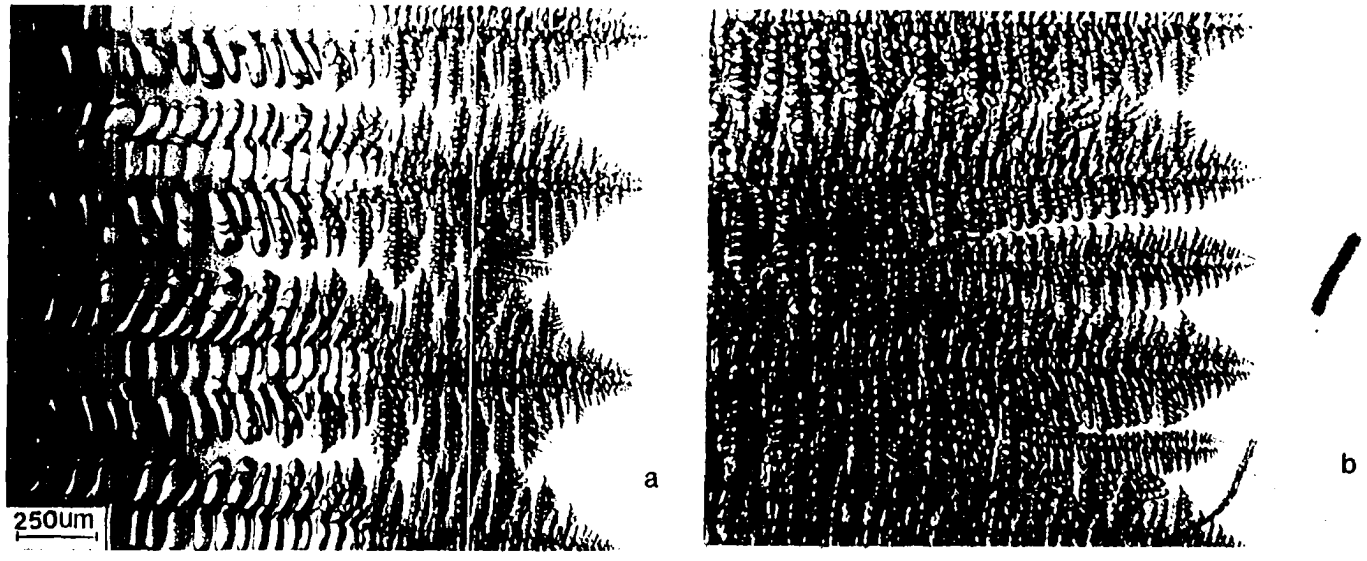

Figure V.4. The mechanism of creation of additional primary dendrites during the change in applied velocity from 1.17 to 10.70 μm/s. (a) After 480 s, tertiary arms are observed to nucleate new primary dendrite arms, (b) after 1200 s, two tertiary arms have become primary dendrites

primary dendrites. Once the tertiary arm begins to grow, there is a lateral movement of other primary arms to accommodate this additional dendrite, as seen in Figure V.3. The formation of additional dendrite and the readjustment of primary spacing takes a considerably longer time than that required for the restabilization of dendrite tip radius or of secondary arm spacing.

The restabilization process is considerably slower when the applied velocity is changed from 5.8 to 1.17 μm/s. In this case, λ_1, λ_2 and ρ will all increase. Figure V.3 shows that the increase in ρ and λ_2 occurs immediately after the applied velocity is increased, whereas λ_1 remains unaltered for some time. In fact, the value of λ_1 does not simply decrease by the elimination (through a slower growth rate) of some of the primary dendrites. As the applied velocity is reduced, the dendrite tips become larger. However, instead of stabilizing the radius value when it approaches the characteristic value of the steady-state growth at V = 1.17 μm/s, the radius increases to infinity. This flattening of dendrite tip occurs due to the interaction of sidebranches with the thermal and diffusion fields at the tip. The nature of this interaction will now be examined.

During the steady-state dendrite growth, the location at which the first sidebranch's perturbation forms is related to the dendrite tip radius. As shown in Figures IV.21 - IV.23, the relationship of λ_p and ρ is found to depend on the value of the temperature gradient, alloy composition and growth velocity. This relationship λ_p/ρ is seen to be one of the steady-state characteristics of dendritic growth. For the

condition used in this experiment, i.e. G = 67 K/cm and C_∞ = 4 wt %, it is found that λ_p/ρ is a weak function of velocity and the value of $\lambda_p/\rho \simeq 4.2 \pm 0.4$ is observed as $1 < V < 10$ μm/s. During the initial steady-state growth at 5.8 μm/s, the initial sidebranches are already present at $\lambda_p = 4.2\rho$. Now, as the velocity is reduced, the dendrite tip radius increases so that the steady-state λ_p will also increase. However, sidebranches are already present near the tip at a location which is much closer to the tip than what the new conditions would require. These existing sidebranches then grow faster than the tip so that the first couple of sidebranches tend to grow toward the primary growth direction. As these sidebranches grow, the solute rejected from these sidebranches causes the tip region to become nearly flat since the tip can no longer reject the solute effectively in the lateral direction. This planar tip, however, is unstable under given growth conditions, so that it will split. The split tip and the first couple of sidebranches then form a complex array of cellular structure. The subsequent evolution to the dendritic structure then occurs through the competition in growth as described in the next part. Once a dendritic array is formed, a finer adjustment in primary spacing occurs through the elimination of one or more dendrites, as seen in Figure V.2(h).

The influence of sidebranches on the adjustment of dendrite tip radius to a larger value can be seen more clearly in Figure V.5. In this figure, the same sequence of events is illustrated for the case in which the applied velocity is changed from 1.50 to 1.17 μm/s. The

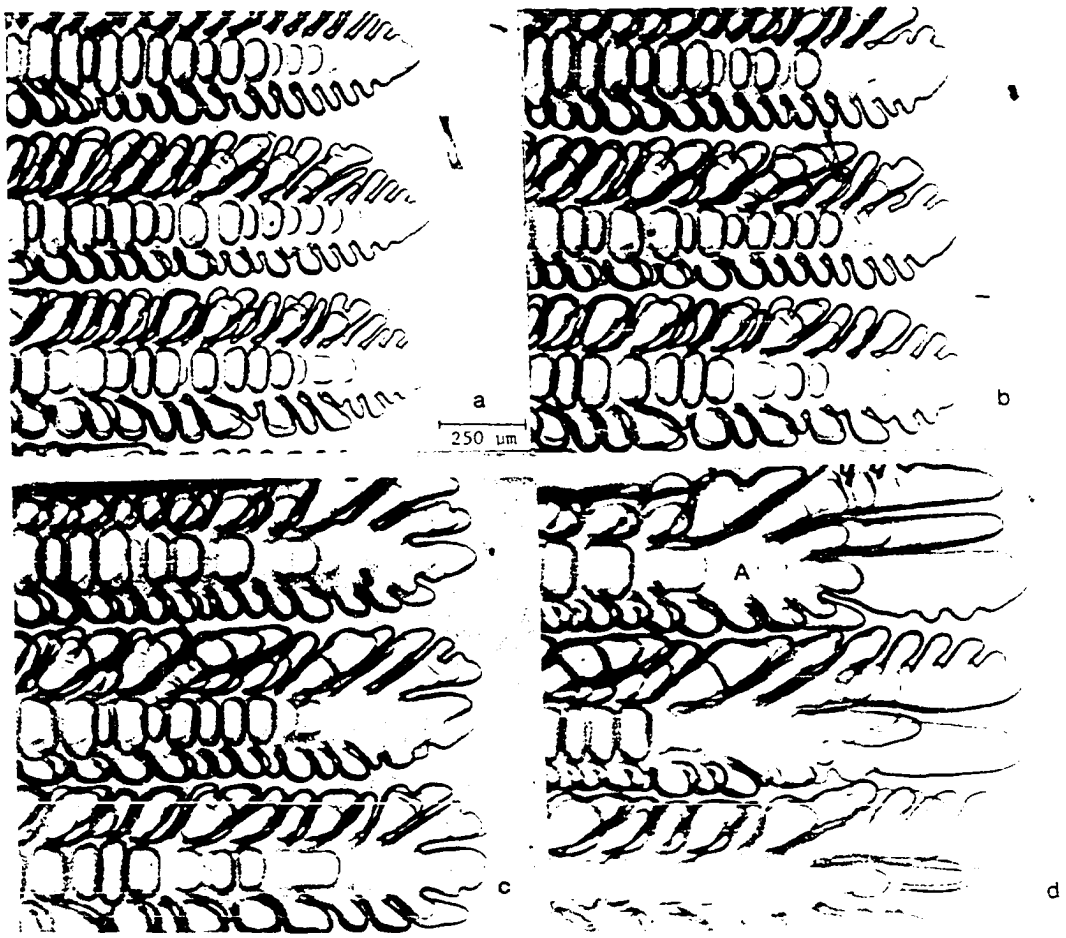

Figure V.5. Interface patterns formed after the steady-state structure solidified at 1.50 μm/s were suddenly altered by changing the applied velocity to 1.17 μm/s. The times after the change in applied velocity are (a) 0 s, (b) 335 s, (c) 782 s, (d) 1365 s

region marked A clearly shows how the sidebranches interact with the tip and how they become a part of the complex array in the direction of primary dendrite growth. Note that in this case, the change in velocity is quite small. Nevertheless, the restabilization process is quite similar to the one shown in Figure V.2 for the larger velocity difference.

2. The hysteresis effect

The hysteresis effect in the restabilization of steady-state interface shapes is quite evident from Figures V.1 - V.3. The dendrite tip radius value always approaches the value which is just marginally stable. The path that dendrite tip radius takes as it goes from its initial value to the final restabilized value will next be examined.

During the steady-state condition at v = 1.17 μm/s, the interface velocity is precisely the same as the applied velocity. However, as the applied velocity is suddenly changed to 5.8 μm/s, the interface velocity does not change rapidly. Rather, it changes over a finite time period which shall be referred to as the restabilization time, τ. From the series of photographs taken with time, the velocity of the interface is determined, and the results are shown in Figure V.6. The change in dendrite tip radius with time is also plotted on an expanded scale to see if any correlation exists between the interface velocity and dendrite tip radius during the transient period. The interface velocity increases rapidly as the applied velocity is changed from 1.17 to 5.8 μm/s. The interface velocity overshoots significantly, then decreases rapidly, and finally, approaches the applied velocity slowly. From this experimental condition, the restabilization time is

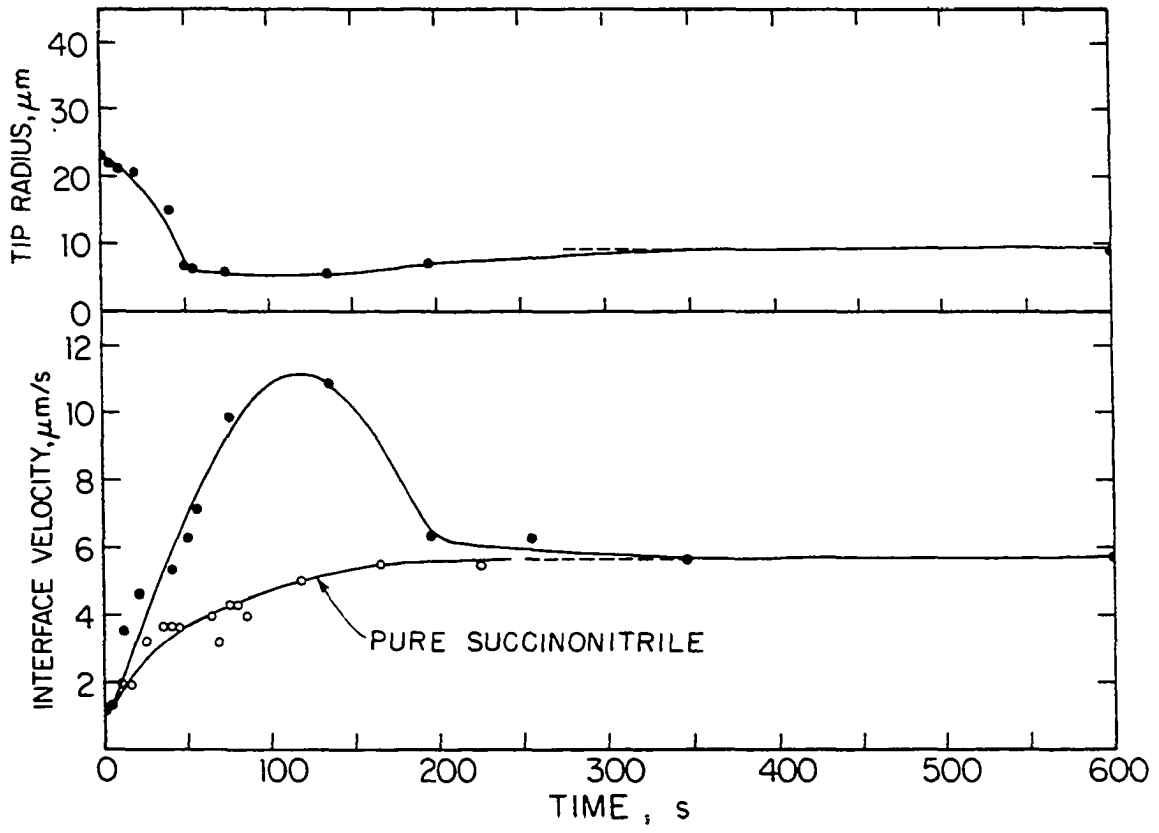

Figure V.6. The variation of dendrite tip radius and the interface velocity as a function of time after the applied velocity was changed from 1.17 to 5.8 μm/s

approximately 343 seconds.

At this point, one might conclude that the overshooting in the interface velocity, as shown by the solid dot in Figure V.6, may occur because of the solute diffusion around the dendrite tip.

However, thermal diffusion may also play an important role during the restabilization process. In order to be sure that only the solute diffusion mechanism is participating in this transient period, another set of experiments was carried out in pure succinonitrile in which the external imposed velocity was changed from 1.2→5.6→1.2 μm/s. For pure succinonitrile grown under positive temperature gradient, the solid-liquid interface is planar and the thermal diffusion is the only mechanism that occurs during the transient period. The changes in the interface velocity were measured with time and superimposed in the Figure V.6. It shows that the interface velocity measured under the growth of pure succinonitrile does not overshoot the final velocity. The restabilization time in this case is about 160 seconds, which is slightly less than that observed in alloy growth. Thus, it may be concluded that the overshoot of interface velocity that occurs during the transient period is due only to the solute diffusion effect.

The change in dendrite tip radius correlates extremely well with the change in interface velocity. As the interface velocity increases, the radius value decreases. Also, the radius value overshoots when the interface velocity overshoots the steady-state value. Finally, the dendrite tip radius approaches the steady-state value when the interface velocity coincides with the applied velocity. Although there

is an excellent correlation between the interface velocity and the dendrite tip radius, no such correlation exists between the interface velocity and the restabilization of the primary spacing. In fact, the primary spacing begins to alter only after the interface velocity becomes equal to the applied velocity.

Figure V.7 shows the variation in interface velocity with time for the reverse sequence in which the applied velocity is changed from 5.8 to 1.17 μm/s. The changes in the interface velocity in the case of pure succinonitrile are also shown on the same figure. The basic features are quite similar to those shown in Figure V.6. The major difference, however, is that the tip radius overshoots to infinity and then splits. No such sharp change in interface velocity is seen at the time when tip splitting occurs. The restabilization time, τ, in this case, is about 4000 sec, which is over an order of magnitude larger than that observed in Figure V.6. However, the restabilization time of interface velocity during the planar interface growth is nearly the same, τ = 150 seconds.

The results of Figures V.6 and V.7 are plotted in Figure V.8 to examine the evolution of pattern in the V-ρ space, where V is the interface velocity. The dotted line is the theoretical correlation between the steady-state velocity and tip radius for the marginal stability criterion. The experimental data for the steady-state conditions match accurately with the theoretical prediction. The solid line shows the path taken in the ρ-V space during the transient period in which the interface velocity adjusts from 1.17 to 5.8 μm/s and from 5.8 to 1.17 μm/s. A significant hysteresis effect is observed.

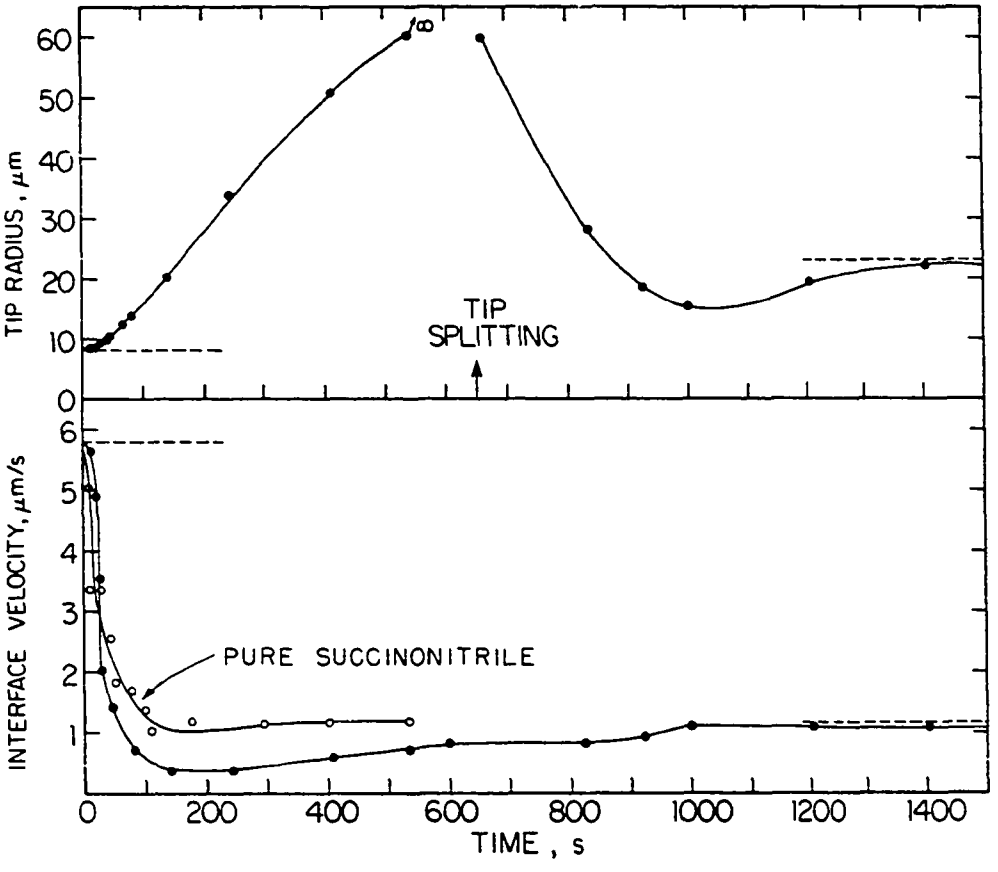

Figure V.7. The variation of dendrite tip radius and the interface velocity as a function of time after the applied velocity was changed from 5.8 to 1.17 μm/s

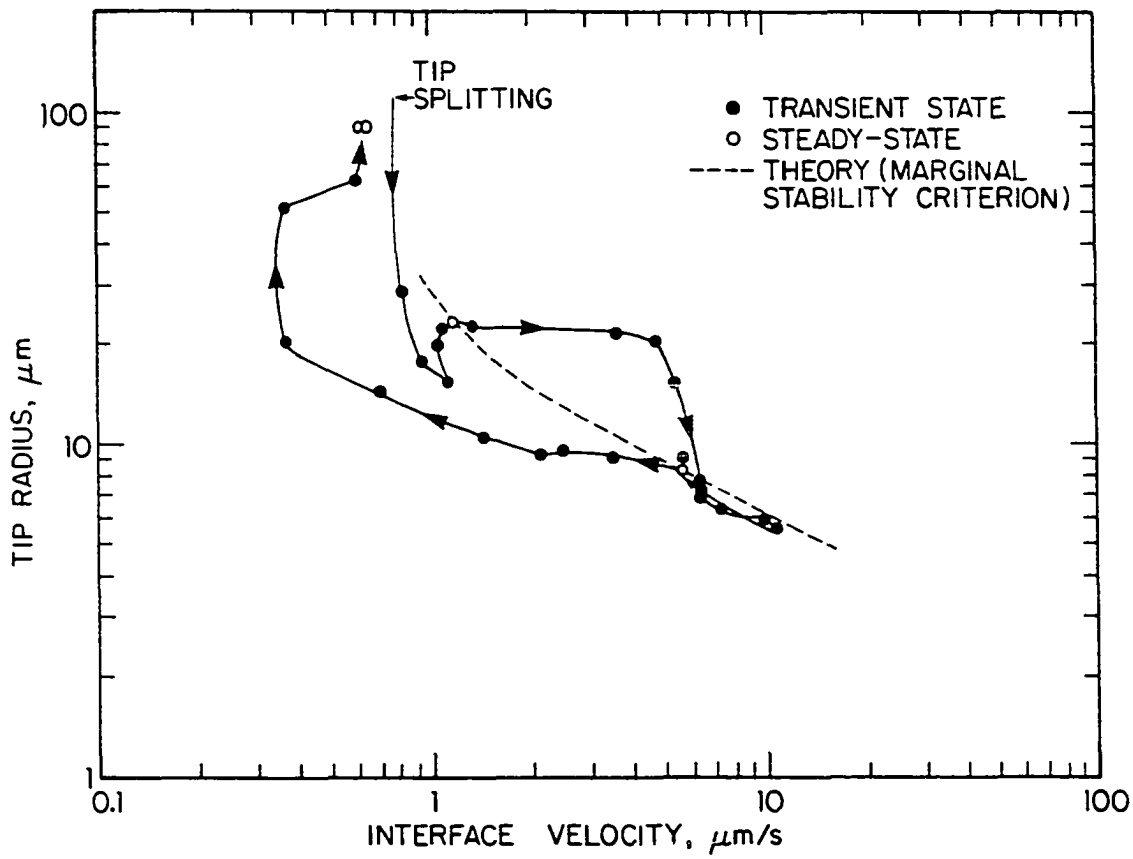

Figure V.8. The correlation between the interface velocity and tip radius during the restabilization of steady-states when the applied velocity was changed from 1.17 to 5.8 to 1.17 μm/s. Experimental steady-state values and the theoretical steady-state values based on the marginal stability criterion are also shown for comparison

For 1.17 to 5.8 μm/s transition, the interface velocity changes somewhat sharply in the beginning, whereas the tip radius changes somewhat slowly. When the interface velocity approaches 5.8 μm/s, a sharp change in tip radius occurs. The overshoot in velocity and radius is clearly seen and finally, the interface velocity approaches the applied velocity and the tip radius approaches the value which is just marginally stable. A somewhat similar observation is made when the applied velocity is changed from 5.8 to 1.17 μm/s. In this case, one again sees, initially, a somewhat rapid decrease in interface velocity and somewhat slower increase in dendrite tip radius. The interface velocity, in this case, overshoots below 1.17 μm/s before a sharp increase in tip radius is observed. The tip radius then splits, and the dendritic pattern which emerges from the complex cellular pattern then approaches the applied velocity, although the tip radius is somewhat smaller. Finally, when the interface velocity coincides with the applied velocity, the dendrite tip radius equals the value which is just marginally stable.

The results presented in Figure V.8 are also exhibited by other sets of experiments in which the velocity sequence was 1.17→1.5→1.17 μm/s and 1.17→10.7→1.17. In all these cases, the restabilized dendrite tip radius always corresponds to the values which are just marginally stable under given experimental conditions. From the viewpoint of the stability analysis, any dendrite configuration which lies above the dotted line in Figure V.8 is unstable with respect to the tip splitting phenomenon. However, these experimental results show clearly that no

tip splitting is observed when the velocity is changed from 1.17 to 5.8 μm/s. This possibly could be due to the fact that the solid line in Figure V.8 shows transient conditions, whereas the stability analysis is based on small deviations from a steady-state configuration. It is also quite likely that any small anisotropy effect present at the tip would make the tip stable with respect to the splitting behavior. We also observe that if the tip radius suddenly becomes larger, the sidebranch activities will cause the pattern to become unstable and the pattern will then restabilize through a complex sequence of events until the marginally stable radius is established.

A similar hysteresis phenomena was observed earlier by Verhoeven and Gibson [68] for a slightly different situation. They studied dendrite to eutectic transition and found that the fraction of dendrites decreases with the decrease in growth rate near the dendrite-eutectic transition region. They observed that if the applied velocity is increased or decreased continuously, the fraction of dendrites present as a function of applied velocity exhibit a hysteresis effect. This observation can be understood in light of the present investigation since the change in primary spacing is found to occur much more slowly than the change in applied velocity.

3. The effect of ΔV

In order to study the effect of the velocity difference on the restabilization phenomena, three sets of experiments were carried out with $\Delta V = 0.33$, 4.63 and 8.83, where ΔV is the magnitude of the

difference between the final and the initial velocity. The basic mechanisms for the restabilization process were found to be the same for all three cases studied. The only difference among these cases was the magnitude of the restabilization time, τ. Table V.2 lists the magnitudes of τ as a function of initial and final velocities. These results are also shown in Figure V.9 for comparison. As ΔV is increased, τ is found to decrease, i.e. the restabilization time is shorter for large differences in velocities. For the same magnitude of ΔV, the value of τ is an order of magnitude larger when the growth rate is decreased, compared to the case in which the growth rate is increased.

In experiments carried out to obtain single crystals of alloys, there are always possibilities of fluctuations in velocities due to the mechanical drive system or due to temperature fluctuations. These experimental results show that even a small fluctuation in velocity

Table V.2. Correlation of τ with V

Applied velocity condition (μm/s)	Restabilization time (seconds)
1.17 → 1.50	1358
1.17 → 5.80	343
1.17 → 10.7	140
1.50 → 1.17	10150
5.80 → 1.17	4000
10.70 → 1.17	2800

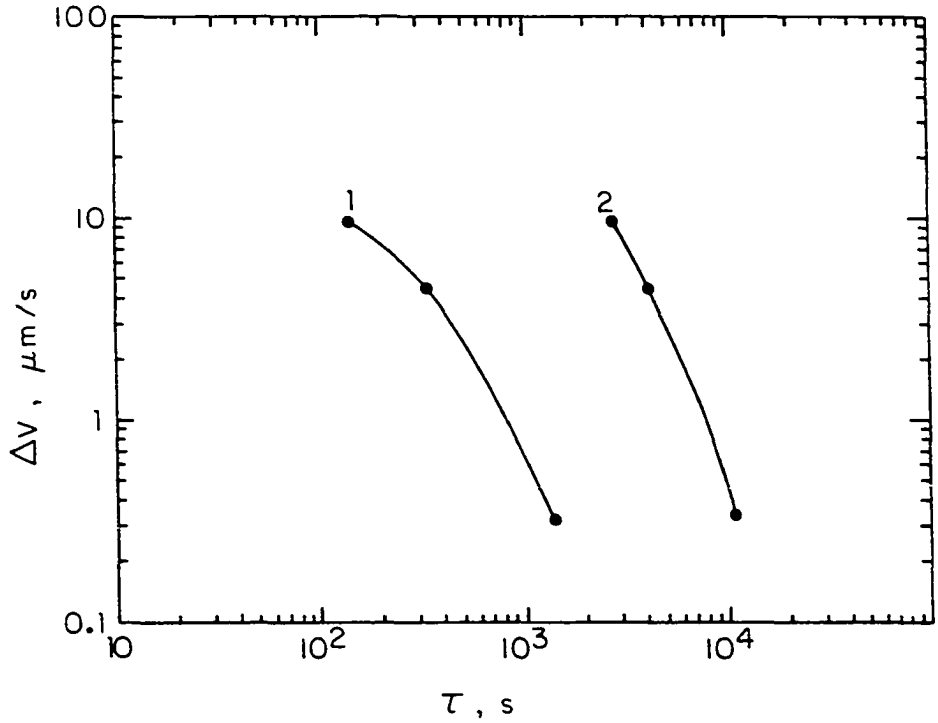

Figure V.9. The dependence of the restabilization time, τ, on the magnitude, ΔV, of the difference between the initial and the final velocities. Curve 1 represents the increase in velocity from 1.17 μm/s and curve 2 is for the decrease in velocity to the final velocity of 1.17 μm/s

will cause a change in microstructure. As the velocity increases and decreases, the microstructure will tend to go through the sequences presented in Figures V.1 and V.2. However, the time taken to cause the change in primary spacing or to observe tip splitting is considerably large. Consequently, any fluctuations in velocity with a small periodicity will only show a small fluctuation in tip radius. What is critical is a fluctuation which may be small in ΔV, but has an extremely large periodicity. Such a fluctuation would cause considerable deviation in microstructure from the required steady-state microstructure.

VI. INSTABILITY OF A PLANAR INTERFACE

A. Results and Discussion

1. Initial breakup of a planar interface

The experimental studies on initial breakup of planar interface were carried out in succinonitrile - 4 wt % acetone solution and the temperature gradient at the interface was maintained at 67 K/cm. At this condition, the critical velocity at which the instability of planar interface occurs can be approximated by using the constitutional supercooling criterion from Equation (1) combined with the physical properties of succinonitrile-acetone system in Appendix A. The result gives V_{cr} = 0.078 μm/s. Consequently, experiments were carried out in which a planar interface was first obtained at V = 0.06 μm/s. Next, the applied velocity was increased to a velocity at which the planar interface becomes unstable. In these studies, velocities were varied from 0.34 to 6.3 μm/s, and the initial wave number (frequency) of the interface was measured from the micrographs for each velocity run.

A series of pictures showing the initial perturbations developed on the planar interface as a function of growth velocities is shown in Figure VI.1. At low velocity regions, a few perturbations develop on the interface. The distribution of these perturbations is not uniform, but somewhat localized, as shown in Figure VI.1(a) and VI.1(b). At high velocity regions, the perturbations occur somewhat uniformly. The average wavelength of the smallest periodicity, λ_i, was measured as a function of growth velocity and is summarized in Table VI.1.

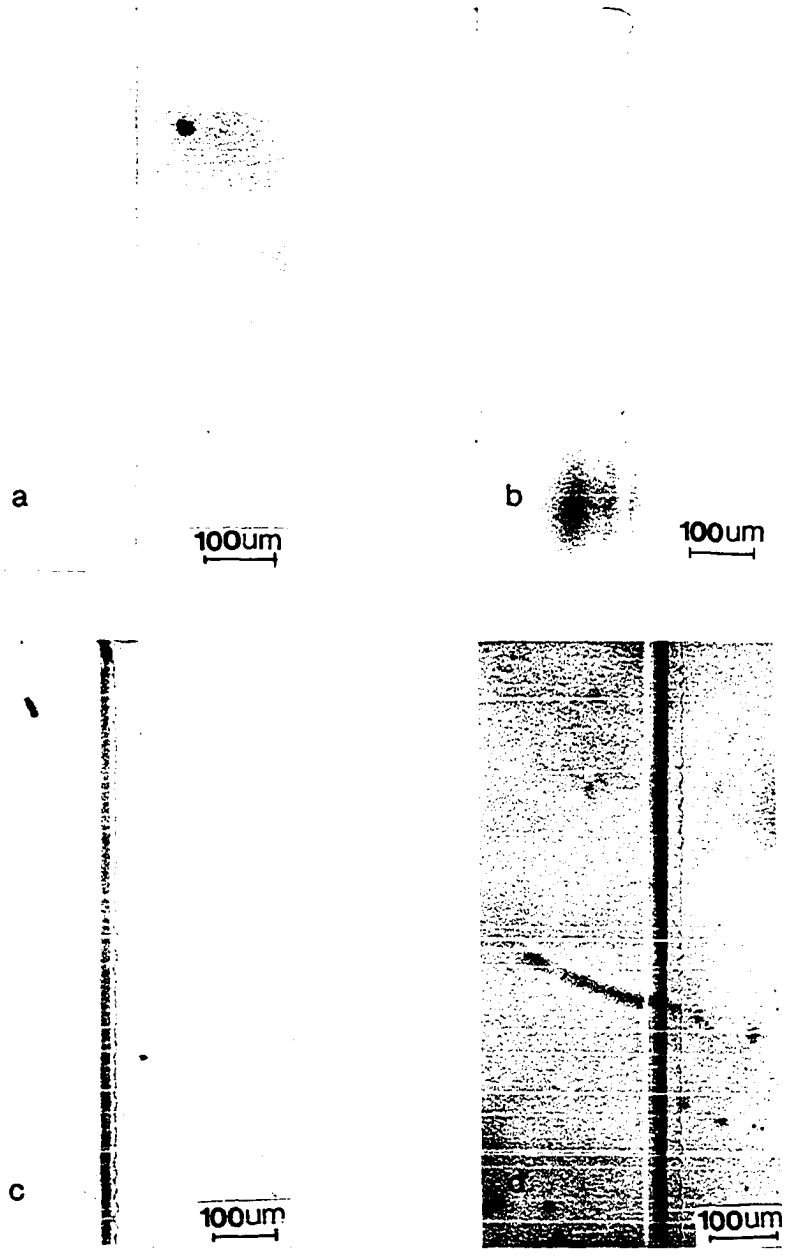

Figure VI.1. Initial perturbations of a planar interface as a function of velocity in succinonitrile - 4 wt % acetone at G = 67 K/cm. a) V = 0.4 μm/s, b) V = 0.83 μm/s, c) V = 2.4 μm/s, d) V = 5.2 μm/s

Table VI.1. Experimental data of initial wavelength as a function of velocity in succinonitrile - 4 wt % acetone at G = 67 K/cm

V (μm/s)	λ_i (μm)	w_i (μm^{-1})
0.34	102.5	0.061
0.4	73.6, 80.0	0.087, 0.079
0.68	71.3, 62.65	0.10, 0.088
0.83	54.52	0.115
1.17	41.7, 47.4	0.15, 0.133
2.46	31.9, 27.7, 26.4	0.197, 0.226, 0.465
3.4	30.0	0.21
5.2	23.0, 25.5, 26.8	0.27, 0.25, 0.23
6.3	20.6, 21.0	0.31, 0.3

Figure VI.2 shows the plots of λ_i as a function of V. The values of the final steady-state spacing, λ_1, are also shown for comparison. In the dendritic region, λ_1 and λ_i are nearly parallel, whereas λ_1 is reduced significantly in the cellular region. Figure VI.3 shows the variation of λ_1/λ_i as a function of V. It clearly shows that the pattern formation process in dendritic region is significantly different from the process in cellular region. The variation of λ_2/λ_i is also shown in Figure VI.3. It shows that the scaling law between λ_2 and λ_i is obtained, i.e. $\lambda_2/\lambda_i \simeq 1.0$, within the range of V studied.

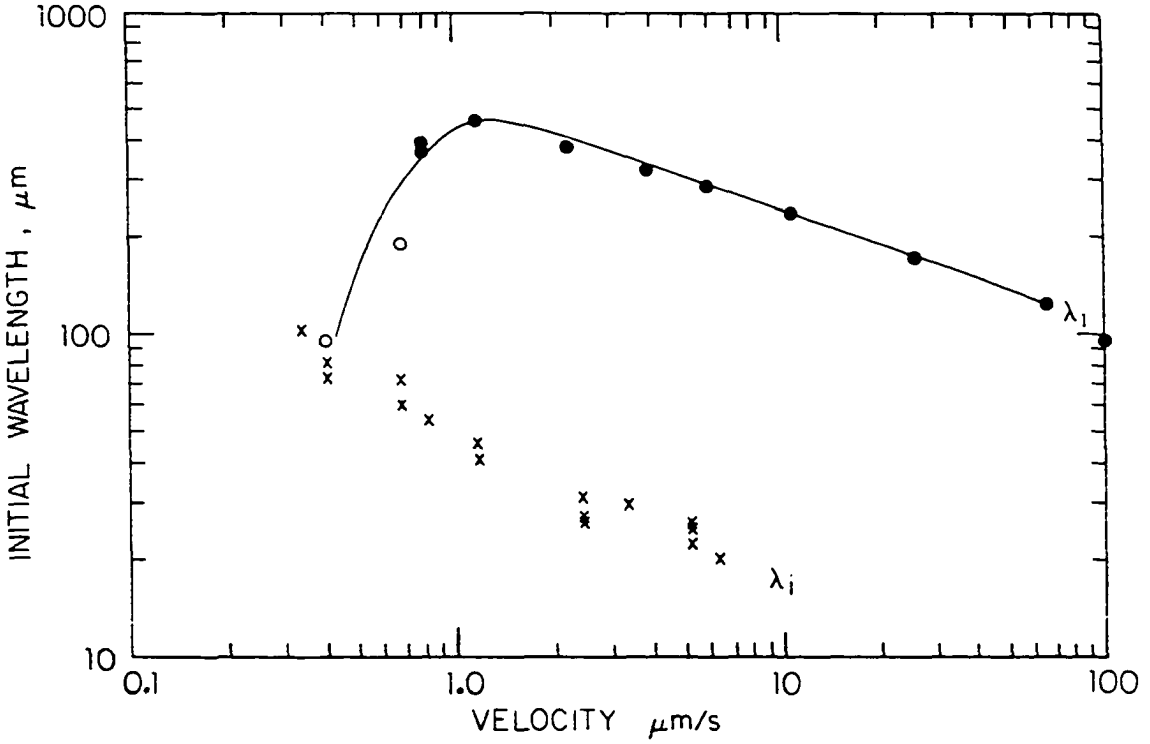

Figure VI.2. Variation of λ_i and λ_1 with V in succinonitrile - 4 wt % acetone at G = 67 K/cm

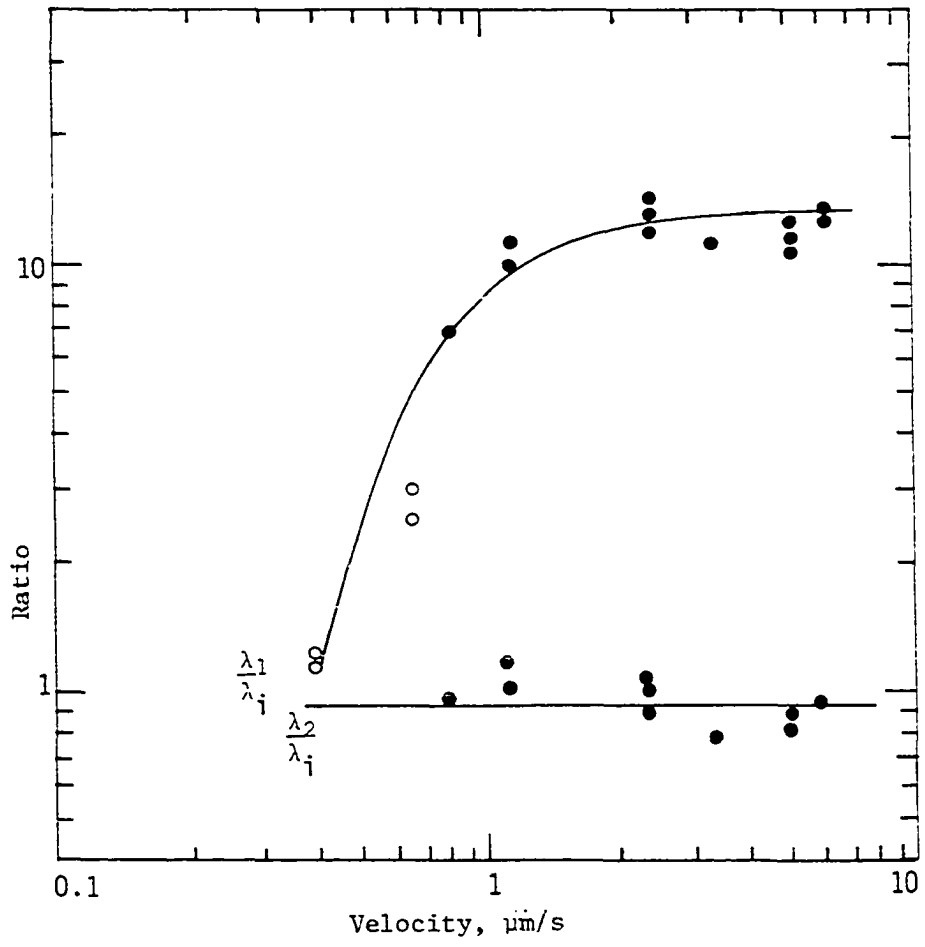

Figure VI.3. Variation of λ_1/λ_i and λ_2/λ_i with V in succinonitrile - 4 wt % acetone at G = 67 K/cm

2. Pattern formation

The experimental results on the instability of a planar interface, which have been discussed above, showed that the pattern formation process could be separated into two regimes: (1) $V > V_{cr}/k$, where dendritic structures form and (2) $V_{cr} < V < V_{cr}/k$, where cellular structures form. Within each regime, the pattern evolution process was found to be the same, whereas the manner in which patterns propagated varied significantly in these two regimes.

Figure VI.4 illustrates the time evolution of the interface pattern in the first regime where $V > V_{cr}/k$. The initial instability occurs somewhat uniformly with a wave number, w_f, (or wavelength, λ_f), as seen in Figure VI.4. The initial instability soon propagates into the undisturbed region such that the interface pattern which emerges has a larger wave number, w_i, (or smaller wavelength, λ_i). As the interface pattern is fractalized, the amplitude of the disturbance corresponding to the wave number w_f is slightly higher than the amplitude of the perturbations which form subsequently (see Figure VI.4(b)). A further propagation of the pattern occurs such that the initial perturbations with wave number w_f keep outgrowing the rest of the perturbations. When the amplitude of the leading perturbation becomes much larger than the amplitudes of the perturbations in its neighborhood, the leading perturbation becomes parabolic at the front and sidebranches begin to form. Once perturbations become dendrites with sidebranches, the growth of the rest of the perturbation is reduced significantly. This dendritic front then increases in its amplitude until it propagates with

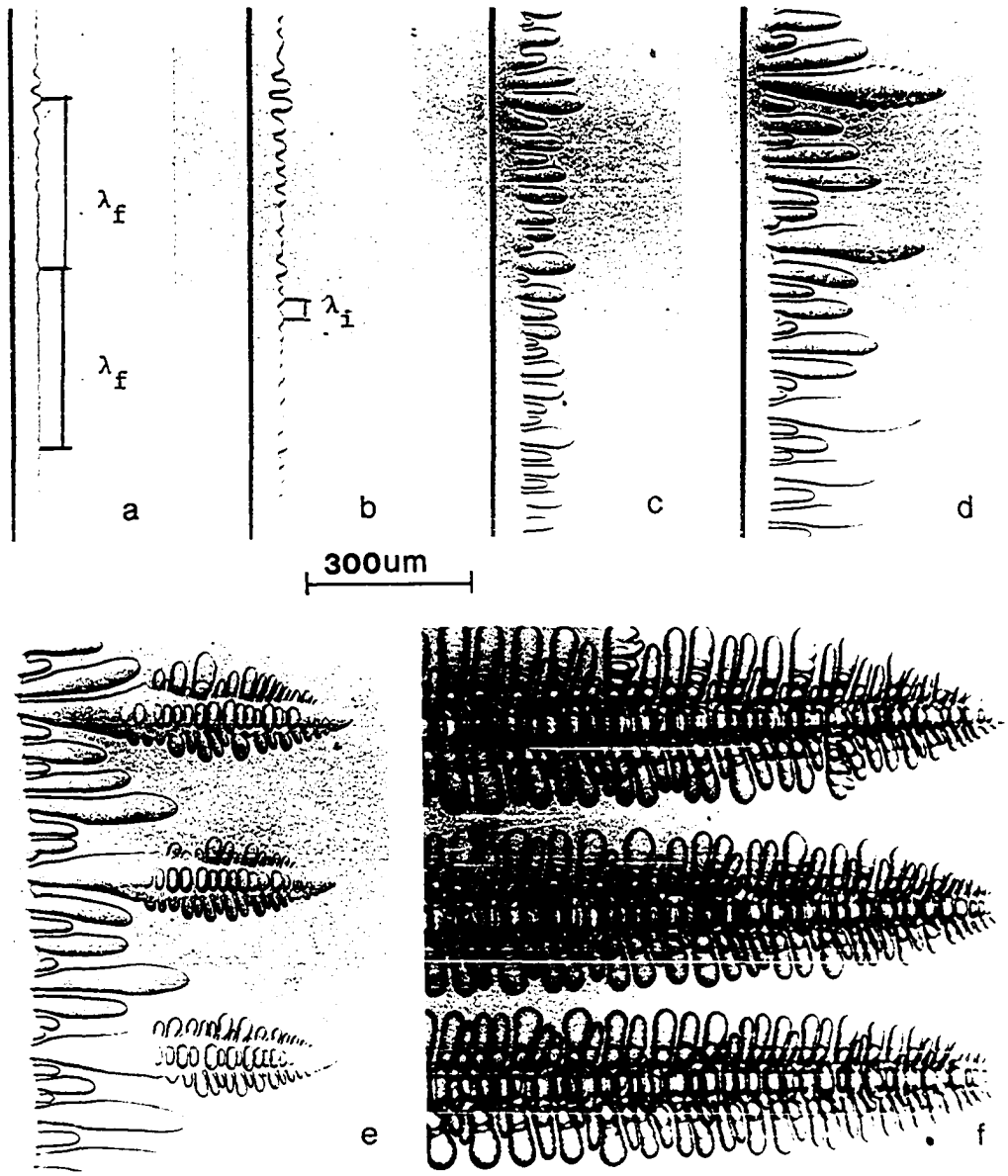

Figure VI.4. Development of solid-liquid interface shapes with change in growth rate from 0.06 to 3.4 μm/s at a temperature gradient of 67 K/cm. (a) 50 s, (b) 55 s, (c) 65 s, (d) 80 s, (e) 135 s, (f) 740 s

a velocity that is equal to the externally imposed velocity. The wave number, w_1, of this final steady-state pattern, shown in Figure VI.4(f), is nearly identical with the wave number, w_f. In some cases, where one of the initial perturbations forms on a grain boundary, some slight lateral movement of that dendrite occurs with time to obtain a uniform primary spacing.

The formation and the propagation of the pattern, when $V_{cr} < V < V_{cr}/k$, is shown in Figure VI.5. In this case, the initial perturbation of the profile is not periodic, but is somewhat localized. As shown in Figure VI.5(a), two perturbations of nearly the same amplitude are observed next to each other with a distance of λ_i between them. As this pattern propagates, additional perturbation is observed at a distance of λ_f away from the first perturbated region. Soon the undisturbed region between these two perturbed regions begins to become unstable with a characteristic spacing which is close to λ_i. Note that the initial perturbation does not propagate faster. In fact, the tip radius of the initial two perturbations increases with time, and the distance between them is also increased slightly. Furthermore, the amplification of the initial perturbation is reduced until the rest of the perturbations catch up with them. Thus, in contrast to the case of dendrite formation, the initial perturbations in this case propagate laterally until a stable pattern is formed whose wave number is characteristic of the cellular structure under given experimental conditions.

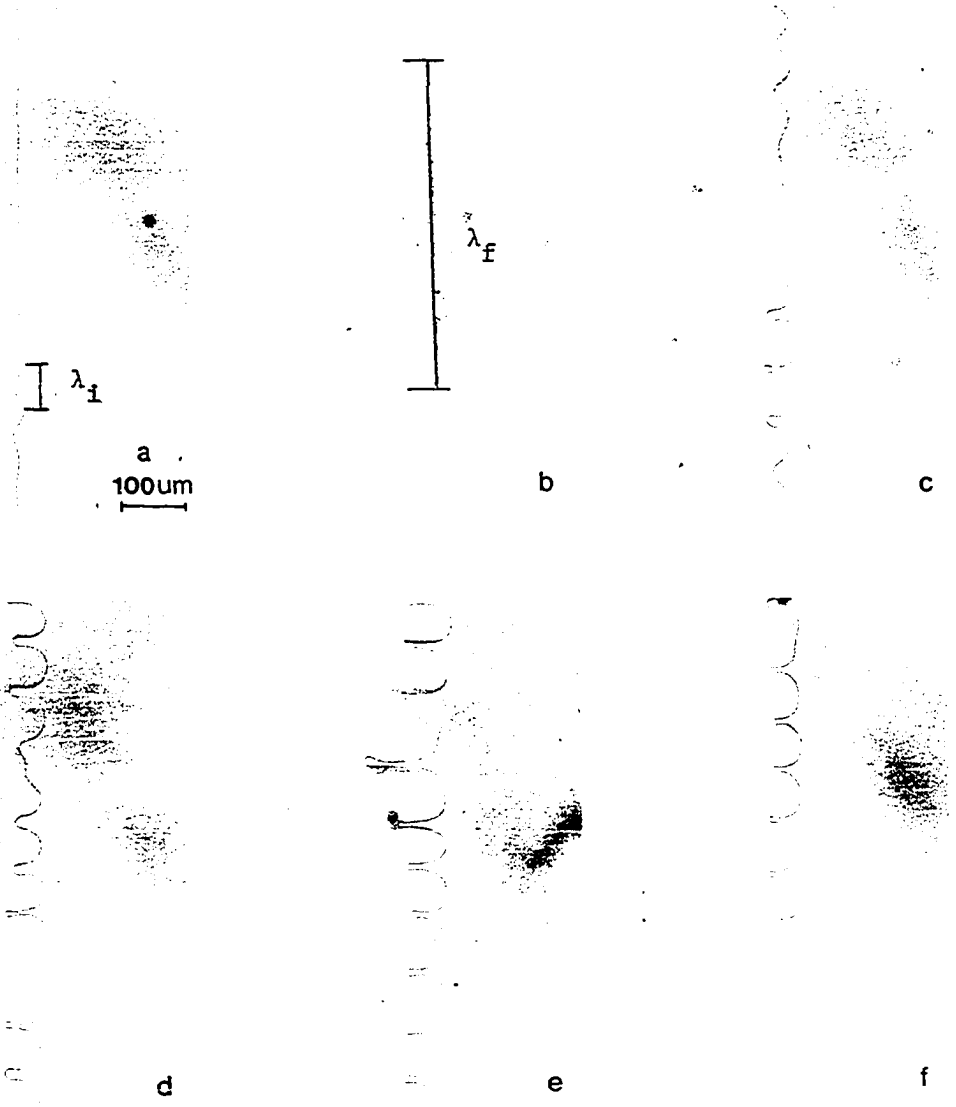

Figure VI.5. Development of solid-liquid interface shapes with change in growth rate from 0.06 μm/s to 0.4 μm/s at G = 67 K/cm. (a) 102 min, (b) 152 min, (c) 167 min, (d) 177 min, (e) 197 min, (f) 287 min

B. Comparison with the Theory

A theoretical model for the pattern propagations is not yet available to compare our results quantitatively. Consequently, the linear stability analysis of Mullins and Sekerka [10] which has been discussed earlier is compared with our results. Figure VI.6 shows the plot of the amplification rate $\frac{\delta^{\cdot}}{\delta}$ for infinitesimal sinusoidal deformation with the wave frequency, w, at different velocities and G = 67 K/cm, C_{∞} = 4 wt % acetone. The curves go through maximum at w_{max} and become positive for a range of frequencies corresponding to an unstable interface. The experimental results of the smallest wavelength, λ_i, are plotted to compare with the theory. Since the final steady-state wavelength λ_1 is always larger than the smallest wavelength, λ_i (or $w_i > w_1$), in all dendritic and cellular regions, the initial, as well as the final, wave frequencies are found to be significantly smaller than those corresponding to the maximum of $\frac{\delta^{\cdot}}{\delta}$. The experimental results for $V > V_{Cr}/k$ show that perturbations with initial wave frequency, w_f, grow faster than the subsequent perturbations with wave frequency, w_i. However, these faster growing perturbations do not correspond to the maximum in $\frac{\delta^{\cdot}}{\delta}$, as predicted by the theory. It thus appears that nonlinear effects are very important in selecting the amplification rate.

For clear understanding, the allowable unstable wave frequencies as a function of velocity can be best examined by v-w diagram, shown schematically in Figure VI.7. The outer curve is the locus of points for which $\frac{\delta^{\cdot}}{\delta}$ vanishes and it represents the neutral stability of the

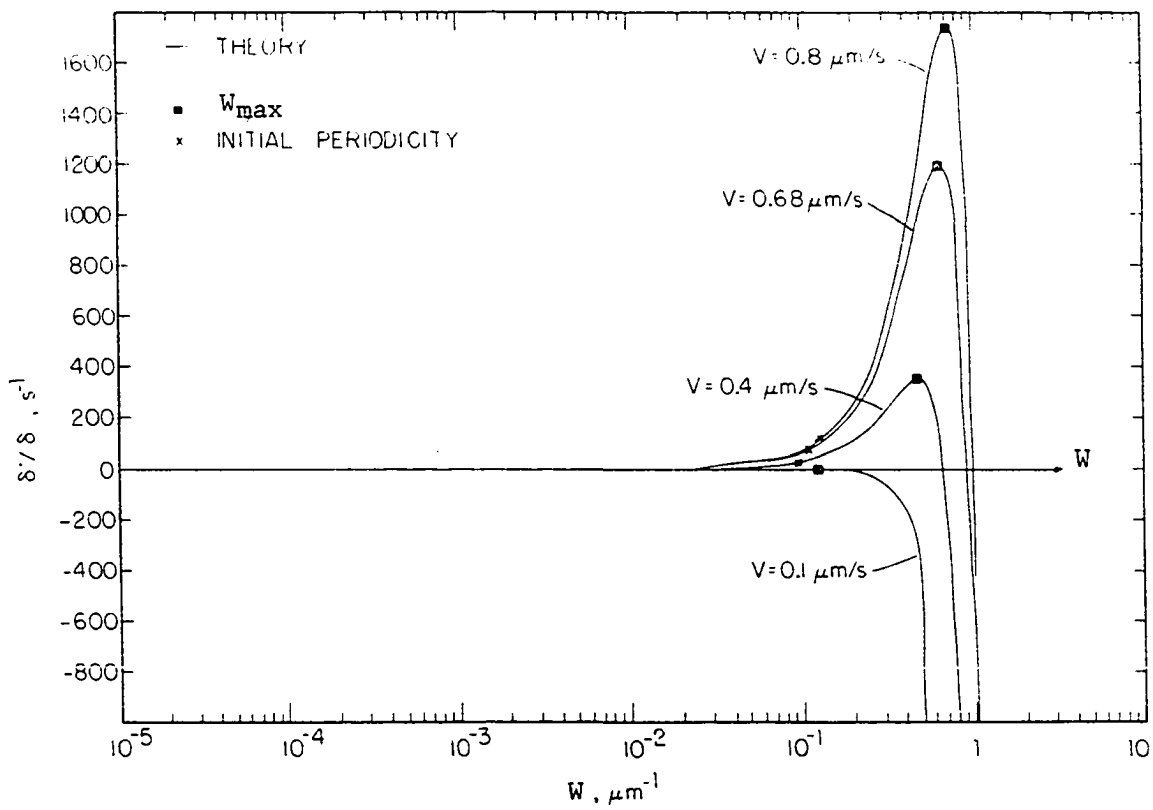

Figure VI.6. Variation of $\dot{\delta}/\delta$ with wave frequency at three different velocities in succinonitrile - 4 wt % acetone at G = 67 K/cm

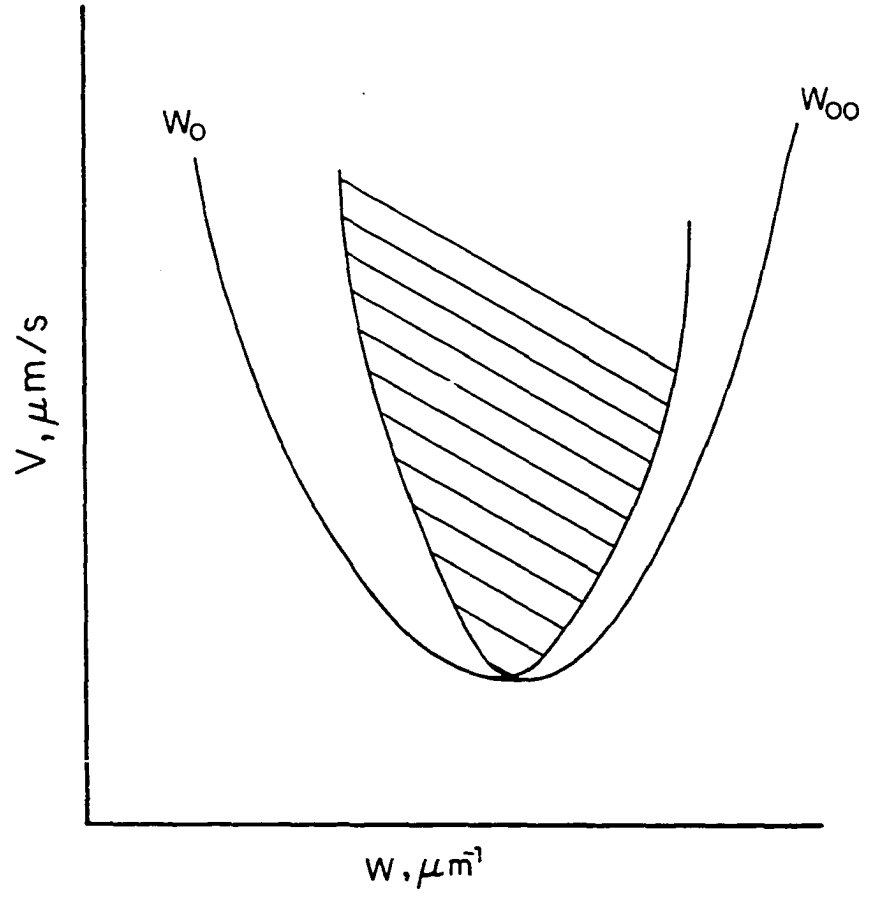

Figure VI.7. Schematic plot of V vs. w showing the regions of stable stationary states (inside the solid curve) and the neutral stability curve (the outer curve)

planar front. Although a planar interface is unstable with respect to a finite band of wave frequencies (w_o, w_{oo}), Dee and Mathur [7] have recently shown that only a subset of these wave frequencies is stable. This is shown schematically in Figure VI.7 where the inner curve gives the region of (v, w) values for which stable, stationary cellular state exists. Experimental studies on the steady-state growth show that for a given velocity, the system evolves into a specific state with a unique wave frequency in that a unique primary spacing is observed for a given value of $V > V_{cr}$. It is thus desirable to see if the experimental results presented in this part lie within the inner envelope or not.

Figure VI.8 shows the v-w diagram of succinonitrile - 4 wt % acetone at G = 67 K/cm. The experimental studies show that the largest and the smallest wave frequencies are w_i and w_l, respectively. This range of unstable wave frequencies is shown in Figure VI.8. Unfortunately, the results of Dee and Mathur [7] are numerically evaluated so that they cannot be qualitatively plotted for the conditions of this experiment. However, it is quite clear that only a small subset of (w_o, w_{oo}) is observed experimentally. These observed ranges of wave frequencies are clearly much smaller than the w_{max} value which corresponds to the highest amplification rate predicted by the linear stability analysis.

The values of w_l and w_i at v = 0.4 μm/s are very close to each other, i.e. w_i/w_l is 1.3. It would be desirable to see the behavior of w_l and w_i near the critical velocity value. Unfortunately, for the composition and temperature gradient values used in this study, V_{cr} is about 0.078 μm/s. Near such a low velocity, the interface pattern is

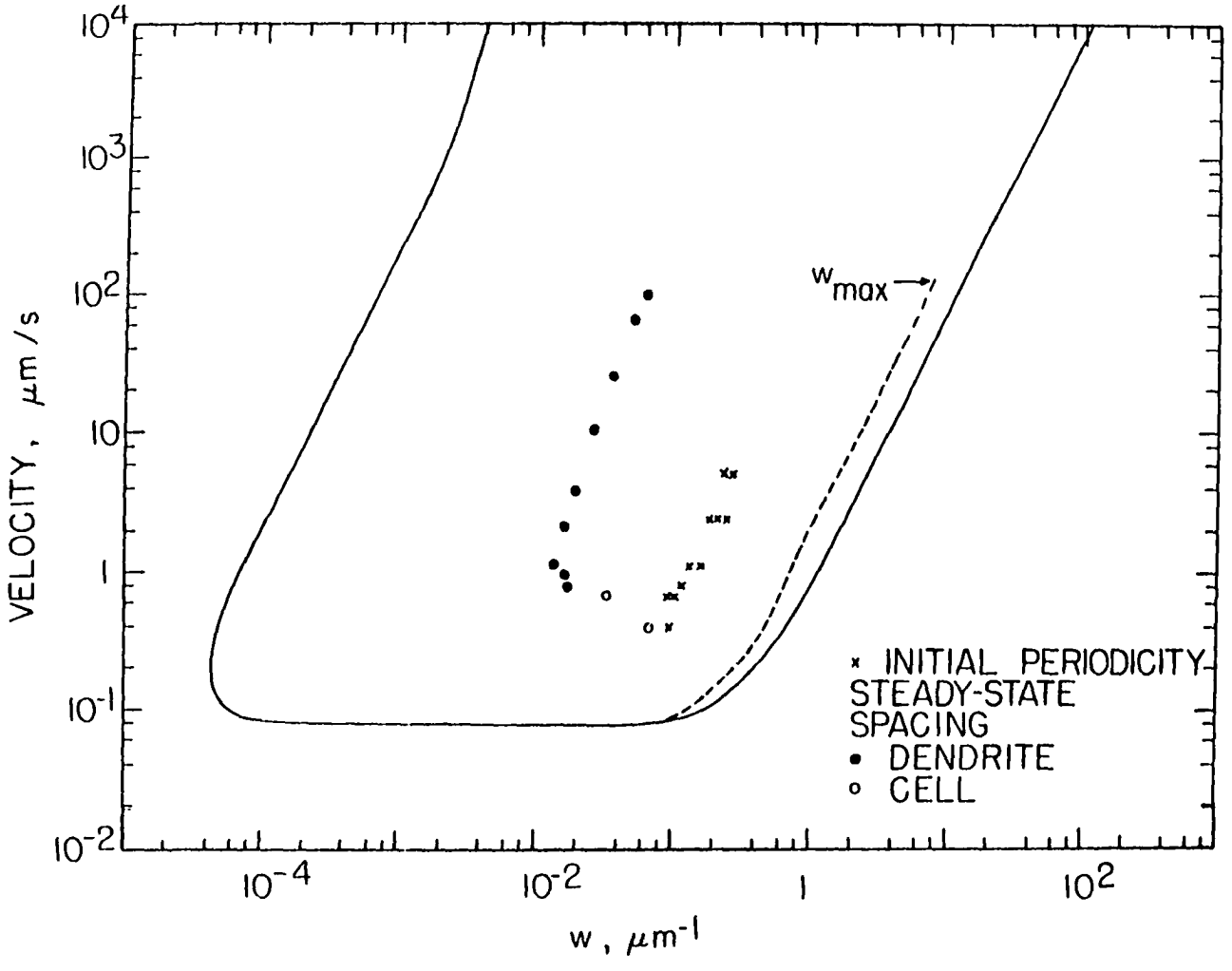

Figure VI.8. The plot of V vs. w for succinonitrile - 4 wt % acetone at G = 67 K/cm

significantly influenced by vibrations and convection effects. In these experiments for $V \geq 0.4$ μm/s, no convection effects were found to be present. This was checked by the procedure described in Part III.

VII. DYNAMICAL STUDIES

One of the transient effects that is important during the dendritic growth process is the time-dependent coarsening of the secondary branches. Also, another transient effect is the occurrence of tertiary branches on the secondary arms. In this part, these two important transient effects which occur during the dendrite growth process will be investigated and compared with the other experimental results.

A. Secondary Arm Coarsening

1. The measurement of secondary arm spacing

Since the secondary branch coarsening is a time-dependent phenomenon, one generally relates local secondary branch spacing with the solidification time, t_f. Strictly speaking, one should carry out the time that is elapsed after the formation of first sidebranch perturbation so that the coarsening time would be $(X - X_p)/V$, where X is the distance behind the dendrite tip and $X_p = \lambda_p$. However, since $X >> X_p$, the local solidification time would give a reasonable result. The measurement of λ_2 in metallic alloys is often made either after a complete solidification or after quenching the alloy. All of the secondary arm spacings which appear in the micrograph are measured and plotted as a function of solidification time. Another criterion for measuring $\lambda_2(t)$ was given by Huang and Glicksman [25] on dendrites grown in pure undercooled succinonitrile melt. They measured only the active branches of the secondary arms. The sidebranches which are larger than the neighboring ones are called "active branches". Their

results, when compared to the results from metallic system, give higher slope of the relationship between $\lambda_2(t)$ and t_f,

In this research, the criterion of Huang and Glicksman [25] on the measurement of $\lambda_2(t)$ is used. This criterion is illustrated in Figure VII.1. Figure VII.1(a) shows an array of dendrites in succinonitrile - 4 wt % acetone, directionally solidified at G = 67 K/cm and V = 1.17 μm/s. It is evident that the sidebranches are longer and the spacings between the branches are larger as we go further behind the dendrite tip. The variation of the length of sidebranches, as measured from the sidebranch to the middle of the primary arm, as a function of distance behind the tip is shown in Figure VII.1(b). The open symbols are the inactive branches which will not be used in the measurement of $\lambda_2(t)$. If every branch, including the inactive branch, is used and $\lambda_2(t)$ is measured, the slope, n, of the relationship between $\lambda_2(t)$ and distance X behind the tip will be small and a large scattering in data is obtained as shown in Figure VII.1(c). Figure VII.1(d) shows the plot of $\lambda_2(t)$ versus X for the active branches. The slope, n, at large distances, obtained from this measurement is somewhat higher and the scattering of the data is smaller. Consequently, all secondary arm spacings, $\lambda_2(t)$, in this study are measured by using the criterion given by Huang and Glicksman.

2. Experimental results

The log-log plots of normalized branch spacing $\lambda_2(t)/\lambda_2(o)$ versus the solidification time, t_f, are shown in Figure VII.2 for

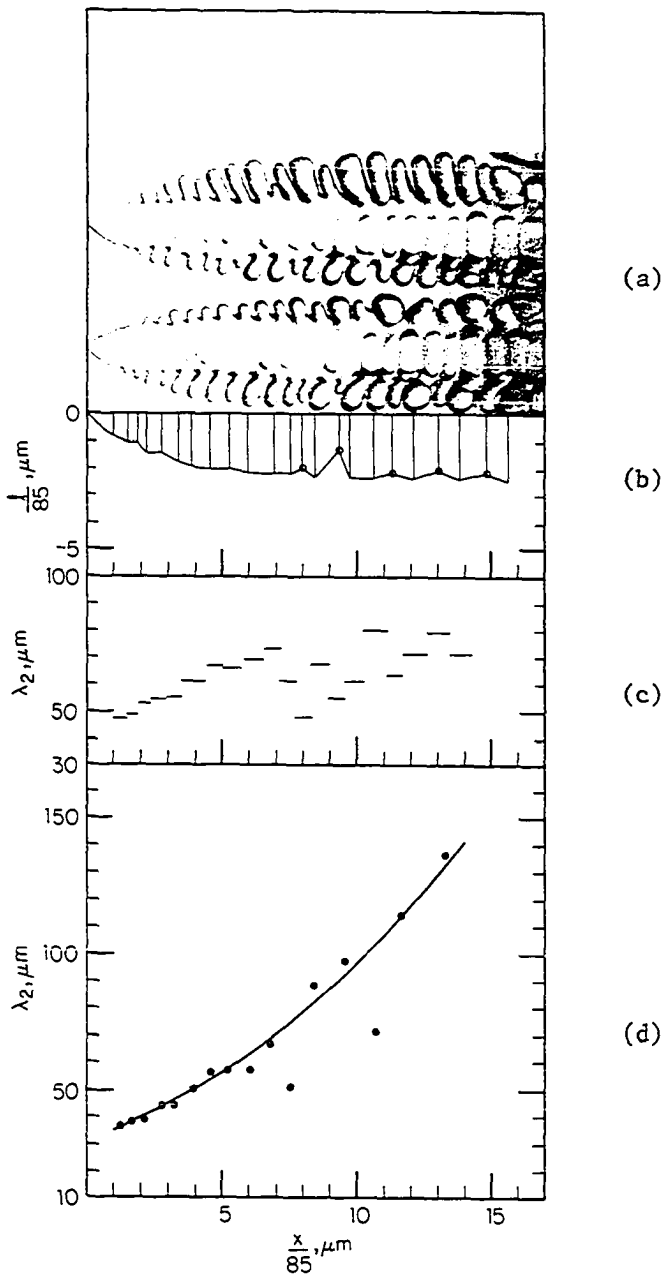

Figure VII.1. The measurement of $\lambda_2(t)$ as a function of distance from the tip. ℓ = length of the sidebranch; X = distance behind the tip

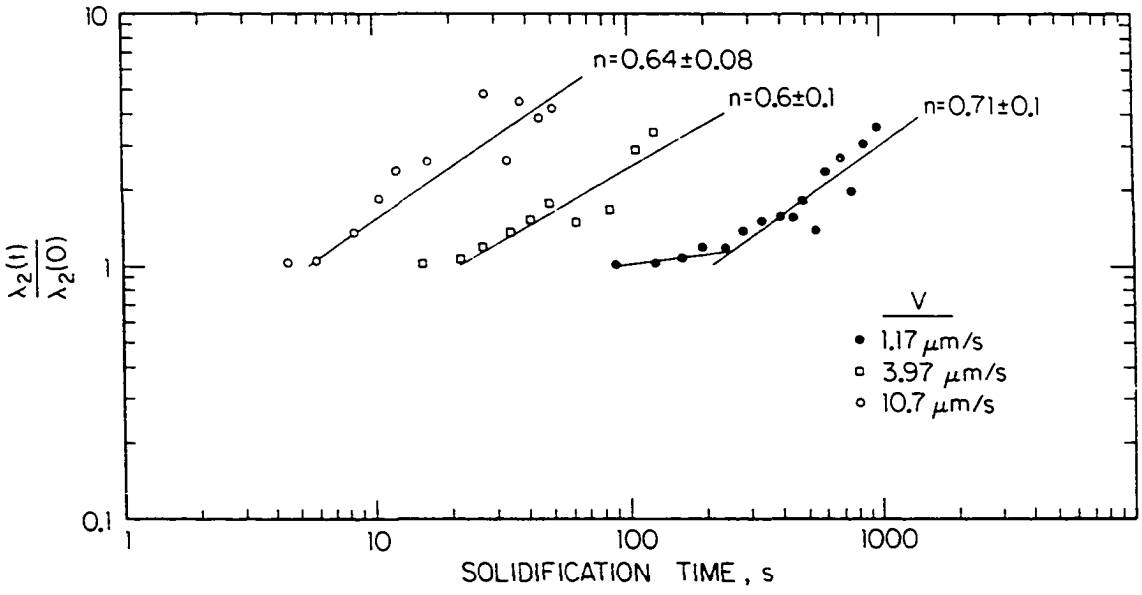

Figure VII.2. Variation of $\lambda_2(t)/\lambda_2(o)$ with solidification time at V = 1.17, 3.97 and 10.7 μm/s in succinonitrile - 4 wt % acetone and G = 67 K/cm

succinonitrile - 4 wt % acetone at four different growth velocities with G = 67 K/cm, where $\lambda_2(t)$ is the secondary arm coarsening behind the dendrite tip and $\lambda_2(o)$ is the initial secondary arm spacing. It shows that each coarsening curve can be broken down into two linear regions, one at very small solidification time where initial coarsening rate is quite slow, and the other for large solidification time where the coarsening rate is high. Note that a rapid coarsening starts sooner as the velocity is increased. We shall discuss only the coarsening rate which occurs at larger solidification times. The results show that within the experimental scattering, the slope is independent of velocity and its value is found to be equal to 0.65 ± 0.05.

The effect of temperature gradient on the secondary arm spacing was carried out at three different temperature gradients with constant V = 10.7 μm/s, and C_∞ = 4 wt % acetone. Figure VII.3 shows the variation of $\lambda_2(t)/\lambda_2(o)$ as a function of solidification time at G = 33, 67 and 86 K/cm. All data are plotted together and it shows that they lie reasonably well on a single straight line with the slope of 0.65 ± 0.05. Thus, we may conclude that the temperature gradient in liquid has a weak effect on the rate of coarsening and the incubation time, t_o, (the time for which the extrapolated line gives $\lambda_2(t)/\lambda_2(o) = 1$) is not a strong function of G.

Figure VII.4 shows the variations of $\lambda_2(t)/\lambda_2(o)$ as a function of solidification time at three different alloy compositions with V = 5.8 μm/s and G = 67 K/cm. The plot of experimental data for each alloy composition shows a straight line behavior. A least square

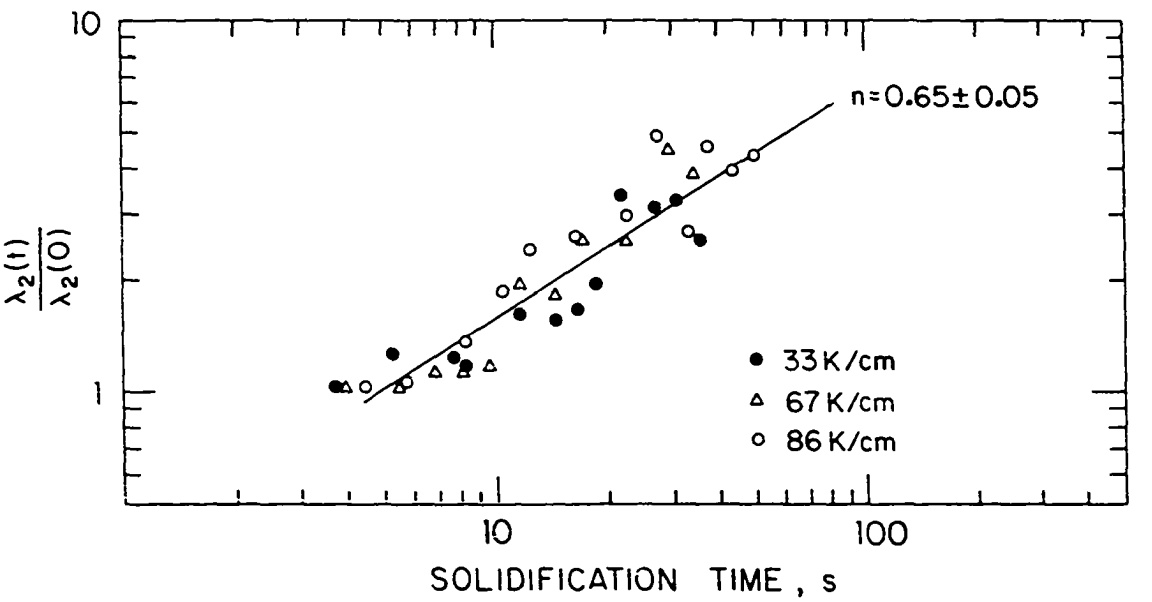

Figure VII.3. Variation of $\lambda_2(t)/\lambda_2(o)$ with t_f in succinonitrile - 4 wt % acetone at V = 10.7 μm/s

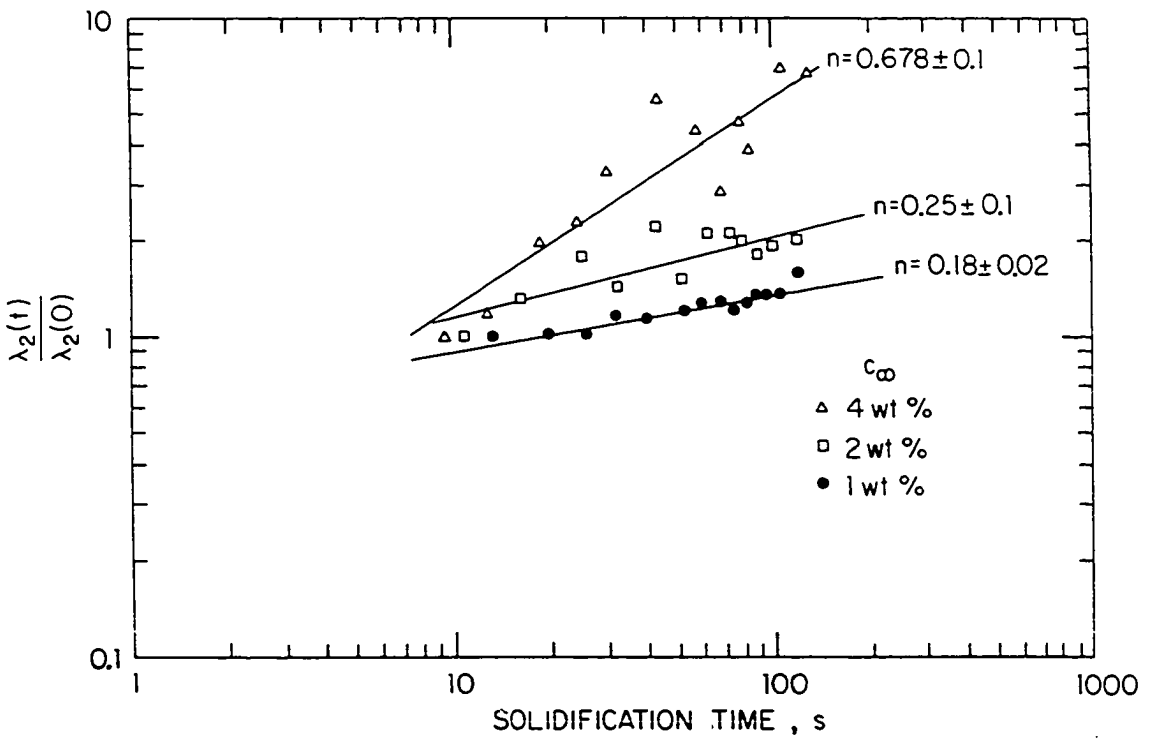

Figure VII.4. Variation of $\lambda_2(t)/\lambda_2(o)$ with t_f at V = 5.7 μm/s and G = 67 K/cm

analysis gives the slopes of 0.18 ± 0.02, 0.25 ± 0.06 and 0.68 ± 0.09 at C_∞ = 1, 2 and 4 wt %, respectively. It is evident that the rate of coarsening increases with the solute concentration. The effect of solute concentration on coarsening process is more dominant than the effect of G and V. Note that the incubation time in this case also does not change appreciably with the composition.

Most experimental work in the secondary arm coarsening showed that the secondary spacing $\lambda_2(t)$ is only a function of solidification time. Thus, if all the data on the $\lambda_2(t)$ are plotted as a function of solidification time, they will conform to a single straight line behavior. Figure VII.5 shows the plot of all data, and it is seen that they do not follow a straight line behavior. The higher growth rate and composition indicate higher values of λ_2 for the same value of t_f. However, the linear regression analysis of these data points gives the slope of 0.35 ± 0.03 which agrees well with the other experimental studies and with the theory (Equation 18) described by Kurz and Fisher [64].

3. Discussion

The coarsening behavior with respect to velocity, shown in Figure VII.2, can be described by a general relationship.

$$\frac{\lambda_2(t)}{\lambda_2(o)} = 1 + A_1(t_f - t_o)^{n_1} \qquad (23)$$

where t_o is the incubation time for which the extrapolated line gives $\lambda_2(t)/\lambda_2(o) = 1$. A_1 and n are constants. A least square analysis of

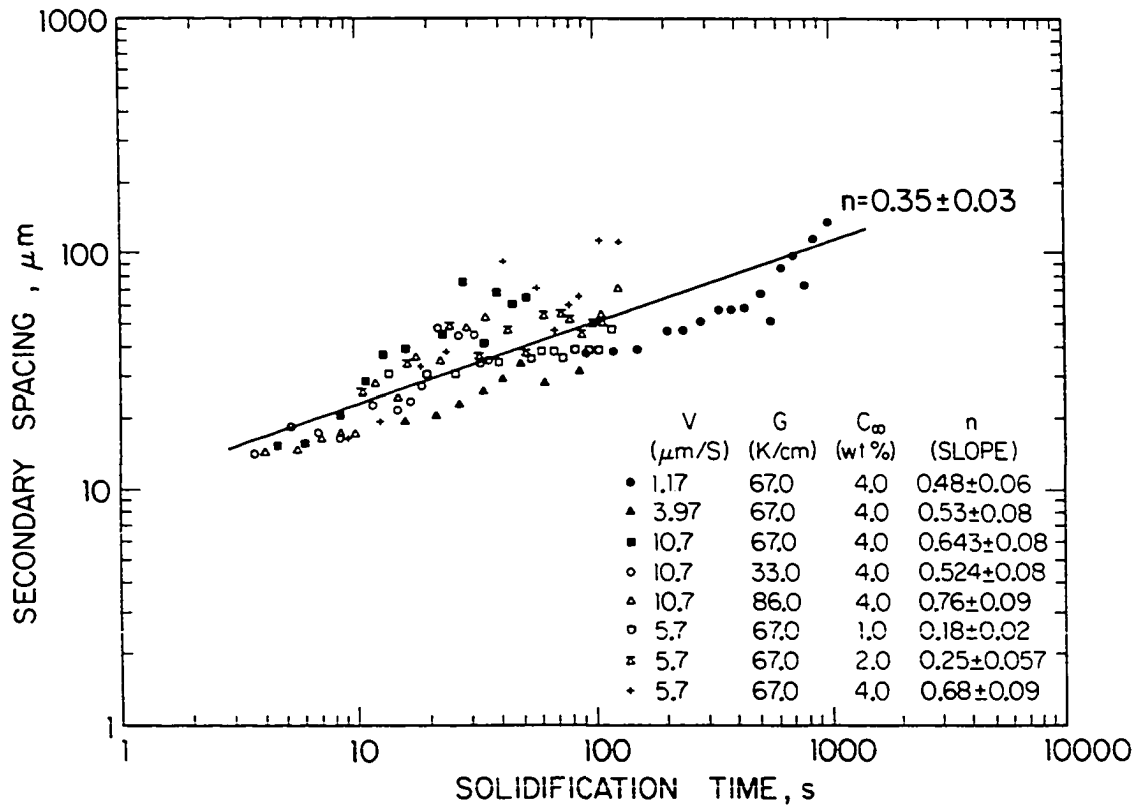

Figure VII.5. Variation of λ_2 with t_f for all experimental data

the higher solidification time portion of the curves gives $n_1 = 0.9 \pm 0.1$. The incubation time, t_o, is a function of velocity, and the variation in t_o with V is shown in Figure VII.6. The value of the constant A_1 is obtained as $A_1 = 0.05 \pm 0.01$.

The variation in $\lambda_2(t)/\lambda_2(o)$ with temperature gradient is found to be quite small. Consequently, the incubation time is not a strong function of temperature gradient. Thus, for constant V and C_∞ , we may write

$$\frac{\lambda_2(t)}{\lambda_2(o)} = 1 + A_2(t_f - t_o)^{n_2} \tag{24}$$

where the values of n_2 and A_2 were found to be: $A_2 = 0.15$ and $n_2 = 0.82$.

The variation in $\lambda_2(t)/\lambda_2(o)$ with composition shows that the slope of the line changes significantly with composition, although the incubation time does not appear to change much. Consequently, we may write

$$\frac{\lambda_2(t)}{\lambda_2(o)} = 1 + A_3(t_f - t_o)^{n_3} \tag{25}$$

where n_3 is a function of composition. The value of n_3 is 0.61, 0.78 or 0.86 corresponding to the composition of 1, 2 or 4 wt % acetone, respectively.

Equations (23)-(25) can thus be concluded to give a general relationship of

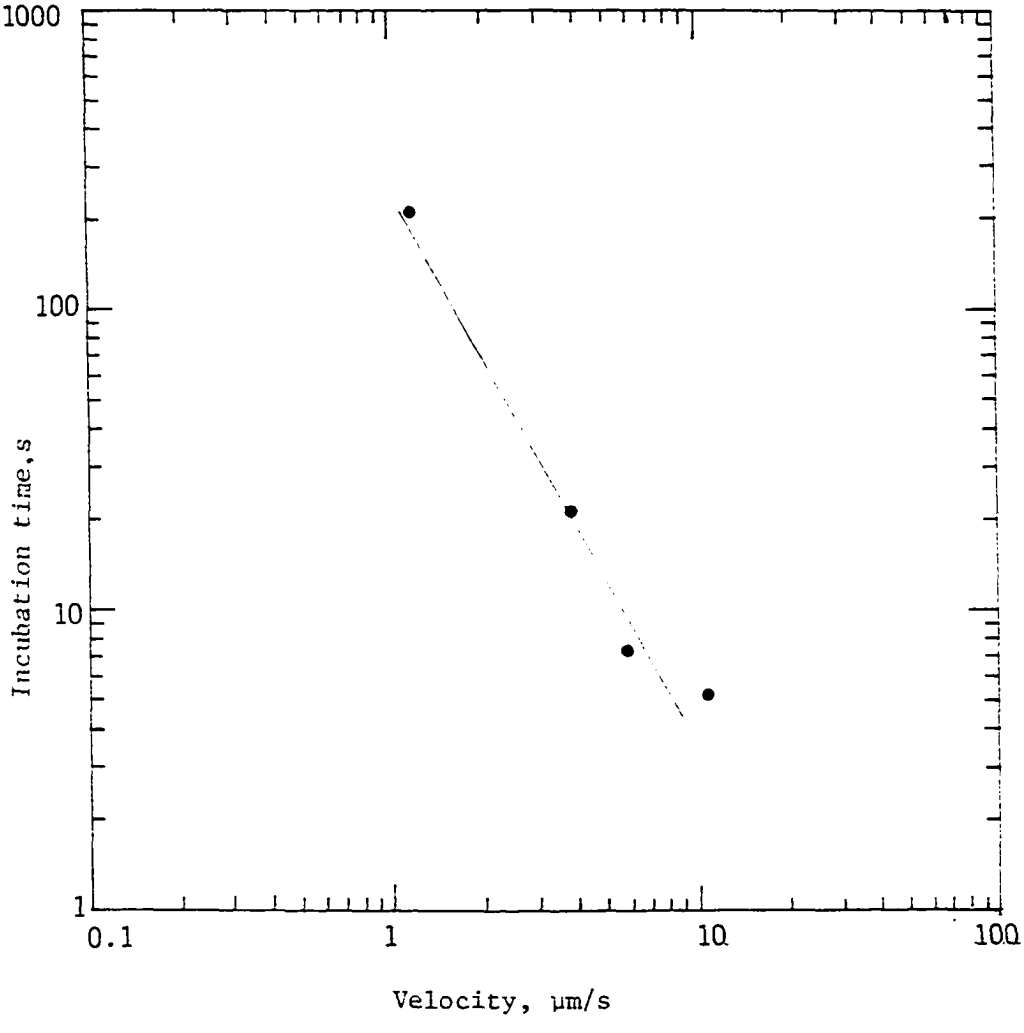

Figure VII.6. Variation of incubation time with growth velocity

$$\frac{\lambda_2(t)}{\lambda_2(o)} = 1 + A(t_f - t_o)^n \qquad (26)$$

where A and n are constant.

It has been established that the driving force for secondary arm coarsening is the reduction in the total surface energy of the system. Consequently, as the curvature at the tip of any given sidebranches increases, the solute concentration gradient in the liquid ahead of that sidebranch decreases which causes that dendrite arm to grow at a slower rate. This will cause the large dendrite arms to grow preferentially. However, this mechanism can occur only if the size of dendrites are different. Huang and Glicksman [25], in the isothermal dendrite growth in pure succinonitrile, found that the secondary arm coarsening process consisted of two mechanisms. The first is competitive sidebranch growth mechanism and the second is the isothermal coarsening by which a small dendrite is eliminated. In our studies, the competitive mechanism of coarsening has been observed, and it is very similar to that described by Huang and Glicksman [25]. During the growth, certain fluctuations in growth rate develop with a characteristic wavelength such that some of the sidebranches grow slightly higher than the neighboring sidebranches. Once such a fluctuation occurs, the slowly growing sidebranches disappear and the periodicity of the profile is governed by the active sidebranches. The thickening of these sidebranches primarily occurs due to the surface energy driven coarsening phenomena. In contrast to

Huang and Glicksman [25] studies, the temperature at the sidebranch decreases as one goes further back from the tip. Consequently, the coarsening rate is much smaller than that obtained for isothermal conditions. Furthermore, the presence of a temperature gradient causes the sidebranches to translate toward the growth direction, as reported earlier by Allen and Hunt [69].

In contrast to isothermal coarsening of pure material, the coarsening phenomenon which occurs during directional solidification of alloys is complicated by the fact that the composition in the liquid increases and the temperature decreases as the distance from the tip increases. Furthermore, a significant interaction is present between the neighboring dendrites. Consequently, the detailed kinetics of coarsening would be significantly different from the isothermal coarsening rate observed for pure succinonitrile.

The effect of different variables on the coarsening rate will now be briefly described.

(a) The effect of increasing the alloy composition is to increase primary spacing and to decrease dendrite tip radius. As the primary spacing increase, the effect of the neighbor dendrite is small, thus the competitive growth can occur which will increase the rate of coarsening. Also, when ρ decreases, the sidebranch becomes thinner which should result in greater coarsening according to the melting process.

(b) Increasing growth velocity will result in decreasing the primary arm spacing and dendrite tip radius. The decrease in primary spacing will result in the decrease in coarsening of secondary arm, but this

effect is slowed down because of the decrease in dendrite tip radius which favor the coarsening of secondary arm. These two effects are combined together during the coarsening process. Consequently, the effect of growth rate on the coarsening of the secondary arm is smaller than the effect of alloy composition.

(c) The experimental results in Figure VII.3 show that temperature gradient has a small effect on the rate of coarsening. The increase in the temperature gradient is to decrease the local temperature at any given location of the sidebranch. This could lead to the slowdown in the coarsening rate. However, the local composition at that location increases, which will increase the coarsening rate. These two effects appear to be nearly the same so that temperature gradient does not affect appreciably the coarsening rate, as seen in Figure VII.3.

Thus, we may conclude that the major effects of the coarsening in array dendrite growth are primary spacing and dendrite tip radius. 1) Increasing the primary spacing will increase the rate of coarsening by increasing the competitive growth. 2) Decreasing in tip radius will result in the increase in the rate of coarsening by remelting of the smaller dendrite. However, the increase in primary spacing alone cannot significantly increase the rate of coarsening. Consequently, these two effects are the major important factors which must be considered during the coarsening process of array dendrite growth.

B. Tertiary Arm Formation

Besides the primary and secondary arm spacings, another dendrite characteristic which occurs during the dendrite growth is the formation

of tertiary arm. These tertiary arms play an important part during the adjustment of primary spacing. In Part V, on the transient effect, the formation of tertiary arm during the adjustment of primary spacing was observed, as shown in Figure V.4. This tertiary arm could grow and become one of the primary arms if the spacing between the primary spacing is sufficiently large.

The experimental studies show that no tertiary branches are formed if the dendrite array has the steady-state primary spacing. Consequently, the formation of tertiary arms occurs during the transient period. Alternatively, tertiary branches can form during the steady-state growth process if fluctuations in primary spacings occur. It is observed that a finite $\Delta\lambda_1$ is required before tertiary branches can form. Figure VII.7 shows the presence of tertiary arms. However, after a steady-state is established, no tertiary branches are seen.

Experimental studies show that the formation of tertiary branch occurs at some distance behind the dendrite tip. Near the dendrite tip region, the formation of the secondary dendrite arms occurs by the perturbation wave mechanism. In this region, the length of the secondary arms are small and have the same size. At some distance behind the dendrite, outside the perturbation mechanism effect, one of the secondary arms can grow faster than the other and become a source of tertiary arms. However, the growth of this tertiary arm is affected by the solute diffusion from the neighbor primary arms. If the spacing between the primary arm is slightly larger than the steady-state spacing, then the diffusion of solute from the neighbor arms will

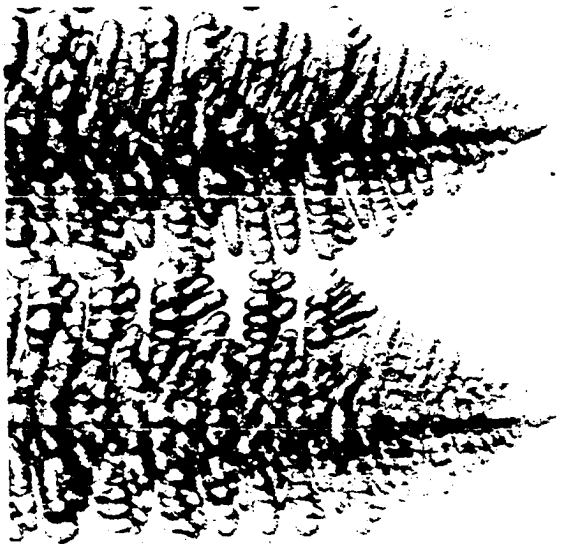

Transient state

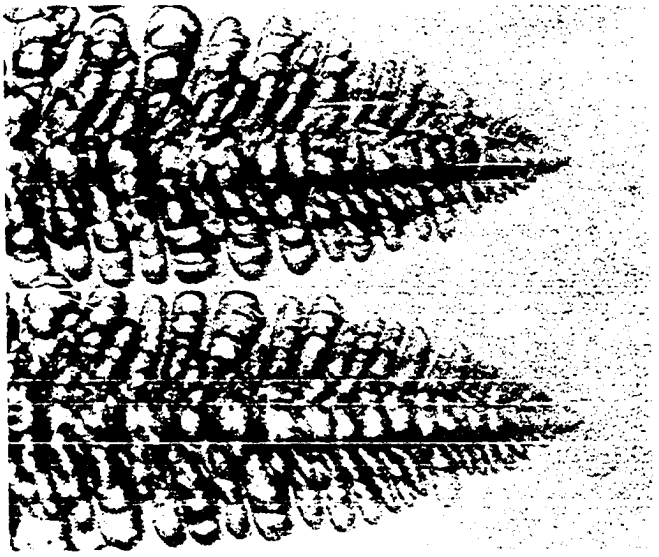

Steady state

Figure VII.7. The formation of tertiary arm during the transient period

impede the growth of tertiary arms. This tertiary arm will slow down. If the primary spacing is sufficiently large, this tertiary arm will grow and become one of the primary arm spacing. The experimental observation shows that if the primary spacing is two times larger than the steady-state spacing, the tertiary arm will be effective as a source of primary arm.

A simple explanation can be given to understand why a tertiary branch, which becomes a primary dendrite, needs to be located further behind the dendrite tip. Figure VII.8 shows the concentration profile ahead of the dendrite arrays. The fastest growing tertiary branch will have the largest composition gradient in front of it. Note that the largest composition gradient is present at the center of the two primary arms, and this gradient has the largest value at a distance X_T from the dendrite tip. Furthermore, for a tertiary arm to become effective as a source, the secondary spacing ahead of the tertiary branch should not impede the growth of tertiary branch. Thus, the length of the secondary branch on which the tertiary arms form should be significantly larger than the active secondary branch ahead of it. Consequently, some coarsening phenomenon is required to increase the spacing between the secondary branches. In addition, it is required that the growth rate of the tertiary branch be greater than the growth rate of the active secondary branch ahead of the tertiary branch. As noted earlier, the location at which tertiary branch will have the largest growth rate is between the dendrites at a distance X_T from the tip. Whether a tertiary branch becomes a primary arm or not is illustrated in a series

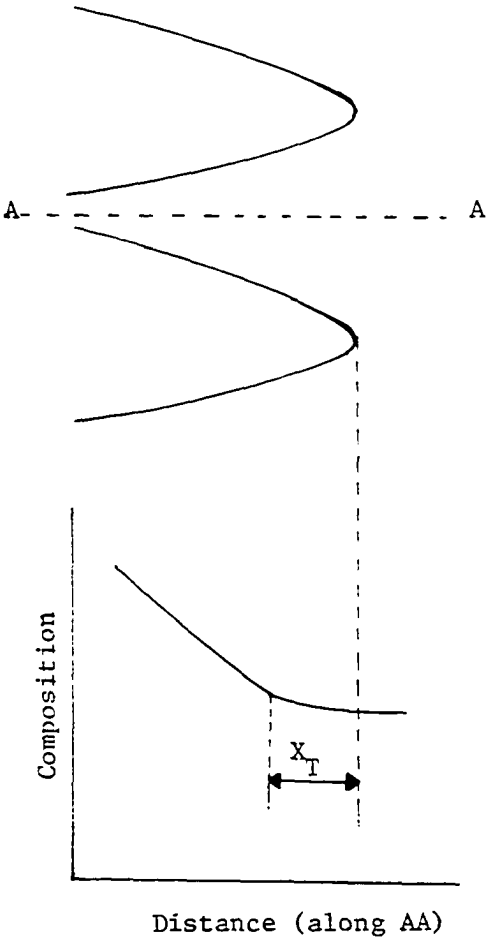

Figure VII.8. Schematic diagram of composition variation along the distance X behind the dendrite tip

of micrographs shown in Figure VII.9, which shows a series of dendrite structures at different growth velocities with G = 67 K/cm and C_∞ = 4 wt % acetone. The spacing between dendrites No. 1 and No. 2 is slightly larger than the steady-state spacing and the tertiary arm occurs, as shown in Figure VII.9. This tertiary arm is not effective as a source of primary arm because the spacing between primary arm is too small. Figure VII.10 shows the plot of primary spacing required to create the tertiary branch as a function of velocity. It is shown that the spacing required to create the tertiary arm increases as the growth velocity is decreased.

The formation of tertiary arm can be seen very clearly if it occurs between two dendrites which grow at different orientations. Figure VII.11 shows a series of dendrites' structure at V = 5.0 μm/s, G = 67 K/cm and C_∞ = 4 wt % acetone. It shows that the formation of tertiary arm occurs very easily at the liquid region between dendrites No. 1 and No. 2. In this region, the space between the dendrites is large enough to cause the formation of tertiary arms. This tertiary will grow very fast and become one of the primary arms. As the new primary arm forms, the spacing between this new primary arm and the old neighboring arm is exactly equal to the steady-state spacing.

The mechanism of tertiary branch propagation to form a primary arm, when two dendrite arrays are not parallel, can be applied to understand the mechanism of the chill-to-columnar zone transition that occurs in a casting. It is generally rationalized that the favorably oriented grains will outgrow the unfavorably oriented grain. How a

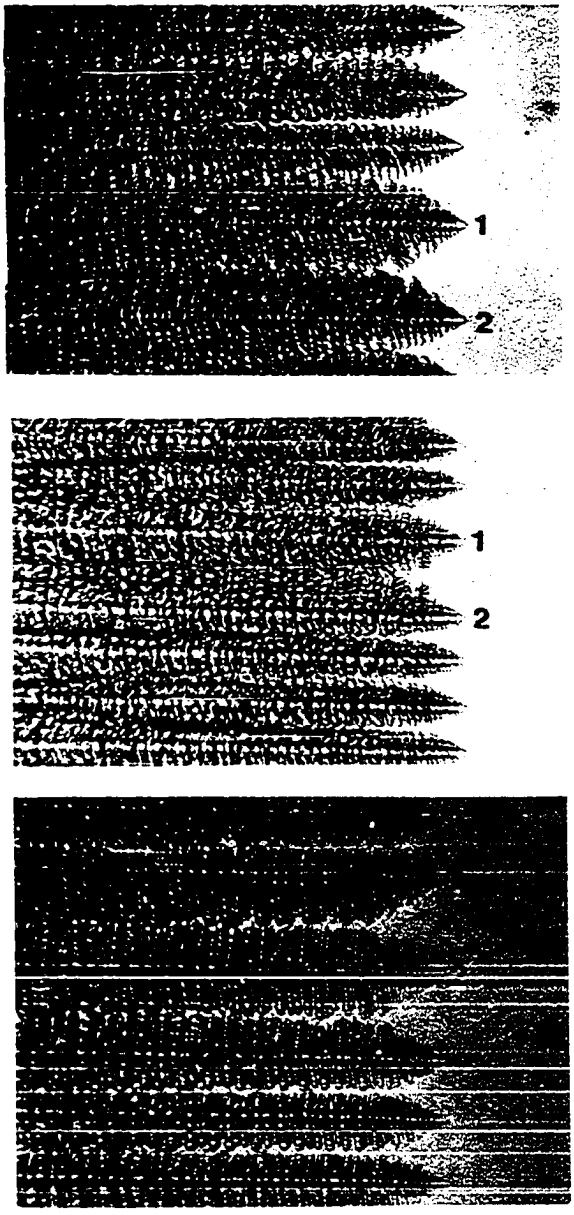

(a)
[40x]

(b)
[40x]

(c)
[60x]

Figure VII.9. A series of dendrite structures showing the formation of tertiary arms in succinonitrile - 4 wt % acetone at G = 67 K/cm. (a) V = 10.7 μm/s, (b) V = 20.0 μm/s, (c) V = 65.0 μm/s

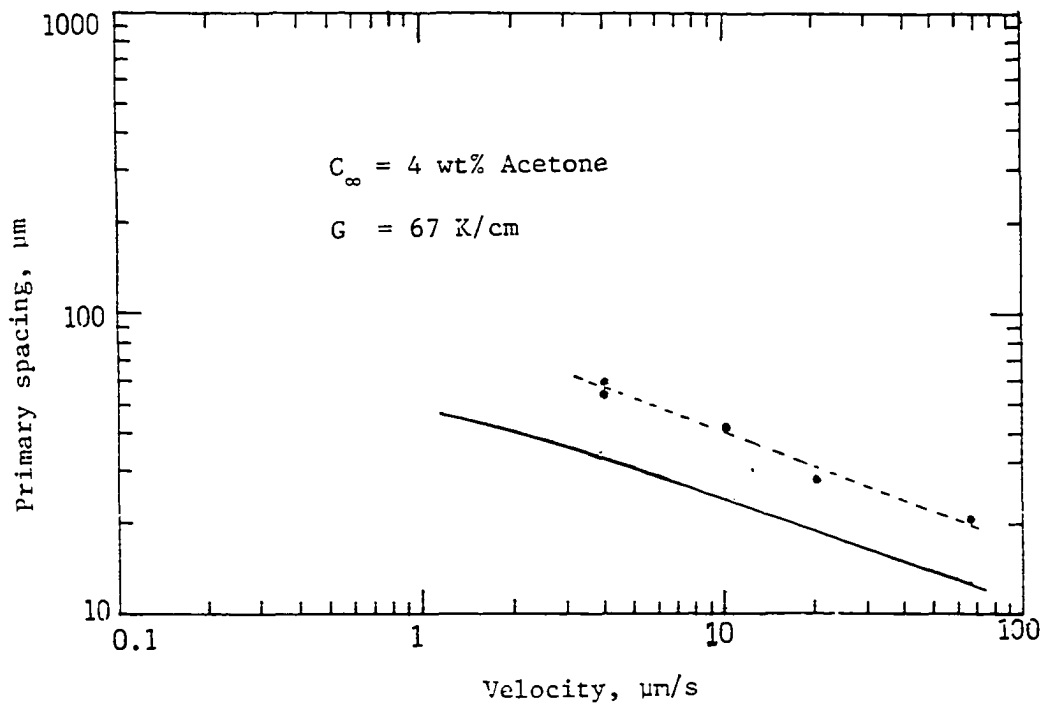

Figure VII.10. The variation of primary spacing with growth velocity. (Solid line is the steady-state primary spacing, dotted line is the spacing required to create tertiary arm)

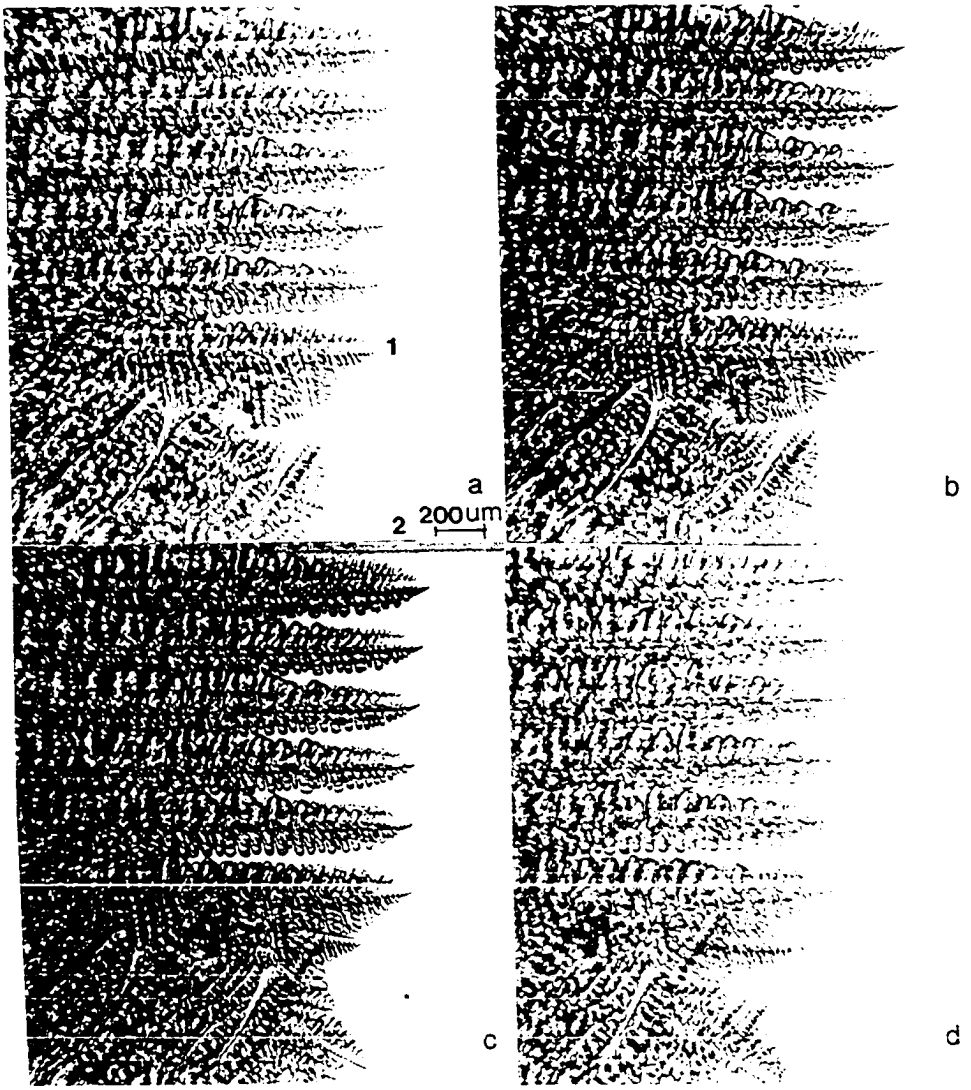

Figure VII.11. A series of dendrite structures in succinonitrile - 4 wt % acetone at V = 5.0 μm/s, G = 67 K/cm. (The tertiary arms form between dendrite No. 1 and No. 2)

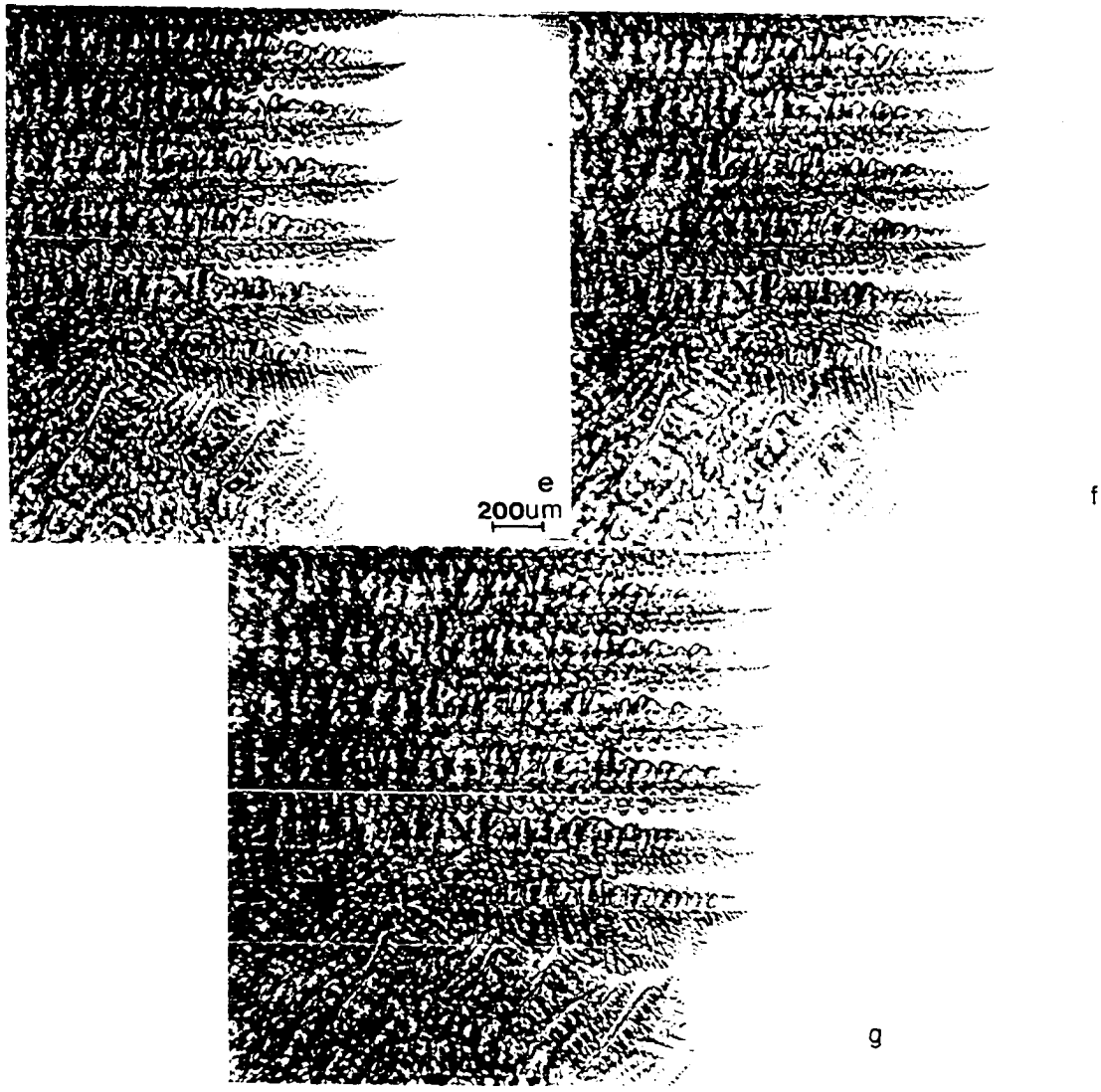

Figure VII.11. Continued

given grain wins in the competitive growth is not well-documented. Figure VII.11 shows a dendrite growing in different directions. If the dendrite array is in the heat flow direction, it generates new primary branches. The generation of primary branches depends upon the relative orientation of the grains. If the dendrite growth directions of the two adjacent grains diverge, then tertiary branches of the favorably oriented grains becomes a source of primary branches and the dendrite array expands laterally. Thus, a grain No. 2 in Figure VII.12 will expand in both directions. However, if the growth directions of two grains converge, no lateral growth is possible, as shown for the top region of grain No. 1 in Figure VII.12. However, if two grains converge, the growth direction of the favorably oriented grain on the other side of arrays will always diverge, thereby causing that grain to grow. Consequently, all grains which are favorably oriented will act as a source for the primary dendrite formation, and consequently, lateral growth of these grains will occur until all unfavorably oriented grains disappear.

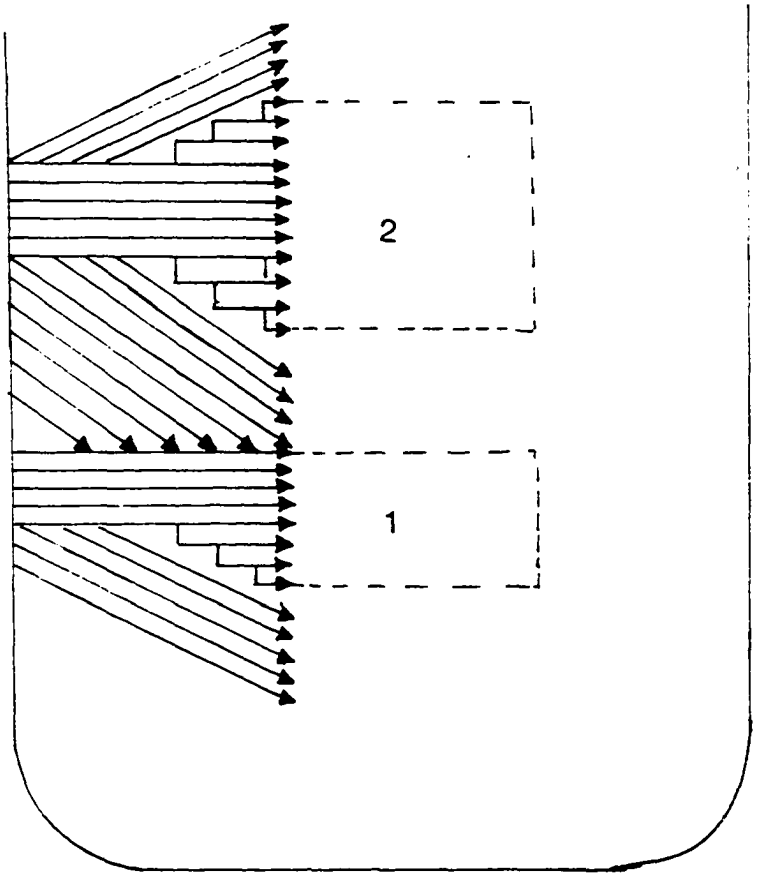

Figure VII.12. Schematic illustration of the growth of array dendrites from chill-to-columnar zone

VIII. CONCLUSIONS

Directional solidification studies in succinonitrile-acetone systems have been presented to characterize microstructural characteristics of the solid-liquid interface. Experiments have been carried out to study 1) steady-state characteristics of dendrite morphology, 2) transient effect of dendritic growth, 3) the initial breakup of a planar interface and the pattern formation process during the solidification and 4) the dynamical studies of secondary and tertiary branch formation.

(1) Experiment measurement on dendrite tip radii are found to agree well with the theoretical models. The initial secondary spacing is found to scale with the dendrite tip radius with $\lambda_2/\rho = 2.0$. This scaling law is found to be independent of experimental variables in this system. Furthermore, both λ_2 and ρ are found to be independent of G in the high growth rate regime. Their dependence on V and C_∞ was found to be a function of VC_∞ only. Theoretical values for primary spacing were found to agree well with the experimental data.

(2) The transient effect of dendritic growth is carried out in succinonitrile - 4 wt % acetone solution to quantitatively evaluate the mechanisms by which a steady-state interface restabilized to a new pattern when the applied growth rate is suddenly increased or decreased. The restabilization process is found to occur by two distinctly different mechanisms, one mechanism operating when the velocity is increased and the other when the velocity is decreased. A strong

hysterisis effect is seen in the V-ρ space during the transient time. It is shown that, irrespective of the mechanism of restabilization, the final steady-state dendrite tip radius always approaches the value which is just marginally stable.

(3) The pattern formation processes are found to be different in cellular and dendrite regions. The initial perturbation of the periodicity are more uniform in dendritic region than in cellular region. The initial wavelength, λ_i, and the final wavelength, λ_1, in cellular region are nearly the same, whereas in dendrite region, λ_1 is much larger than λ_i. Both λ_1 and λ_i are found to be significantly smaller than that corresponding to the maximum amplification predicted by the linear stability analysis.

(4) The effect of increasing solute content and growth velocity is to increase the rate of coarsening, whereas the temperature gradient has no effect on the rate of secondary arm coarsening. It is proposed that the increase in the rate of coarsening is mainly due to the decrease in tip radius and the increase in primary spacing.

(5) The formation of tertiary arm occur if the spacing between primary arm is larger than the steady-state spacing. This formation is easier if the tertiary arm forms between two dendrites which grow at different orientations. The dendrite which is favorably oriented with respect to the heat flow direction becomes a source for primary arms and thus, overtakes the dendrites which are not favorably oriented.

(6) A number of important scaling laws have been found.

a) The primary dendrite spacing is found to be precisely equal to the large wavelength, λ_f, of the planar interface breakup.

b) The secondary spacing λ_2 is found to be equal to the wavelength λ_i observed during the planar interface instability.

c) The dendrite tip radius is found to be equal to $\lambda_2/2$ for all experimental conditions.

d) The distance λ_p has been found to be equal to $0.5\ (\lambda_1\lambda_2)^{\frac{1}{2}}$ for all experimental conditions in the dendrite growth process.

IX. REFERENCES

1. Jackson, K. A.; Hunt, J. D. Acta Met. 1965, 13, 1212.
2. Glicksman, M. E. Private communication, RPI, Troy, N.Y., 1982.
3. Langer, J. S. Rev. Mod. Phys. 1980, 52, 1.
4. Langer, J. S. Met. Trans. A 1984, in press.
5. Dee, G; Langer, J. S. Phys. Rev. Letters 1983, 50, 383.
6. Brower, R. C.; Kessler, D. A.; Koplik, J.; Levine, H. Phys. Rev. Letters 1983, 51, 1111.
7. Dee, G; Mathur, R. Phys. Rev. B 1983, 27, 7073.
8. Tiller, W. A.; Jackson, K. A.; Rutter, J. W.; Chalmers, B. Acta Met. 1953, 1, 428.
9. Tiller, W. A. In "The Art and Science of Growing Crystals"; Gilman, J. J., Ed.; John Wiley and Sons, Inc.: New York, 1963.
10. Mullins, W. W.; Sekerka, R. F. J. Appl. Phys. 1964, 35, 444.
11. Hardy, S. C.; Coriell, S. R. J. Crystal Growth 1968, 3-4, 569.
12. Hardy, S. C.; Coriell, S. R. J. Appl. Phys. 1968, 39, 3505.
13. Hardy, S. C.; Coriell, S. R. J. Crystal Growth 1969, 5, 329.
14. Hardy, S. C.; Coriell, S. R. J. Crystal Growth 1970, 7, 147.
15. Coriell, S. R.; Hardy, S. C. J. Appl. Phys. 1969, 40, 1652.
16. Coriell, S. R.; Hardy, S. C.; Sekerka, R. F. J. Crystal Growth 1971, 11, 53.
17. Sato, T.; Ohira, G. J. Crystal Growth 1977, 40, 69.
18. Sato, T.; Shibata, K.; Ohira, G. J. Crystal Growth 1977, 40, 69.
19. Shibata, K.; Sato, T.; Ohira, G. J. Crystal Growth 1978, 44, 419.
20. Teghtsoonian, E.; Chalmers, B. Can. J. Phys. 1951, 29, 370.
21. Atwater, H.; Chalmers, B. Can. J. Phys. 1957, 35, 208.

22. Tiller, W. A.; Rutter, J. W. Can. J. Phys. 1956, 34, 96.

23. Glicksman, M. E.; Schaefer, R. J.; Ayers, J. D. Met. Trans. A 1976, 7A, 1747.

24. Huang, S. C.; Glicksman, M. E. Acta Met. 1981, 29, 701.

25. Huang, S. C.; Glicksman, M. E. Acta Met. 1961, 29, 717.

26. Sharp, R. M.; Hellawell, A. J. Crystal Growth 1971, 11, 77.

27. Kramer, J. J.; Bolling, G. F.; Tiller, W. A. Trans. Met. Soc. AIME 1963, 227, 374.

28. Sharp, R. M.; Hellawell, A. J. Crystal Growth 1970, 6, 253.

29. Backerud, L.; Chalmers, B. Trans. Met. Soc. AIME 1969, 245, 309.

30. Doherty, R. D.; Feest, E. A.; Holm, K. Met. Trans. 1973, 4, 115.

31. Burden, M. H.; Hunt, J. D. J. Crystal Growth 1974, 22, 99.

32. Bower, T. F.; Brody, H. D.; Flemings, M. C. Trans. Met. Soc. AIME 1966, 236, 624.

33. Burden, M. H.; Hunt, J. D. J. Crystal Growth 1974, 22, 109.

34. Ivantsov, G. P. Dokl. Akad. Nauk SSSR 1947, 58, 562.

35. Trivedi, R. J. Crystal Growth 1980, 49, 219.

36. Trivedi, R. Acta Met. 1970, 18, 287.

37. Jin, I.; Purdy, G. R. J. Crystal Growth 1974, 23, 29.

38. Kurz, W.; Fisher, D. J. Acta Met. 1970, 18, 287.

39. Trivedi, R. Unpublished work, Iowa State University, Ames, Iowa.

40. Edwardson, T.; Fredrikson, H.; Svenson, I. Metal Science 1976, 10, 298.

41. Kotler, G. R.; Casey, K. W.; Cole, G. S. Met. Trans. 1972, 3, 723.

42. Dann, P. C.; Eady, J. A.; Hogan, L. M. J. Australian Inst. Metals 1974, 19, 140.

43. Spittle, J. A.; Lloyd, D. M. "Solidification and Casting of Metals Metals"; The Metals Society: London, 1972; Book 192, p. 15.

44. Jacobi, H.; Schwerdtfeger, K. Met. Trans. A 1976, 7A, 811.

45. Okamoto, T.; Kishitake, K. J. Crystal Growth 1975, 29, 131.

46. Langer, J. S.; Müller-Krumbhaar. Acta Met. 1978, 25, 1697.

47. Honjo, H.; Sawada, Y. J. Crystal Growth 1982, 58, 297.

48. Bell, J. A. E.; Winegard, W. C. J. Inst. Metals 1964, 92, 357.

49. Coulthard, J. O.; Elliot, R. J. Inst. Metals 1967, 95, 21.

50. Jesse, R. E.; Giller, H. F. J. I. J. Crystal Growth 1970, 7, 348.

51. Sharp, R. M.; Hellawell, A. J. Crystal Growth 1970, 6, 334.

52. Okamoto, T.; Kishitake, K. J. Japan Inst. Metals 1972, 36, 869.

53. Young, K. P.; Kirkwood, D. H. Met. Trans. A 1975, 6A, 197.

54. Klaren, C. M.; Verhoeven, J. D.; Trivedi, R. Met. Trans. A 1980, 11A, 1853.

55. Mason, J. T.; Verhoeven, J. D.; Trivedi, R. J. Crystal Growth 1982, 59, 516.

56. McCartney, D. G.; Hunt, J. D. Acta Met. 1981, 29, 1851.

57. Hunt, J. D. "Solidification and Casting of Metals"; The Metals Society: London, 1979; Book 192.

58. Trivedi, R. Met. Trans. A, in press.

59. Flemings, M. C.; Poirer, D. R.; Barone, R. V.; Brody, H. O. J. Iron Steel Inst. 1970, 208, 371.

60. Taha, M. A.; Jacobi, H.; Imagumbai, M.; Schwerdtfeger, K. Met. Trans. A 1982, 13A, 2131.

61. Chernov, A. A. Kristallografiya 1956, 1, 583.

62. Kahlweit, M. Scripta Met. 1968, 2, 251.

63. Kattamis, T. Z.; Coughlin, J. C.; Flemings, M. C. Trans. Met. Soc. AIME 1967, 239, 1504.

64. Kurz, W.; Fisher, D. J. "Fundamentals of Solidification", in press.

65. Werner, E. A. Analyst 1933, 58, 335.

66. Hunt, J. D.; Jackson, K. A.; Brown, H. Rev. Sci. Instrum. 1966, 37, 805.

67. Jackson, K. A.; Hunt, J. D.; Uhlmann, D. R.; and Seward III, T. P. Trans. AIME 1966, 236, 149.

68. Verhoeven, J. D.; Gibson, E. D. Met. Trans. 1972, 3, 1893.

69. Allen, D. J.; Hunt, J. D. Met. Trans. A 1976, 7A, 767.

70. Wulff, A. C.; Westrum, Jr., E. F. J. Phys. Chem. 1963, 67, 2376.

X. ACKNOWLEDGMENTS

I would like to express my appreciation to Dr. Rohit Trivedi, my major professor, for his patience, help and guidance during the research and throughout my graduate program. I also wish to thank Dr. John Patterson, Dr. John Verhoeven, Dr. Douglas Finnemore and Dr. James Corones for their service on my graduate committee.

My appreciation is extended to John Mason for his valuable assistance in providing the solidification equipment and his helpful suggestions. I also wish to thank Barbara Dubberke for excellent typing of this manuscript.

Special thanks to the Royal Thai Navy for the financial support throughout my graduate program.

Finally, I thank Boondarig, my wife, for her love, understanding, support and assistance. I thank her for her encouragement and many sacrifices during the course of my graduate program.

XI. APPENDIX A: THE PHYSICAL PROPERTIES OF SUCCINONITRILE

Succinonitrile [$CNCH_2CH_2CN$] is a cubic crystal in nature at room temperature. The experimental studies on the properties of succinonitrile by Wulff and Westrum [70] showed that succinonitrile exhibited two different crystal phases at two temperature ranges. The low temperature phase, $T < -46^{\circ}C$, is monoclinic. The high temperature phase, $-46^{\circ}C < T < 58^{\circ}C$, is body-centered cubic. The transition from the low temperature phase to the high temperature phase is from a completely ordered phase to highly disordered phase with the entropy of transition $\Delta S = 6.35$ cal/mole K. At $T = 58^{\circ}C$, the high temperature phase succinonitrile transforms to liquid phase with the entropy of melting, $\Delta S_m = 2.68$ cal/mole -K. The solidification of high temperature phase from liquid is analogue to that for metal system. The addition of small amount of acetone into pure succinonitrile reduces the melting point of pure succinonitrile, and the solid solution system is obtained.

The physical properties of pure succinonitrile and succinonitrile-acetone system are shown below.

Succinonitrile

Melting point	331.24	K
Entropy of fusion	11.21	J/mol K
Density of solid	1.016×10^3	kg/m^3
Density of liquid	0.907×10^3	kg/m^3
Thermal conductivity of solid	0.224	J/msK

Thermal conductivity of liquid	0.223	J/msK
Surface energy	8.95×10^{-3}	J/m^2
<u>Succinonitrile-acetone</u>		
Diffusion coefficient	1.27×10^{-5}	cm^2/s
Liquidus slope	3.02	K/wt % acetone
Equilibrium partition ratio	0.10	

XII. APPENDIX B: SUMMARY OF EXPERIMENTAL DATA ON STEADY-STATE GROWTH

V (μm/s)	G (K/cm)	C_∞ (wt %)	λ_1 (μm)	λ_2 (μm)	λ_p (μm)	ρ (μm)	Sample thickness	Run no.
1.1	71.0	4.0	501.0, 488.0	46.6	--	20.7	50	47
1.5	64.9	4.0	456.0	34.8	--	17.44	50	48
2.15	66.0	4.0	445.0, 404.0	26.4, 27.4	--	10.9, 11.1	50	45
3.97	65.9	4.0	360.6, 407.0	23.2, 22.7	--	10.1	50	44
4.3	67.34	4.0	154.02	--	--	17.24	50	40
11.0	69.93	4.0	314.2, 309.9	12.6	--	5.65	50	36
13.67	68.6	4.0	300, 317	9.10	--	4.2	50	41
7.50	67.5	4.0	375.0, 370.0	15.6	--	6.27	50	49
27.56	70.15	4.0	192.0	6.9	--	3.06	50	42
34.0	66.67	4.0	157.9, 158.3	5.8, 5.53	17.2	2.7, 2.4	50	43
65.6	65.6	4.0	142.2, 138.6	4.7, 5.1	--	2.1, 1.8	50	46
101.8	66.3	4.0	91.56	3.4	--	1.65	50	50
1.06	69.0	4.0	505.0	39.5	--	19.6	100	56
4.01	70.6	4.0	335.0	22.23	--	11.1	100	55
10.7	66.7	4.0	241.3	13.0	--	6.2	100	52
25.2	73.07	4.0	183.19	7.5	--	3.5	100	54
0.40	67.0	4.0	93.0	--	--	--	150	94
0.68	67.0	4.0	188.0	--	--	52.0	150	95
1.17	67.0	4.0	472.0	47.5	81.16	23.0	150	91
2.15	67.0	4.0	377.0	30.7	57.79	13.6	150	75

V (μm)	G (K/cm)	C_∞ (wt %)	λ_1 (μm)	λ_2 (μm)	λ_p (μm)	ρ (μm)	Sample thickness	Run no.
3.97	65.0	4.0	328.0	21.6	48.69	10.3	150	74
5.8	67.0	4.0	294.4	17.8	39.4	8.9	150	126
10.7	66.7	4.0	240.5	14.2	33.7	6.2	150	47
25.5	66.7	4.0	174.2	8.2	--	4.0	150	58
65.6	65.6	4.0	125.2	5.8	--	2.3	150	63
100.0	67.0	4.0	96.8	--	--	1.77, 2.2	150	76
3.97	69.0	4.0	324.0	20.8	--	9.8	500	80
10.7	67.0	4.0	240.0	13.5	35.0	6.3	500	79
65.3	29.6	4.0	182.0, 180.0	5.7	18.3	2.5	150	119
65.8	42.4	4.0	144.0, 156.0	5.2	15.1	2.56	150	118
65.9	52.0	4.0	144.0, 142.0	5.1	16.1	2.30	150	117
64.3	77.0	4.0	116.7, 123.0	5.3, 5.7	14.8	2.3, 2.5	150	66
10.6	29.9	4.0	370.0	11.2, 12.0	37.5	5.25	150	125
10.6	41.0	4.0	332.5	13.1, 12.6	36.0	5.73	150	124
10.64	46.7	4.0	262.0, 268.0	11.4	30.1	5.27	150	121
10.54	63.7	4.0	240.5, 250.0	12.6	33.7	5.4	150	123
10.75	77.02	4.0	209.9, 202.0	13.1, 13.7	27.9	5.73	150	122
5.5	64.0	0.25	152.0	--	--	63.0, 71.2	150	112
5.6	65.6	0.448	148.0, 118.0	--	--	29.5, 32.3	150	114
5.67	68.4	0.55	185.0	42.0, 44.0	80.0	23.5, 25.0	150	113

V (μm)	G (K/cm)	C_∞ (wt %)	λ_1 (μm)	λ_2 (μm)	λ_p (μm)	ρ (μm)	Sample thickness	Run no.
5.7	69.0	1.0	235.7	30.08	61.1	18.2	150	99
5.75	69.0	2.0	274.72	28.0	45.7	14.86	150	100
5.8	69.0	3.0	277.2, 266.0	21.9	43.0	11.62	150	101
5.87	69.0	4.0	286.0	16.5	--	8.6	150	102
5.5	68.0	1.5	189, 250	32.3	56.8	16.5	150	111
5.8	69.0	1.0	237.56	38.9, 36.0	50.2	22.8	250	104